UNIVERSITÀ DEGLI STUDI DI PADOVA

Dipartimento di Fisica e Astronomia "Galileo Galilei"

Master Degree in Astrophysics and Cosmology

Final Dissertation

ALMA reveals the nature of LABOCA submillimeter sources in a galaxy protocluster field at z=2.2

Thesis Supervisor:
Prof. Paolo Cassata
Thesis Co-supervisor:
Dr. Helmut Dannerbauer

Candidate:
Alessandro Bianchetti

Academic Year 2021/2022

Abstract

Submillimeter Galaxies (SMGs) are among the best indicators of star formation activity in the high redshift Universe. In fact, most of them consist of young galaxies enshrouded in dust, whose optical/UV light is absorbed by the dust cloud and re-emitted in the submm. In this work, we present 870 μm Atacama Large Millimeter/sub-millimeter Array (ALMA) dust continuum observations of 13 bright sub-millimeter sources previously revealed by the instrument LABOCA at the APEX telescope in a 140 $arcmin^2$ field of the HzRG MRC 1138-262 at redshift z=2.16. Evidence for this field (named Spiderweb from the alleged filamentary structure) being a galaxy protocluster, meaning a cluster in formation, can be found in literature. ALMA data are imaged with different tapering and weighting schemes, in order to explore the effect of the resolution on the flux recovery. The final maps reach a sensitivity of ≈ 0.17 mJy, and we detect 41 (34) SMGs with a S/N>3 (>5). For two LABOCA sources, we found no ALMA detection in the corresponding pointing. In the other 11 cases, ALMA sub-arcsec resolution revealed that the single-dish LABOCA sources are composed by a blend of at least two sources (3.7 on average, higher than commonly found in literature). For each ALMA source we measured both the peak flux and fixed aperture, integrated flux: comparing the two gives hints on whether or not the source is resolved. We also found that using the maps obtained with heavy tapering, for 8 out of 11 cases, summing up the fluxes of the individual ALMA sources we recover the 870 μm flux measured by LABOCA. In addition, we searched for counterparts at other wavelengths, exploiting the wealth of multi-wavelength data available for this field. We find that a fraction of our sub-millimeter population is obscured in the optical/NIR regime, suggesting that this class of objects should be accounted for when constraining the star formation rate density of the Universe, which is typically estimated through optically-selected samples. Finally, we compute the number counts and find that within the inner 13 $arcmin^2$ region, cumulative counts for sources with flux densities >2 mJy show an overdensity of a factor $\approx$9 above blank fields in literature. The overdensity is much less marked when we consider a wider area of the original LABOCA map. In conclusion, the evidence reported in this thesis supports the hypothesis of the Spiderweb field hosting a protocluster in formation, with its core within the 13 $arcmin^2$ region.

Contents

1 Introduction and Motivation 5
- 1.1 The physics of sub-mm emission . . . 5
- 1.2 Sub-mm observations . . . 7
  - 1.2.1 Negative K correction . . . 7
  - 1.2.2 Other applications of submm measurements . . . 8
- 1.3 Source confusion and Interferometry . . . 10
  - 1.3.1 The limits of single-dish instrumentation . . . 10
  - 1.3.2 Interferometry . . . 11
  - 1.3.3 Deconvolution . . . 13
  - 1.3.4 Atacama Large Millimeter/sub-millimeter Array . . . 15
- 1.4 SMGs, or Distant Star-Forming Galaxies . . . 15
  - 1.4.1 SMGs and red sequence galaxies . . . 17
- 1.5 Galaxy protoclusters . . . 18
  - 1.5.1 The Spiderweb Galaxy Protocluster . . . 19
- 1.6 Motivation . . . 24

2 Datasets and methodology 26
- 2.1 Dataset . . . 26
  - 2.1.1 ALMA data . . . 26
  - 2.1.2 Observations . . . 26
  - 2.1.3 Data reduction . . . 27
- 2.2 Source extraction . . . 28
  - 2.2.1 Noise computation . . . 28
  - 2.2.2 Source detection . . . 30
- 2.3 Number counts . . . 33
- 2.4 Multi-wavelength data . . . 35
  - 2.4.1 MW data . . . 36

3 Results 39
- 3.1 Source catalogue . . . 39
- 3.2 Multiplicity . . . 43
- 3.3 Flux measurements . . . 47
- 3.4 Flux comparison with LABOCA . . . 51
- 3.5 Counterpart matching . . . 56
  - 3.5.1 NIR/Optical counterpart matching . . . 58
  - 3.5.2 FIR cross-identifications . . . 59

3.5.3 Radio counterparts 60
3.5.4 HAEs counterpart matching 62

4 Number counts **65**
4.1 Number counts in literature 66
4.2 ALMA number counts 68

5 Discussion and Outlook **76**

References **81**

A Detections and flux analysis **85**
A.1 ALMA flux maps 85
A.2 Flux measurements 92

B Multi-wavelength gallery **98**
B.1 HST/ACS/WFC (814 nm) 98
B.2 HST/NICMOS/110W (1.1μm) 99
B.3 HST/NICMOS/160W (1.6μm) 99
B.4 VLT/HAWK-I/Y (1.0μm) 100
B.5 VLT/HAWK-I/H (1.6μm) 101
B.6 VLT/ISAAC/K_s (2.1μm) 103
B.7 Subaru/MOIRCS/NB2071 (2.1μm, narrow band) 104
B.8 Subaru/MOIRCS/K_s (2.1μm) 105
B.9 Spitzer/IRAC/ch1 (3.6μm) 106
B.10 Spitzer/MIPS (24μm) 107
B.11 VLA 1.4GHz 108

Chapter 1

Introduction and Motivation

At its dawn, after the epoch of inflation, the observable Universe formed from plasma almost uniformly distributed. This theory was supported by Boomerang and the COBE missions (Crill et al. 2003, Mather et al. 1990) and later by the renowned CMB spectrum images collected by the space probes WMAP (Bennett et al. 2013) and Planck (Lamarre et al. 2003), that gathered flux coming from the last scattering surface and found a high degree of isotropy. Then, baryonic matter started to follow the underlying DM structure, arranging into clumps: these clumps eventually reached the Jeans mass and started to collapse, fragmenting into smaller pieces of about $10^2 - 10^3 M_\odot$, whose furher growth led to the first stellar groups. A wide range of physical mechanisms are involved in this process, from general relativity (GR) to gas dynamics and gas cooling, to nuclear reactions and energy transfer models. Together with the even wider range of initial conditions and due to the non-linear nature of most of the aforementioned processes, modelling the structure of the Universe is cumbersome and can lead to an incredibly wide range of results.

Galaxy formation can be studied by attempting to reproduce the observed Universe via analytical models, or even numerical simulations, constrained by observations of the current components of the Universe. The most common observables in this regard are stellar and molecular mass, chemical composition and morphology of the galaxies, and of course direct observation of the emission coming from the early Universe. The history of direct observation of the light of distant galaxies started almost 70 years ago, using optical telescopes, and more recently radio telescopes. Nowadays, astronomers can exploit the full wavelength range, from the lowest energy radio waves, up to high-energy radiation like γ rays. Combining all this complementary information can help us progress in understanding the physical processes at work.

1.1 The physics of sub-mm emission

This work is based on sub-mm continuum observations from the thermal emission of dust.

There are two main sub-mm emission sources from galaxies: thermal continuum emission from dust grains (99% of the total energy budget of the sub-mm and FIR waveband) and line emission from atomic and molecular (rotational) transitions in the interstellar gas (Blain et al. 2002). For instance, carbon monoxide (CO) and ionised carbon (CII) are effective tracers of molecular gas, the latter showing evidence of being more efficient at high redshift (Carilli & Walter 2013). Molecular gas are the fuel for star formation, therefore it is important to keep it into account. Line emission from molecular rotational levels or atomic fine-structure transitions can be used to infer physical conditions within molecular clouds, besides estimating redshift or deriving the properties of the galaxy, like metallicity and gas content.

However, in this work we analyse thermal sub-mm emission, coming from obscured galaxies, where young, massive stars lie within dust clouds. Intense optical/UV radiation radiated by young stars heats up dust grains up to tens of degrees. This energy is then emitted in the form of a blackbody spectrum, peaking around $100\mu m$. Such spectrum is featureless, thus revealing very little about the physical conditions of the sources enshrouded in gas.

In order to describe the emission from dust grains we need at least two parameters: dust temperature T_d and emissivity ϵ_ν. Dust in galaxies is formed by different phases (or components), each with its own density and temperature. However, we can use just one T_d as collective parameter. Modelling the Spectral Energy Distribution requires to solve the Radiative Transfer equation.

$$\frac{dI_\nu}{ds} = -k_\nu I_\nu + \epsilon_\nu \tag{1.1}$$

This equation describes the change in intensity of radiation travelling through a slab of material of thickness ds. k_ν is the frequency-dependent absorption coefficient. Emissivity ϵ_ν expresses the emitting power of the dust cloud. In the Rayleigh-Jeans regime (long wavelength) it can be modelled with a volume-averaged (often we lack resolved images of galaxies) power law function $\epsilon_\nu \propto \nu^\beta$, where β is the dust emissivity spectral index. Usually, when solving this equation we change coordinates and switch to optical depth

$$d\tau_\nu = -k_\nu ds. \tag{1.2}$$

A possible solution to the Radiative Transfer equation would thus be

$$I_\nu \propto [1 - e^{-\tau_\nu}]B_\nu \tag{1.3}$$

where B_ν is the Planck function. In the optically thin material approximation ($\tau_\nu << 1$), we get

$$I_\nu \propto \tau_\nu B_\nu. \tag{1.4}$$

Moreover, the optical depth τ_ν is a multiple to emissivity (Blain et al. 2002), so we can write $I_\nu \propto \epsilon_\nu B_\nu$. In the RJ limit,

$$B_\nu = 2kT_d\nu^2/c^2 \tag{1.5}$$

This yields

$$I_\nu \propto \nu^{\beta+2}. \tag{1.6}$$

Observations on sub-mm galaxies Spectral Energy Distribution (SED) typically suggests $T_d \approx 40K$ (Kovács et al. 2006, Casey 2012) and $1 < \beta < 2$ (Blain et al. 2002, Casey, Narayanan & Cooray 2014). Indeed, scattering theory predicts β=2 at longer wavelengths, while β=1 better matches the general trend of extinction curves describing the absorption of UV radiation by ISM (Calzetti et al. 2000).

1.2 Sub-mm observations

This work is based on a direct observation of the galaxy formation process, to which we have gained access in a "new" window, that is the sub-millimeter range $[200\mu m - 1mm]$, thanks to the new powerful instrumentation developed in the last couple of decades. Almost 30 years ago Blain & Longair (1993) predicted that sub-millimeter observations could provide important insights into the nature of galaxies in the early Universe beyond the reach of optical and near-infrared surveys. If early-star forming galaxies contain dust, then optical/UV-photons emitted by these young stars are absorbed by dust clouds and reprocessed through the far-infrared, thus being pushed into the sub-millimeter regime (Hildebrand 1983). In particular, sub-mm range probes the long-λ tail of the cold dust continuum spectrum, associated to carbonaceous and silicate component.

Past observations show that some high-redshift sources are emitting a large fraction of their bolometric emission in the rest-frame far-infrared, which is detectable in the sub-millimeter, with infrared luminosities that may even exceed local ultraluminous infrared galaxies (ULIRGs, $L \approx 10^{12} L_\odot$, first unveiled in the Infrared Astronomy Satellite (IRAS) all-sky survey in the 80s (Sanders & Mirabel 1996). We now know that the FIRB (Far Infrared Background) constitutes up to half of the energy density budget associated to star formation activity integrated through the lifespan of the Universe (Hughes et al. 1998). Detection in this range was transformative in the field of extragalactic astronomy, as it also offers another window on structure formation in the high-redshift universe.

1.2.1 Negative K correction

Sub-mm observations are especially interesting for astronomers. In fact, they offer a unique probe of the distant Universe, not only because of scientific significance, but also due to an observational advantage, the so-called *negative k-correction* (Blain & Longair 1993). Usually, as an object moves at further redshift, the measured flux is dimmer (since it is a function of distance) and we investigate a different portion of the SED, which moves to the right as redshift grows. Sub-mm galaxies enjoy the property of negative k-correction: their FIR SED peaks around 100μm to 200μm, so when we measure high-redshift objects at sub-mm wavelength we are picking up emission from the peak. Since the SED peaks at long wavelengths and the spectral energy distribution is steep enough, sources of similar intrinsic brightness appear brighter as they go to higher z. In other words, as the spectrum gets more and more redshifted (cosmological redshift), the dimming is compensated for by the rise of the Rayleigh-Jeans tail, bringing an increase of radiation field as it is redshifted through the band. This is what makes sub-mm emission so interesting on an observational level. Suppose we have a galaxy of fixed luminosity: as redshift increases, flux density S_ν should decrease like $(1+z)^{-4}$. In fact,

$$S_\nu = L_\nu / 4\pi D_L^2 \tag{1.7}$$

where D_L is luminosity distance and $D_L \propto (1+z)^2$. Then, using Equation 1.6, flux density can be written as

$$S_\nu \propto \nu^{\beta+2} / 4\pi D_L^2 \propto [\nu_0(1+z)]^{\beta+2} / (1+z)^4 \tag{1.8}$$

where ν_0 is the rest frequency. This means that

$$S_\nu \propto (1+z)^{\beta-2}. \tag{1.9}$$

As $\beta \approx 2$ at this wavelength, we can conclude that flux density will be roughly redshift-independent. This means that two sources with the same intrinsic luminosity can be observed with roughly the same flux density at 870μm at $z \approx 0.5$ and $z \approx 10$. For example, an ULIRG (with $L_{IR} \approx 10^{12} L_\odot$) would be observed with a flux density of 1–2 mJy at 870μm over most of cosmic history (Blain et al. 2002). For this reason, flux-limited surveys in this band offer the possibility to sample large cosmic volumes, potentially probing well into the epoch of re-ionization. Figure 1.1 shows how the flux density is naturally redshift-dependent and sources get dimmer at higher redshift at different wavelengths except for 850μm. At that λ, flux density is independent on redshift and sources maintain constant flux density even at high redshift. Beyond $\approx$3mm, the emission of galaxies gets dominated by other physical processes, like synchrotron and free-free emission: this changes the way we model flux density and the K-correction stops providing this compensation.

1.2.2 Other applications of submm measurements

Other than being a window on galaxy formation at high-redshift, this wavelength regime also offers other uses. In case of lack of spectroscopic information about a source, photometric redshift can be used, which is the estimation of redshift based on the recession velocity estimated by measuring the shift in the observed SED with respect to the assumed SED template. This method is typically carried out in the UV-optical-NIR. The dust emission of galaxies in the sub-mm depends on temperature: the peak shifts at longer wavelength at decreasing temperature; therefore, there is a degeneracy between temperature and redshift. This is a source of uncertainty for photometric redshift, unless we are able to extract information about the intrinsic dust temperature

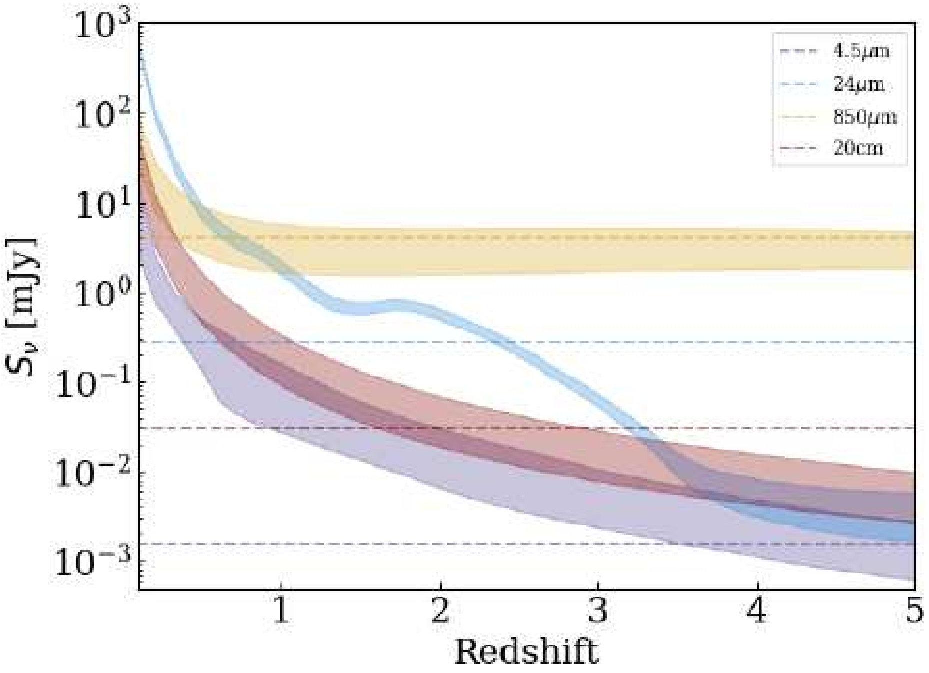

Figure 1.1: Expected flux density of an average SMG (from ALESS survey) at different wavelengths redshifted from 0 to 5 (Shim et al. 2022). Expected flux densities are shown by the shaded areas, which represent an average of different spectral templates of SMGs. See how the yellow band, associated to 850 μm band, displays a strikingly constant flux density as a function of redshift. Horizontal dashed lines are the 5σ flux limits in the corresponding multiwavelength datasets.

of the source. However, photo-z estimated on far-infrared SEDs still remains a reliable technique.

Moreover, dust can be studied to derive SFR. The more young stars, the more energy is absorbed by dust, the stronger the emission we measure. Calibrated empirical relations are available in literature (Kennicutt 1998, see Chapter 5).

Other applications include empirical correlation between the radio and far-IR flux densities of low-redshift galaxies. Assuming this relation also holds at high redshift, the sub-mm-selected galaxies should be detectable in the deepest radio images, depending on the sensitivity. The reason of this correlation lies in the fact that young stars on one hand heat up the dust, on the other hand eventually explode as supernovae. In supernovae, synchrotron emission from accelerated relativistic electrons causes radio emission.

1.3 Source confusion and Interferometry

1.3.1 The limits of single-dish instrumentation

The first extragalactic sub-mm/mm surveys were carried out with bolometers. A bolometer is a device based on the principle of temperature change of a receiver absorbing incident radiation. Measuring temperature is thus also a measure of the intensity of radiation. Bolometers are instruments that measure wavelength-integrated flux, since heating is independent of frequency.

SCUBA (Submillimeter Common-User Bolometer Array) started operation at JCMT back in 1997, probing two bands simultaneously (450, 850 μm) in a 2.5 arcmin-wide field, and providing an excellent leap forward in probing sub-mm emission (Holland et al. 1999). MAMBO (Max-Planck Millimeter Bolometer Array) is technically similar to SCUBA, but investigating the 1.25 mm band. We also mention LABOCA (Siringo et al. 2009), a multichannel bolometer array built for continuum observations, installed in 2006 in the Cassegrain cabin of the APEX telescope and started operations in 2007. The optimised observing frequency is 870μm (345 GHz). The bolometer employs 295 channels, with an angular resolution of 18.6" and a total FoV of 11.4$'$.

The surveys carried out in the 2000s by these instruments revealed a population of very luminous, high-redshift galaxies, responsible for a significant fraction of the energy generated over the history of the Universe (Smail, Ivison & Blain 1997, Hughes et al. 1998).

The most important reason for the delay in the blooming of sub-mm astronomy is the technical challenge of measuring flux at long wavelengths. In general, angular resolution of a telescope of diameter D is approximately given by

$$\theta \approx \lambda/D \tag{1.10}$$

which means that the smallest angular scale that the instrument can resolve is given by the ratio between the wavelength of the observed radiation and the diameter of the aperture of the telescope. In other words, the size of the telescope represents an intrinsic limit to its resolving power. For this reason, long λ limits the resolution of the telescope: to get a 0.5 arcsec resolution, common nowadays in the optical regime, at 1mm we would need apertures of about 400 meters, while currently the technical limit of single-dish radio instrumentation is about 30m (IRAM 30m telescope). For example, if we want to effectively probe the dawn of galaxy evolution, we need to go at z>2. To give a quantitative feeling of the resolution we need for this task, we point out that at z=2.2 the scale is around 8kpc/arcsec. Average size of a galaxy is of the order of 2-3 kpc (van der Wel et al. 2014), therefore at this redshift it would have the size of about 0.3 arcsec. This is why we need at least such resolution to explore the morphology of high-z galaxies.

Moeover, efficient sub-mm observations can only be carried out in high mountain sites, where the absorption due to the atmospheric layers is minimized, and yet only in selected wavelength windows.

Faint unresolved sources piling up on the scale of the observing beam constitute another significant problem for observations in sub-mm band. In fact, by lying below the detection limit, they mix up with the stochastic fluctuations of the background, thus enhancing noise estimations (Smail et al. 2002). This is called source confusion and is due to the relatively coarse resolution available with single-dish facilities. For a given beamsize, the confusion limit is the flux density threshold at which the surface density of detections above that threshold multiplied by the beamsize is equal to 1 (Casey, Narayanan & Cooray 2014). For instance, SCUBA detection at 850 μm do not go below the threshold of 2mJy, making it difficult to identify the source.

That is why the astronomical community had to rely on other methods to deal with sub-mm and radio observations. While single-dish apertures are limited by their size, interferometers can dramatically enhance the resolution of images.

1.3.2 Interferometry

Interferometry is based on the principles of interference of light: Albert Michelson was awarded the Nobel Prize in Physics for the invention of the first interferometer in 1907. One year later, Gabriel Lippman won the Prize for his findings about interference.

While the electromagnetic field simply sums up in a vectorial manner (principle of Superposition), intensity is not simply the sum of the intensities of single sources, but it includes also an extra term, that can enhance or dampen the total intensity. In the simple case of two sources, intensity at a given point in space is given by

$$I = I_1 + I_2 + 2\sqrt{I_1 I_2}\cos\delta. \tag{1.11}$$

where δ is the phase difference between the two light beams. Since δ changes as a function of the path difference between the two sources, the observer gathering light will measure the characteristic fringe pattern, where the intensity is maximized at certain angles and damped at others.

Interferometers make use of interference to recover the properties of light. In fact, at odds with optical image synthesis, interferometry works on the Fourier-transform spatial frequencies plane rather than the optical plane, where the original image coordinates are reconstructed. The data we get from interferometers are called *visibilities*, and they quantify the degree of correlation between light waves. Correlators are devices that are able to output visibility, which depends on the so-called *baseline*. The baseline is a spatial scale that in short corresponds to the distance between different antennas in the interferometric array, linked by the correlator. Figure 1.2 represents schematically how signals from different array elements are combined by the correlators to assemble the image. Baselines regulate the spatial resolution we are able to access: by coupling different elements of the antenna array, we access to different angular scales. The finest resolution would be given by λ/B_{max}, B_{max} being the largest baseline available in the array.

The key relation connecting flux density of a source to the output of correlators is expressed by the *Wiener-Khinchin theorem*,

$$S(\nu) = \int R(\tau) e^{-2\pi i \nu \tau} d\tau \tag{1.12}$$

where $\tau \propto \vec{B} \cdot \vec{s}$ is the *delay time*, and $\vec{s}$ is the direction of the light ray. Since the latter rotates with the Earth, the correlation pattern varies with time. Thanks to this equation, that substantially expresses a Fourier Transform, we can recover the flux density of the source. In principle, if we knew the *correlation function* or *visibility function* $R(\tau)$, we would be able to quickly recover the flux density. However, in practice, visibility is sampled in a discrete manner, therefore the recovered image is polluted by the sampling function: such image is called *dirty image*, which corresponds to the true image convolved with the Fourier Transform of the sampling function (*dirty beam*). Thus, in order to recover the true image, a deconvolution process is needed to remove the dirty beam.

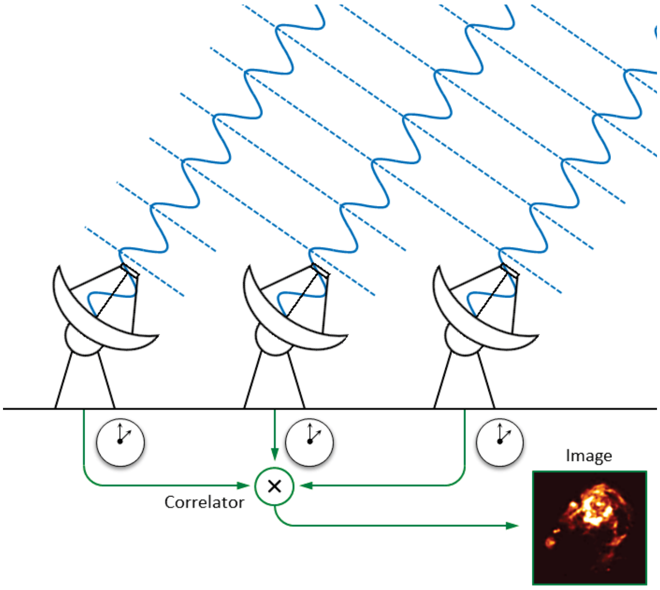

Figure 1.2: Scheme depicting the correlation process (Schediwy 2013). Antennas observe the sky and the signal they observe is assembled in the correlator to reconstruct the image.

We also mention the concept of *beam* in radio observations: the response of an antenna (ie the element of an interferometric array) is described by a power pattern describing the antenna response (sensitivity) as a function of the angle from the center of the pointing. Therefore, it is a function of sky coordinates and antennas are usually characterized by a beamed response function. The power pattern is usually larger for a certain range of sky coordinates: this range is called *main beam* or *main lobe*. However, part of the power is always lost in the *sidelobes*, meaning secondary peaks of the power pattern pointing

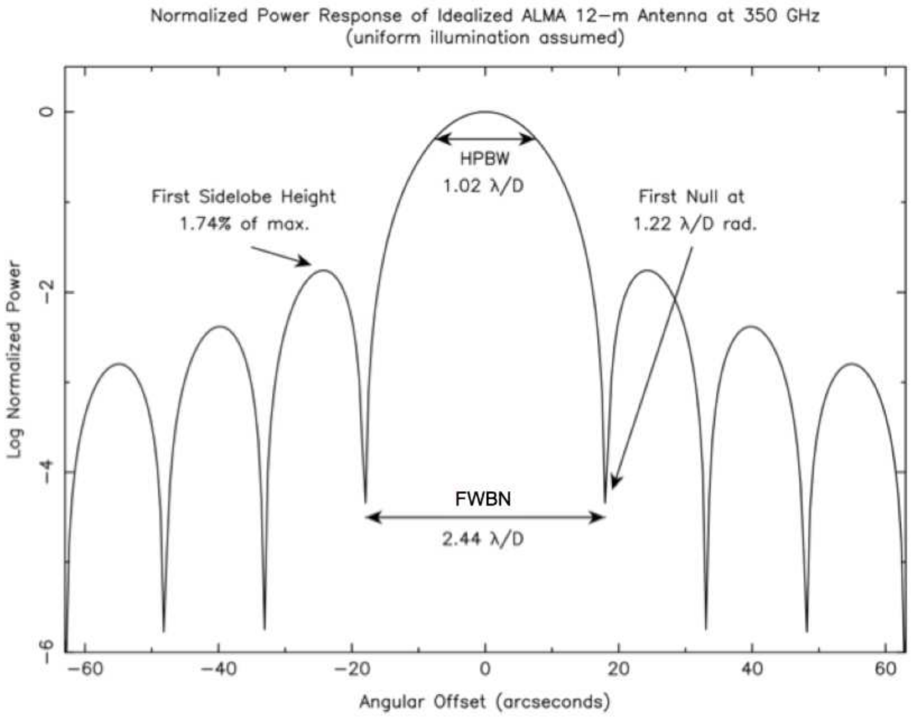

Figure 1.3: Normalized 1-D antenna power response for an ALMA 12-m antenna uniformly illuminated at 350 GHz. The power is expressed in log units to emphasize the sidelobes. The HPBW of the primary beam (central bell) is about 1.02 λ/D and the FWBN is 2.44 λ/D. The angle of the first null, where we have destructive interference, is found at 1.22 λ/D. Image taken by the ALMA Cycle 7 Technical Handbook (https://arc.iram.fr/documents/cycle7/ALMA_Cycle7_Technical_Handbook.pdf)

a direction other than that of the source. Sidelobes can be reduced but are intrinsic to radio antennas and interferometry. The response function of a 12-m antenna from the Atacama Large Millimeter Array (ALMA) is plotted in Fig. 1.3, where we can see both the main lobe and the side lobes.

Advantages of interferometry include high angular resolution, large collecting areas (that depend on the sum of the areas of each dish in the array and the number of visibilities employed), the possibility to filter out extended emission and large FOV.

1.3.3 Deconvolution

The procedure trough which we assemble the correlation signals from an array of antennas to construct images is called aperture synthesis: in this process, to each spatial configuration inside the array, we can associate a component of the Fourier transform of the spatial distribution of the surface brightness of the target. Aperture synthesis fruited the 1974 Nobel prize to Sir Martin Ryle for his pioneering contribution to Radio Astronomy.

One of the step of aperture synthesis is deconvolution, or the removal of the response function of the instruments. This task is often entrusted to specialised algorithms. The most widely used software for radio data processing is CASA[1], the Common Astronomy Software Applications package, developed by the National Radio Astronomy Observatory (McMullin et al. 2007). It is the primary program to support the data reduction and imaging pipelines of radiotelescopes like ALMA and VLA. One of the key tasks of CASA is the CLEAN algorithm, the most popular method for reconstructing a model image based on interferometric data. CLEAN is an iterative algorithm removing dirty beam from the observed brightness of a radio source, developed in 1974 by Jan Högbom, and later improved throughout the years.

The "clean" task of CASA (today *tclean*) for data reduction offers the option to select a suitable weighting scheme to weight the visibilities. Adding a weighting scheme corresponds to slightly altering the response function of the instrument in order to adapt data reduction to the observer needs (like maximize the signal-to-noise or make sure to resolve the source to study its morphology). The available weighting schemes are:

- **natural weighting** scheme gives equal weights to all visibilities: this preserves the natural response of the instrument and maximizes S/N;
- **uniform weighting** gives equal weight to the same spatial frequencies and maximizes resolution, ideal for high signal-to-noise sources;
- **Briggs** (or **robust**) **weighting** produces a PSF which is intermediate between natural and uniform weightings depending on selected tuning parameter.

Moreover, we should also mention uv-tapering: it has a similar role as the weighting scheme, and it is implemented in order to weight down some specific spatial frequencies. Higher spatial frequencies are down-weighted to suppress possible artifacts arising from poorly sampled areas in the frequency plane. Tapering is indeed meant to suppress small-scale sidelobes, thus increasing the size of the synthesized beam width and increasing the sensitivity to the large-scale emission. Snapshots observations are often characterized by big sidelobes: tapering is often employed to smooth them out. Tapering also cause noise to grow.

One can choose a threshold for the tapering, meaning a frequency limit above which the contributions are suppressed. Tapering also impacts the resolution of the final image: in fact, different taperings will access different spatial scales in the image. We will see how this kind of choices can affect flux measurements in Section 3.4. A common choice is applying a Gaussian taper to the spatial frequency grid, in the form of a Gaussian in uv-space (eg. units of lambda).

---

[1] https://casa.nrao.edu/

1.3.4 Atacama Large Millimeter/sub-millimeter Array

Technical specs

ALMA is currently the most powerful instrument available for sub-mm observations. It was commissioned in 2006 in the Atacama Desert in Chile and started observations in 2011, in an exceptionally high plateau, which provides a suitable environment for interferometry measurements, being dry with low precipitable water vapour. It is composed of 54 12-m antennas and 12 7-m antennas. The spectral range is divided into 10 main frequency bands, covering a range that goes from 3mm to 315 μm (84-950 GHz). The angular resolution is approximately given by $\theta = 1.33\lambda/B_{max}$. Baselines can reach 15 km (enabling a limiting resolution of 0.015” at 300 GHz).

The 10 receiver bands have different widths: in each band, the correlators produce two "sidebands", separated by 8 GHz and 4GHz wide each; each sideband can be further divided into multiple basebands, typically 2, so in total one has 4 basebands. ALMA data undergo all the important calibration steps: phase, bandpass, and polarization calibration. Different correlation combinations are called modes: ALMA offers up to 70 modes.

ALMA FoV is determined by the size of antennas and by the observing frequency, while it does not depend on array configuration. To estimate the FoV, we can fit ALMA primary beam with a Gaussian profile. The FWHM of the primary beam will be the size of the FoV. However, note that sensitivity is not uniform across the pointing, but it is roughly bell-shaped, with a maximum at the center and minima towards the edges. This is why flux maps are primary-beam corrected, meaning that they are multiplied by a correction factor to account for the shape of the response function.

Science with ALMA

ALMA scientific goals include the observation of high-z galaxies, proto-stellar nuclei, nearby star-forming galaxies, circumstellar disks, exoplanets, solar system objects.

However, ALMA is best suited to observe around the redshifted continuum emission from the peak of the dust thermal emission. In fact, as we know, negative k-correction makes the submillimeter brightness nearly independent of redshift up to z=10. Dust continuum emission is used to trace dust mass and temperature, and thus obscured star formation activity. Thanks to its high-resolution images ALMA is an excellent tool to observe SMGs.

Moreover, ALMA can also detect molecular and atomic emission lines, that can help us trace cold and warm components of gas clouds in distant galaxies.

1.4 SMGs, or Distant Star-Forming Galaxies

The sub-mm background represents one of the cleanest measures of activity in the distant Universe. In this wavelength regime, we are able to detect the so-called *obscured* star formation activity, due to young stars covered in dust.

After heating up, the dust cloud produces thermal emission, that we detect in the sub-mm. Obscured starburst events are common in the galaxy populations detected in the sub-mm go under the name of DSFGs (Distant Star-Forming Galaxies) or SMGs (Sub-Millimeter Galaxies) from the wavelength range in which they're found. Their importance was first highlighted by Smail, Ivison & Blain (1997) and Hughes et al. (1998). These objects are characterized by intense infrared luminosities ($10^{13} L_{\odot}$) and SFR of the order of $10^3 - 10^4 M_{\odot} yr^{-1}$, but due to strong dust obscuration they are not detectable in the optical or NIR regimes (Dannerbauer et al. 2002, Dannerbauer et al. 2004, Genzel et al. 2003, Greve et al. 2005). Figure 1.4 shows the typical SED of a Submillimeter Galaxy, emitting a consistent amount of flux at the peak ($\approx 100\mu$m). The full spectrum ranges from 10μm to 1mm.

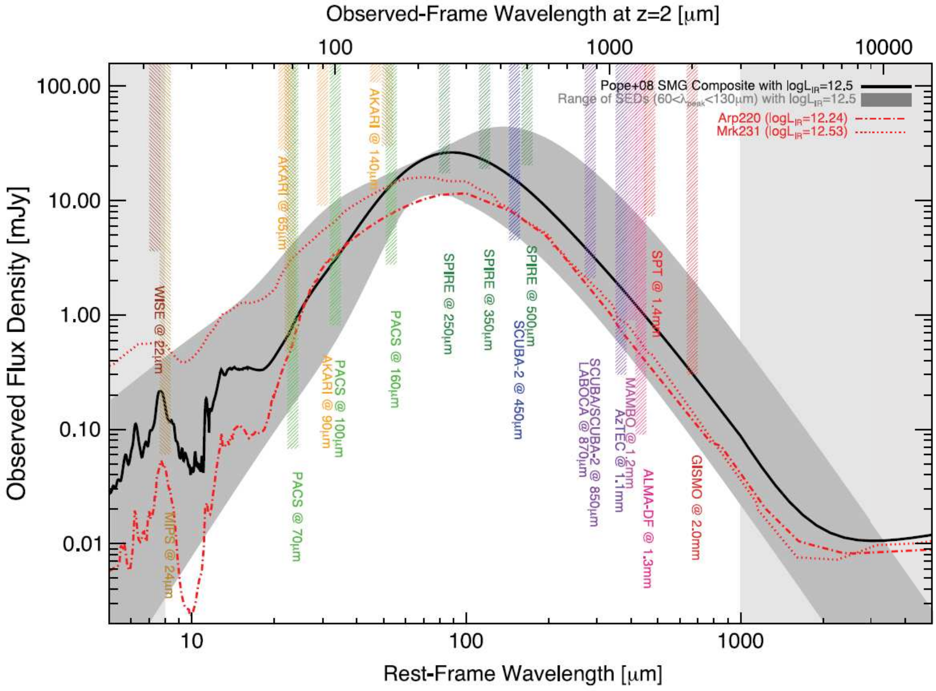

Figure 1.4: SED for a SMG (Casey, Narayanan & Cooray 2014). Black line represents the SED for a $500 M_{\odot}/yr$ SMG. Gray band covers a range of SED types at fixed infrared luminosity (10^{25} $L_{\odot}$ with peak between 70 and 130 μm). Dashed and dotted red lines correspond respectively to models for local galaxies Arp220 and Mrk231. The vertical shaded, colored bands represent the operating range of a number of FIR instruments.

Sub-mm emission is characterised by a significant surface density, indicating that the luminosity function of distant sub-mm galaxies is larger than that of low-redshift galaxies, and undergoes a very strong evolution (Blain et al. 2002, Casey, Narayanan & Cooray 2014). It is possible to estimate that the density of high-redshift galaxies with such luminosity excess is 400 times greater than at z=0.

Moreover, the distribution of the volume-averaged SFRD (Star-Formation Rate Density) of the Universe peaks at redshift $z \approx 2$: Fig.1.5 shows in fact how the star formation rate density of the Universe increases from z≈0 to z≈2, where it reaches its peak, and then decreases from z≈2 to the epoch of the cosmic reionization. Since the contribution of infrared luminous galaxies to the global SFR density increases continuously up to z= 2 and 3 (Casey, Narayanan & Cooray 2014), understanding the physical nature of SMGs is crucial for constructing a self-consistent galaxy evolution theory. SMGs may represent a major contribution of star formation at high redshift, where obscured star formation is easier to detect with respect to unobscured star formation.

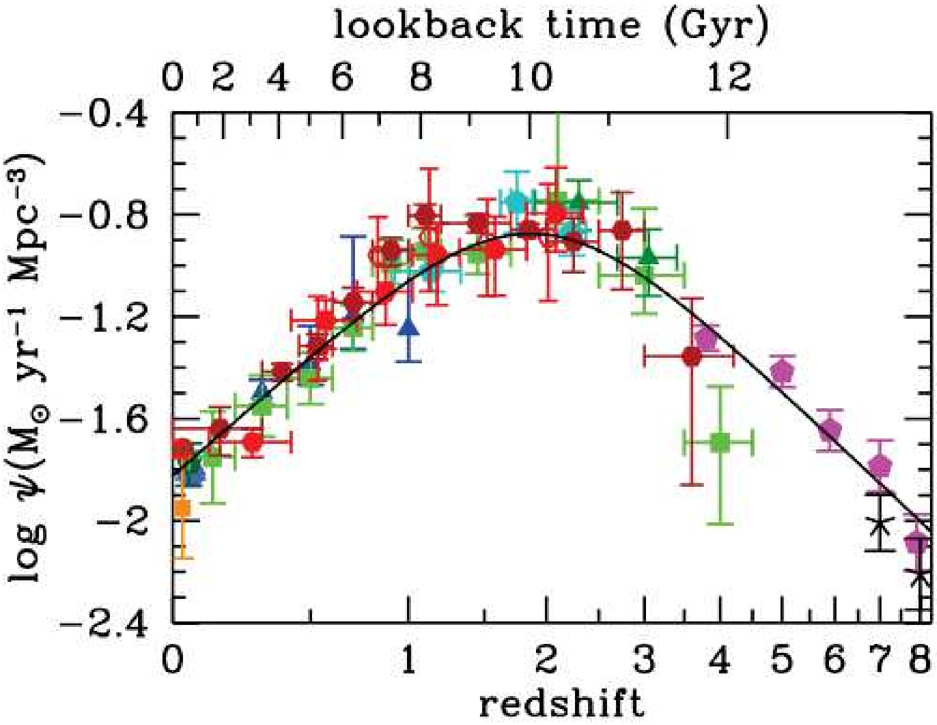

Figure 1.5: History of cosmic star formation density from FUV (green and purple dots) and IR (red). Solid curves in the three panels plots the best-fit SFRD (Madau & Dickinson 2014). This plot shows how the intensity of star formation activity per unity peaking at redshift z>2.

1.4.1 SMGs and red sequence galaxies

One of the hot topics in astrophysics today is the origin of the so-called "red sequence" of galaxies. These are massive, early type, elliptical, red galaxies that are not forming stars and have been passively evolving since redshift z=2, when star-formation activity was somehow quenched. The issue of when and how the ancestors of the members of the red sequence arose in the early Universe is still under investigation.

Massive ellipticals dominate the core of local galaxy clusters: they are characterized by very homogeneous properties and have very old stellar populations, suggesting that they formed in relatively short timescales in the past.

This is one of the reasons why SMGs are considered to be suitable ancestors of members of the red sequence, since they are characterized by a quick build-up of their stellar mass budget in short times.

One of the aims of the study of SMGs is indeed bridging the stellar activity phase at high redshift with red sequence galaxies. In order to transit from a SMG phase to red sequence galaxies, we need some physical process to quench star formation. One of these processes may be the merger of two gas-rich galaxies: in the early phase of the merger, the gas is brought into the dusty center of the system and a burst of star formation is triggered, shining as SMG: then the system goes through a quasar phase, that can be traced as dust-obscured AGN activity. Finally, we get the massive, passively-evolving galaxy. Oteo et al. (2017) suggest that elliptical galaxies form in intense high-redshift starbursts, that are represented by different SMG phases, meant as brightness classes. Local, massive galaxies form in a SMG phase at high redshift (z=4 to 6), while less massive ellipticals in the Local Universe arise from less intense sub-mm bursts, possibly at more intermediate redhift (z≈2-3) .

Other than intragalactic phenomena like AGN and supernova feedback, possible quenching mechanisms include intergalactic occurrences like tidal stripping, which is the removal of gas or stars due to tidal gravitational interaction with another large galaxy (Spilker et al. 2022). Another possible factor is ram pressure, meaning the pressure exerted by the the hot intra-cluster medium on galaxies floating inside of it. This pressure may cause gas outflow where the gas is weakly gravitationally bound (Steinhauser, Schindler & Springel 2016).

Observations of molecular lines provide the mass of the molecular gas component of a galaxy, which together with SFR (that dust continuum can provide) can yield an estimate of gas-depletion timescale, which can be broadly defined as the ratio M_{gas}/SFR. Such timescale can provide insights on whether and when the distant source may become a massive elliptical (Carilli & Walter 2013).

1.5 Galaxy protoclusters

Besides contributing to determining star formation rate and helping to constrain galaxy formation and evolution models, SMGs can also help us understanding cluster structure evolution. Clusters of galaxies are the most massive and largest gravitationally bound objects in the Universe. They play a key role in many different aspects of extragalactic astronomy and cosmology, such as cosmological models, structure formation scenarios and dark matter properties. Clusters can be defined as virialized structures that appear as overdensities of galaxies, with total mass of about $M = 10^{14} M_{\odot}$ (Bower & Balogh 2004, Trudeau et al. 2022). These objects are dark matter dominated (≈85%): the bulk of the baryonic mass budget amounts to hot gas (Intra-Cluster Medium ICM, that can be detected in the X-ray band). Mature clusters are also characterized by a prominent red sequence.

The study of clusters can bring information about galaxy evolution and cosmology. Clusters cores and halos represent very different environments in terms of density: these properties make cluster a suitable laboratory where to investigate the effect of galaxy interactions and galaxy evolution. For instance, from galaxy clusters we can also constrain cosmological parameters: in fact, number density of clusters strongly depends on cosmological parameters, mainly Ω_M and σ_8 (Pentericci, Miley & Venemans 2007).

At z>2, we can find the candidate ancestors of clusters. Until twenty years ago, galaxy overdensities were mostly studied through optical/NIR observations, thus only probing unobscured star formation. However, more recently several studies have been reporting excess of SMGs near high-redshift radio galaxies (HzRGs), thus providing evidence for SMGs being possible signposts of overdensity in the early Universe (Stevens et al. 2003, De Breuck et al. 2004, Greve et al. 2007, Priddey, Ivison & Isaak 2008, Stevens et al. 2010, Carrera et al. 2011, Rigby et al. 2013). Such overdensities are referred to as protoclusters: they represent an early stage of cluster evolution (Overzier 2016). As a broad definition, protoclusters are overdensity of galaxies that are approaching gravitational collapse and are bound to become virialized soon.

1.5.1 The Spiderweb Galaxy Protocluster

One of the most famous, documented overdensities of galaxies at high z is the protocluster associated with the radio galaxy MRC 1138-262, sitting at redshift z=2.16, also known as Spiderweb. Lyα and Hα photometric and spectroscopic observations have shown an excess of LAEs with respect to blank fields (Pentericci et al. 2000, Kurk et al. 2001). In literature, there are attempts of identifying sub-mm sources in this field : Stevens et al. (2003) used SCUBA-2 850 μm observations to report a tentative excess of SMGs. However, we point out that SCUBA has a narrow FoV, with diameter of $2'$, corresponding to a physical scale of 1 Mpc at this redshift. Therefore, such results were based on limited statistics. Rigby et al. (2013) presented Herschel SPIRE data from a much larger FOV (400 $arcmin^2$), finding evidence of an excess of sources at $500\mu m$. Nevertheless, recent works with Herschel show the importance of determining the redshift for all the sources associated to the protocluster: Wylezalek et al. (2013) showed that many of the sources in the field of the 4C+41.17 protocluster at z=3 were indeed foreground sources.

In these cases, the authors did not attempt a wide multiwavelength characterization of the detections. A simple way to test the robustness of a source and infer its physical properties is counterpart matching: if images from the same field are available at other wavelengths, then we can look for emission in such maps at the location of the ALMA-detected source. That is where Dannerbauer et al. (2014) brought its major contribution to the study of the Spiderweb field. This paper is built around sub-mm observations of the field, taken with the LABOCA bolometer onboard the APEX telescope with ESO time (ID 084.A-1016(A), PI Kurk) and Max-Planck-Gesellschaft time (ID 083.F-0022, PI Kurk). LABOCA operated at an effective frequency of 345 GHz (870 μm), covering a FoV of 11.4" with with $FWHM = 19"$. Observations were carried

Source Alias	RA(J2000)	DEC(J2000)	$S_{870_{\mu m}}$[mJy]	S/N	z_{phot}	z_{spec}
DKB01	11:41:00.04	-26:30:39.2	9.8±1.5	6.7	2.3±0.7	2.165
DKB02	11:40:53.28	-26:29:14.0	8.1±1.5	5.4	2.7±0.8	-
DKB03	11:40:58.26	-26:30:44.0	7.3±1.5	4.9	2.1±0.6	2.163
DKB04	11:40:46.75	-26:25:39.2	6.8±1.4	4.7	3.6±1.1	-
DKB05	11:40:43.88	-26:23:40.2	8.2±1.8	4.5	2.4±0.7	-
DKB06	11:40:59.54	-26:32:00.7	6.8±1.7	3.9	0.8±0.2	0.028
DKB07*	11:40:48.36	-26:29:14.4	6.7±1.7	3.9	2.2±0.6	2.156
DKB08	11:40:33.88	-26:31:25.6	10.6±2.7	3.9	5.6±1.7	-
DKB09	11:40:40.92	-26:25:56.0	7.1±1.9	3.8	3.6±1.1	-
DKB10	11:40:43.66	-26:22:16.8	11.0±3.0	3.7	3.0±0.9	-
DKB11	11:40:38.48	-26:32:01.4	7.0±1.9	3.6	2.6±0.8	-
DKB12	11:40:57.58	-26:29:33.7	5.0±1.4	3.6	2.1±0.6**	2.17**
DKB13	11:40:48.34	-26:27:48.0	4.4±1.5	3.0	1.3±0.4	-
DKB14	11:40:42.38	-26:27:15.5	5.3±1.8	3.0	1.3±0.4	-
DKB15	11:40:54.26	-26:28:00.0	3.2±1.3	2.4	3.4±1.0	-
DKB16	11:41:02.41	-26:27:46.0	4.2±1.4	2.9	1.9±0.6	2.154

Table 1.1: LABOCA positions and flux measurements from Dannerbauer et al. (2014). Column (1): short LABOCA alias. Column (2): Right Ascension, J2000 format (hh:mm:ss). Column (3): Declination, J2000 format (degrees:mm:ss). Column (5): LABOCA flux with error. Column (6): signal-to-noise ratio. Column (7): photometric redshift derived from the optical, NIR and FIR data. Column (8): spectroscopi redshift (if available). The * sign marks DKB07, which is radio loud galaxy MRC 1318-262, or Spiderweb. The ** sign marks LABOCA source DKB12, for which multiple counterpart with different z_{phot} and z_{spec} were found. DKB12 was not observed in this ALMA follow-up program.

out between August and December 2009 in service mode, under exquisite atmospheric conditions with zenith opacities between 0.2 and 0.3. The bolometer mapped a region of ≈ 140 $arcmin^2$ around the HzRG MRC1138-262, with total integration time of 16.6h. The central part of the LABOCA map achieved an rms noise of 1.3-1.9 mJy. 16 sources were detected overall: twelve of them were classified as secure (S/N $>3.5\sigma$), while the other 4 were labelled as tentative, meaning that they did not achieve the same S/N but had significant counterparts at other wavelengths. The secure category included the sources labelled DKB01 to DKB12, while DKB12-DKB16 correspond to the tentative detections. Positions and flux measurements of the sources are reported in Table 1.1. Figure 1.6 shows the map produced by LABOCA and the 16 sources that were detected (white circles). The 56 $arcmin^2$ subregion within the 1.9mJy noise contour encompasses all sources but DKB08 and DKB10: in this subregion, the number density of sources having flux densities >7mJy was found to be ≈ 0.107 $arcmin^{-2}$, about 2 to 4 times higher than the corresponding cumulative bin in the blank field survey chosen as a reference (Weiß et al. 2009). The estimated SFRD for the LABOCA detections reaches ≈ 1500 $M_{\odot} yr^{-1} Mpc^{-3}$ and is compared to the average value of the SFRD of the Universe reported in Hopkins & Beacom (2006), finding an excess of about four magnitudes. This supports the idea of that the field of the Spiderweb galaxy hosts an overdensity of galaxies.

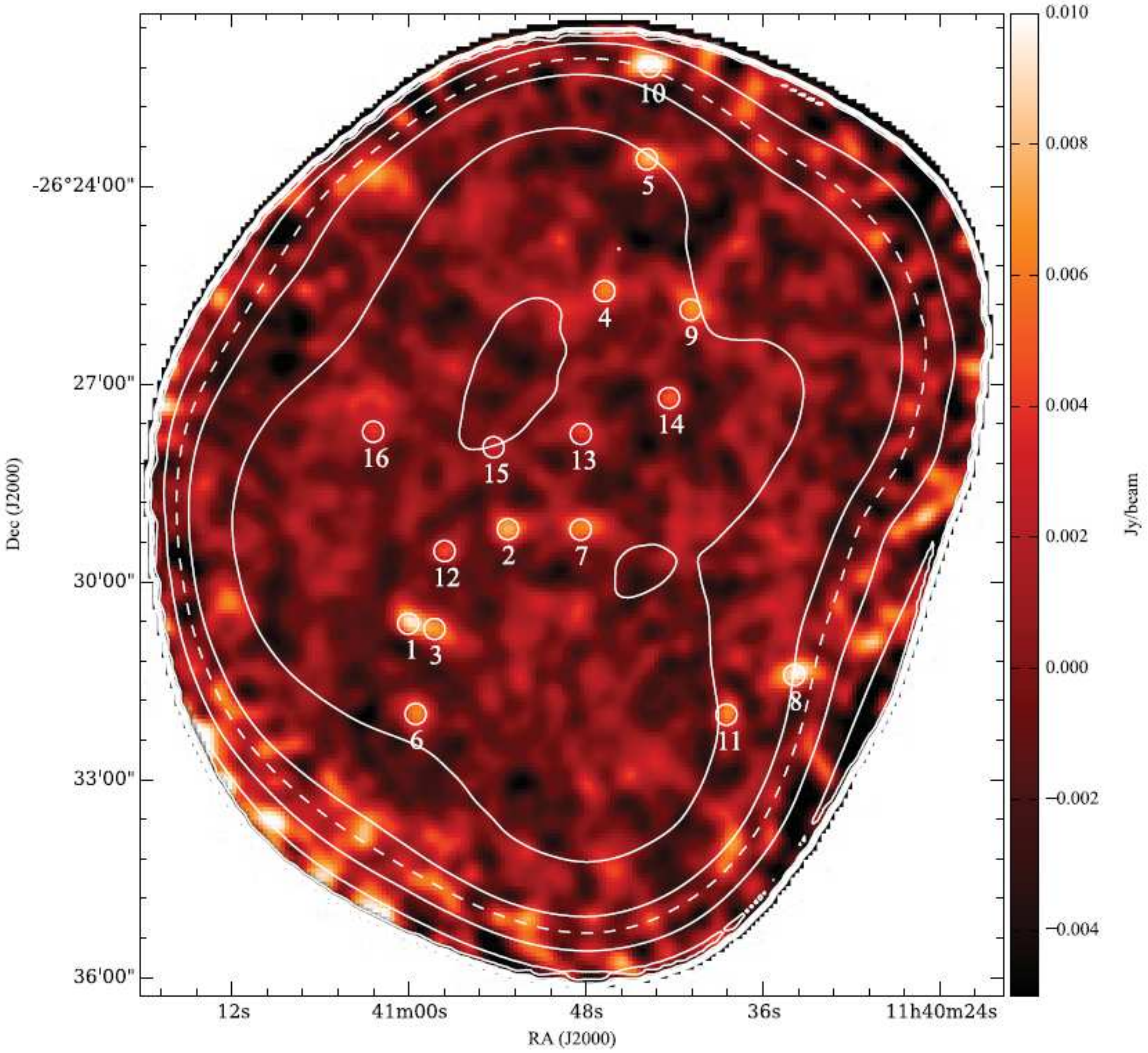
10
5
4
9
14
16
15
13
2
7
12
1
3
8
6
11
-26°24'00"
27'00"
30'00"
33'00"
36'00"
Dec (J2000)
12s
41m00s
48s
36s
11h40m24s
RA (J2000)
0.010
0.008
0.006
0.004
0.002
0.000
−0.002
−0.004
Jy/beam

Figure 1.6: LABOCA flux map of the field around the HzRG (indicated by #7) (Dannerbauer et al. 2014). The white circles indicate the locations of the 16 LABOCA detections reported in the same paper. White contours represent the noise contours of the map, respectively 1.3, 1.9, 2.6, 3.0, 3.7, 5.2 and 7.4 mJy/beam. 14 sources out of 16 are included in the 56 $arcmin^2$ subregion, which constitutes the overdensity region. North is at the top, east is to the left.

As we mentioned before, Dannerbauer et al. (2014) attempted an ambitious counterpart matching, looking for possible counterparts of the LABOCA sources in all the available data of the same region to improve the characterization of the protocluster field (Spitzer MIPS, Herschel PACS and SPIRE, VLA data, and narrow-band observations of LAEs and HAEs). This task also allowed to reconstruct the SED and estimate photometric redshift for the LABOCA detections. These are very useful, since the field is only partially covered by spectroscopic redshift information. Based on VLA 1.4 GHz, Herschel, Spitzer MIPS and Subaru H_α imaging, the authors identified the counterparts of the LABOCA sources and derived FIR photometric redshifts, coupling them with spectroscopic redshift available from H_α spectroscopy (see Table 1.1). Based on such redshifts, we can establish whether or not the LABOCA detections are part of the protocluster structure at z=2.2. Protocluster membership is secure for DKB01, DKB03, DKB07, DKB12 and DKB16 and tentative for DKB02 and DKB05. For three sources, meaning DKB06, DKB13 and DKB14, cluster membership was ruled out. For the remaining sources, not enough information was collected. Figure 1.7 shows the LABOCA detections, where different colors and shapes are assigned basing on whether or not the sources are confirmed protocluster members. The authors also considered again number density focusing on a narrower circular area of 4' diameter, hosting all those sources which had spectroscopic redshift information and were confirmed member. Such area can be seen as a black circle in Fig.1.7. This subregion shows even stronger evidence for an excess of SMGs: the cumulative number count for sources with flux densities $>$7 mJy lead to a value which is about 4 times the reference field (Weiß et al. 2009), meaning 2 times more than the 56$arcmin^2$ area considered earlier. Such compact SMG overdensity should correspond to the core of the protocluster structure, and is not centered exactly on the radio galaxy MRC1138-262, but rather slightly east from it.

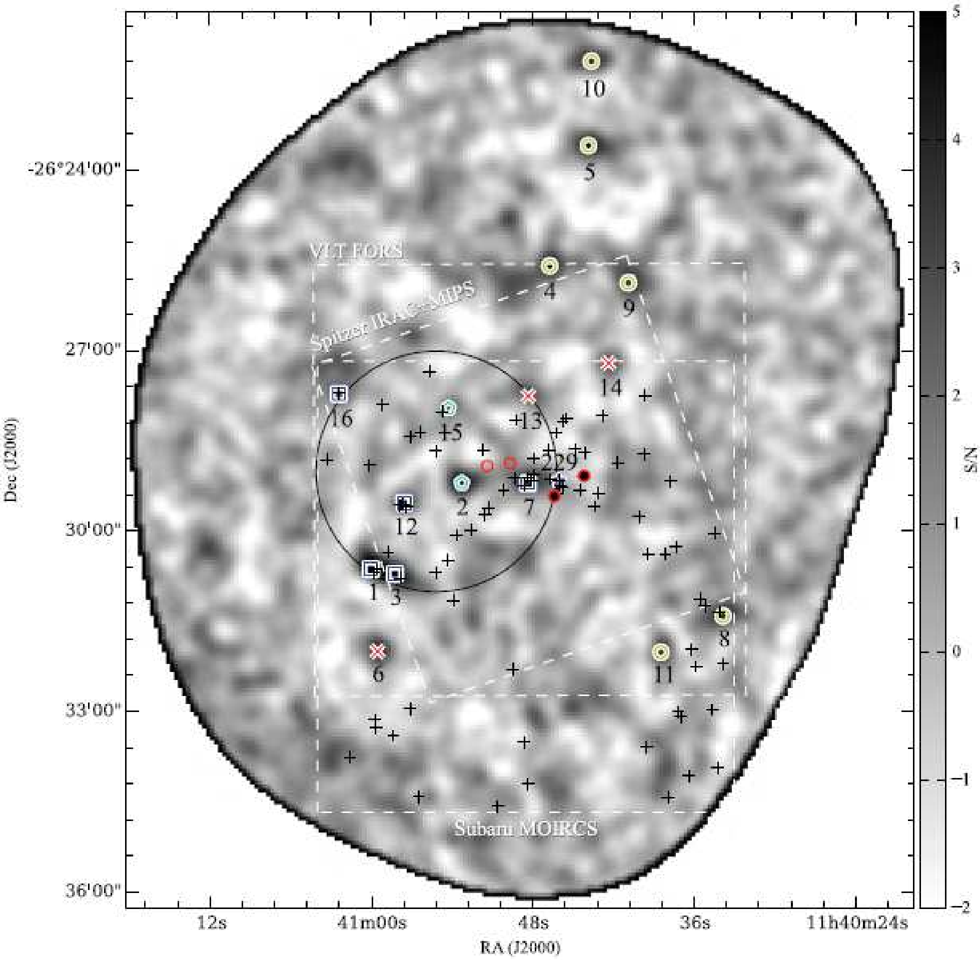

Dec (J2000)
RA (J2000)
-26°24'00"
27'00"
30'00"
33'00"
36'00"
12s
41m00s
48s
36s
11h40m24s
S/N
5
4
3
2
1
0
−1
−2
VLT FORS
Spitzer IRAC+MIPS
Subaru MOIRCS
10
5
4
9
14
16
13
15
2
7
22
29
12
1
3
8
11
6

Figure 1.7: The 16 sources extracted by LABOCA in the Spiderweb field. DKB07 is the high-redshift radio galaxy MRC1138-262. Blue squares represent spectroscopically confirmed members of the protocluster at z=2.2. Cyan pentagons mark the tentative protocluster members, yellow circles mark those sources for which the membership was not determined. Red crosses show sources that are not protocluster members. The white circle marks the area with diameter 4′, where the overdensity is concentrated. Moreover, the dashed squares represent the field of view of Spitzer IRAC/MIPS, VLT/FORS and Subaru/MORCS dataset.

1.6 Motivation

Dannerbauer et al. (2014) proved that sub-mm observations can indeed unveil protoclusters of massive, dusty starburst events, and detailed observation at this wavelength regime is feasible. However, they also emphasize that only the highly sensitive, subarcsecond resolution power of ALMA would lead to a complete characterization of the sources identified by LABOCA. In fact, LABOCA beam size ($\approx$ 19") is too coarse to allow robust and unambiguous source identification: uncertainties on the positions are large and in most cases we are facing detections that correspond to multiple sources blended together. Such sharp, confusion-free observations would bridge the existent gap between the coarse LABOCA FIR data and the high-resolution optical/NIR datasets (HST, Subaru).

For these reasons, new ALMA observations have been carried out. They constitute the core of this thesis and we will present them in detail in the next chapter. ALMA was used with the aim of spatially resolving the emission blobs identified by LABOCA, measure their flux and evaluate the density of the field using the new ALMA catalogue.

The goals of this thesis include:

- check the reliability of the LABOCA sources;
- deblend the LABOCA sources into multiple detections;
- determine subarcsecond positions;
- accurately measure fluxes of the ALMA detections;
- studying number density of galaxies by computing number counts (number of galaxies per unit area), in order to constrain the overdensity of the field;
- set up a multiwavelength analysis to investigate the robustness of the catalogue.

In the following, we are going to describe the datasets and describe the methodology applied to analyse them (Chapter 2). Afterwards, we present the results that we obtained (Chapter 3), and we discuss them in comparison to literature (Chapter 4). We summarize the main points of in the final chapter (Chapter 5).

Chapter 2

Datasets and methodology

2.1 Dataset

This work is based on ALMA observations carried out in the field of the Spiderweb protocluster. ALMA targeted the 16 LABOCA detections reported by Dannerbauer et al. (2014) with the aim to study them with ALMA and see if they split in multiple sources, thanks to its ground-breaking resolution, unprecedented for this field. Later, we also present other high-resolution multiwavelength data available for this field.

2.1.1 ALMA data

2.1.2 Observations

ALMA targeted 13 out of the 16 sources selected by LABOCA. In fact, DKB07, DKB12 and DKB15 are not included in this project, as they were observed in other ALMA programs and subarcsecond accurate positions were already obtained. These sources were not considered in this analysis to ensure an homogeneous treatment of data, as they belong to different observation sessions and were reduced differently. Note that 07 and 12 were confirmed protocluster members (DKB07 is the radio galaxy that names the field), and 15 was classified as "candidate member" (Dannerbauer et al. 2014).

Our ALMA data are 870μm, band 7 snapshot dust continuum observations (project code 2016.1.00102.S, PI Helmut Dannerbauer), carried out with the 12-m array during ALMA Cycle 4, in configuration C40-4. The observed band is split up int two sidebands covering the ranges [335-339] and [347-351] GHz respectively. Data were taken on November the 16th, 2016 between 11:23 and 11:33 UTC. The 13 observed maps are centred on the LABOCA coordinates reported by Dannerbauer et al. (2014) and reported in Table 1.1. The requested flux sensitivity was 0.17 mJy with an angular resolution down to 0.3”. Each of the 13 separate pointings had a FoV of 17” and was observed for an integration time of 32.2 s (snapshot observation). Including overheads, the total time invested in the project reached ≈0.5 hours.

2.1.3 Data reduction

Every single LABOCA detections is observed with an independent ALMA observation, so we deal with 13 different pointings. The ALMA flux maps were reduced by Dr. Bjorn Emonts[1], using the CLEAN algorithm. Images were cleaned using two different weighting schemes: natural weighting and Briggs weighting with robustness parameter R=0.3. Natural-weighted flux maps were also tapered using Gaussian tapering with 4 different threshold values; 50kλ, 100kλ, 250kλ, 500kλ. Tapering and weighting schemes provide different beamsizes and also affect the achieved rms sensitivity. Table 2.1 reports the beamsize of each weighting scheme, ranging from 1.75" for the most stringent tapering (natural weighting and 50kλ tapering) to 0.3" for the Briggs weighting with no tapering.

We point out that ALMA does not have a uniform response function within the FOV. The ALMA pointing must be corrected according to its response function. In fact, the edges of the pointing field lie outside the primary beam, and thus they have different sensitivity and must be corrected with a multiplicative factor before using them for science purposes. We have both the uncorrected data and the primary beam-corrected data, but we use only the latter for scientific discussion. Figure 2.1 show an example of the primary beam corrected ALMA flux maps, the ones for LABOCA source DKB01. Each panel represents one of the six different weighting configurations. On the bottom left of each panel, a blue circle represents the tapered beamsize.

---

[1] National Radio Astronomy Observatory: Charlottesville, VA, US

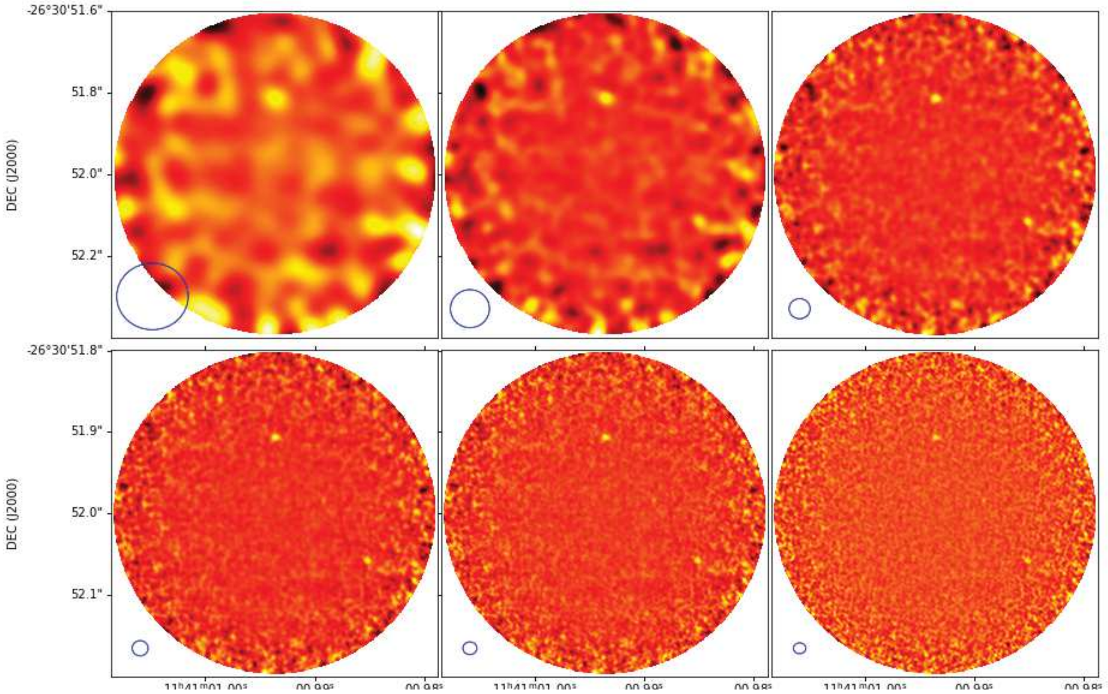

Figure 2.1: ALMA primary beam-corrected flux maps for LABOCA detection DKB01. From top to bottom, left to right: Natural Weighting with Tapering 50kλ, Natural Weighting with Tapering 100kλ, Natural Weighting with Tapering 250kλ, Natural Weighting with Tapering 500kλ, Natural Weighting with No Tapering, Briggs Weighting.

2.2 Source extraction

2.2.1 Noise computation

ALMA fields do not have homogeneous noise, so we cannot just compute the RMS of the full map irrespectively of the distance from the center. In fact, due to primary beam correction, noise is enhanced at the edge of the map. The method designed in this analysis ensures we are tracking noise in the surroundings of the source, thus accounting for the specific behaviour of noise in that part of the field. The approach is the following: for each pixel in the map, we fix an inner and outer radius, defining two partially overlapping circular regions centred in such pixel. Noise is computed as the root mean square (RMS) of the ring region between outer and inner radius, after proper sigma clipping. This allows to assign a noise value to each pixel of the map. In this way, we probe the every region of the ALMA field, while simultaneously trimming out potential sources located in the reference pixel, so that the noise estimate is not contaminated. The most robust choice is 2-sigma clipping and ≈ 2 arcsec ring width: such settings guarantee that the noise estimate is independent on the width of the ring. In fact, we find that with 3σ clipping the noise estimate depends too strongly on the thickness of the ring (2,2.5 or 3 arcsec), changing more than 20%.

Fig 2.2 displays an example for the noise contours, associated to the pointing of DKB01. First, we note that noise for strongly tapered images is higher: noise ranges from about 0.6 to ≈2 mJy/beam in 50kλ-tapered images (top left), while in the absence of tapering (bottom middle and bottom right) noise ranges from 0.2 to 0.6 mJy/beam on the edges.

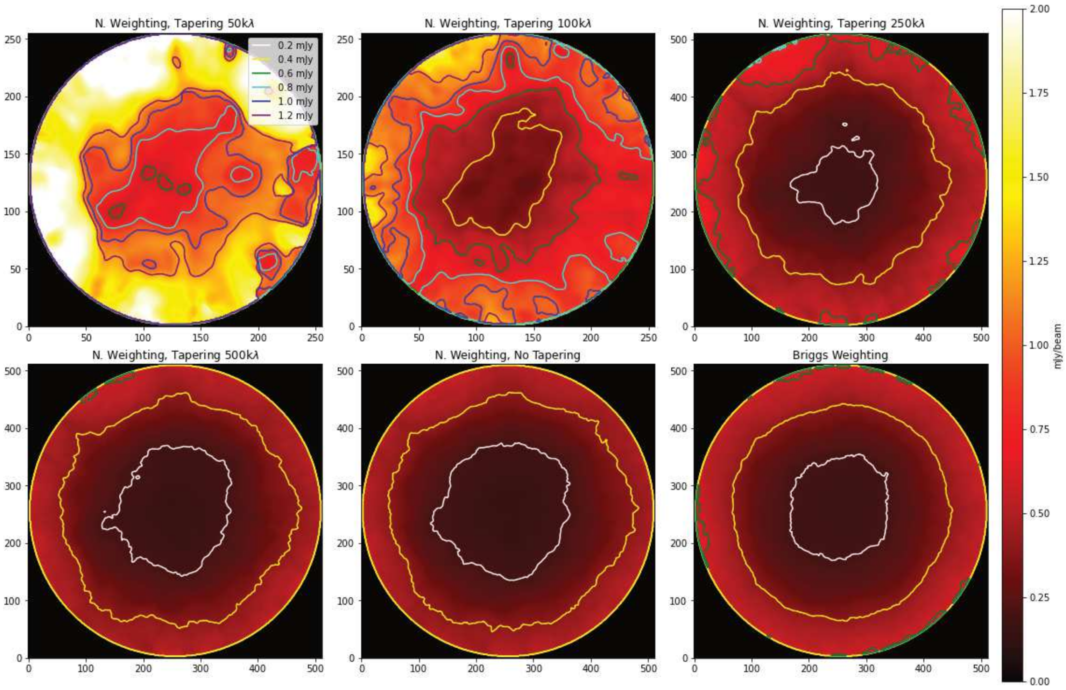

Figure 2.2: Noise contours for DKB01 field for different reduction schemes. The noise panels are displayed in units pixels: the scale is 0.1"/pixel for the heaviest taperings (50 and 100 kλ) and 0.05"/pixel for the rest of the cleanings. RMS is lower as we go to higher-resolution, lighter-tapered images. With stringent 50kλ tapering, noise ranges from 0.6 to 2 mJy/beam. With light tapering or raw images, noise ranges roughly from 0.2 to 0.6 mJy/beam.

Second, we point out that noise also has an increasing profile within the single pointing. If we look at a single panel, we see that noise is higher at the edges, while the central area is characterized by lower noise and by a more uniform pattern. This area corresponds to the primary beam. A focus on the trend of noise as a function of the distance from the center is given by Fig 2.3, which represents the noise profile for the DKBO1 ALMA pointing with 100kλ tapering. The steepness of the noise growth seems not to be constant, but suddenly increasing at around 10". This roughly defines ALMA primary beam, which is the region where noise can be approximated as constant at first order. Indeed, the noise profile is flatter within that distance from the center.

A quantitative indication of the noise in the different taperings can be found in Tab.2.1. In the table we report an average estimate of the noise within the primary beam of the available ALMA maps. PB noise goes from $\gtrsim$0.8 mJy in heavily tapered images, that suffer from resolution deterioration, down to $<\approx$0.2 mJy noise of lightly-tapered or not tapered flux images.

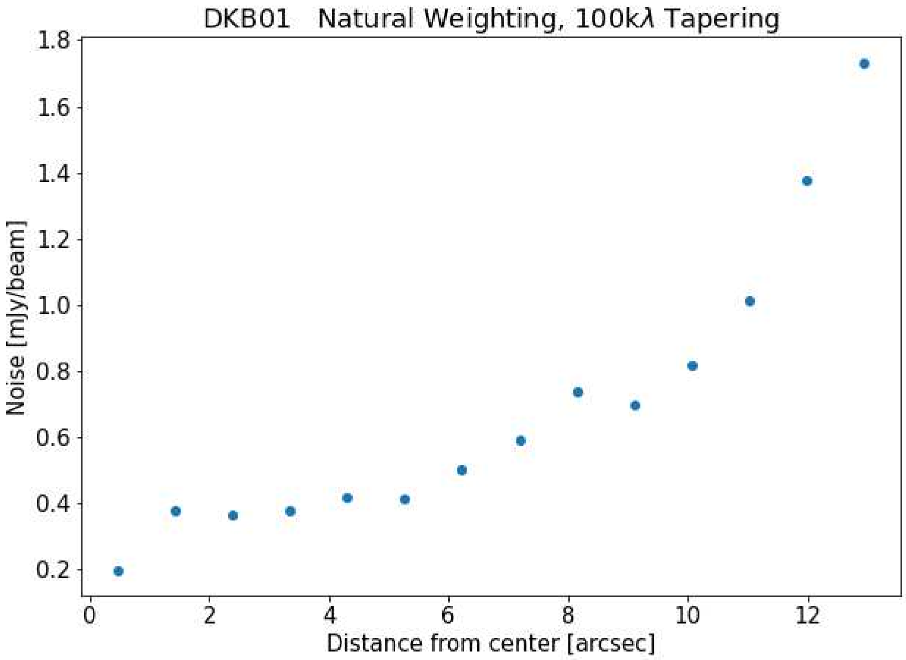

Figure 2.3: Trend of noise as a function of distance from the center of the ALMA field for DKB01, Natural Weighting, Tapering 100kλ.

weighting scheme	tapering	beamsize [arcsec]	PB-rms [mJy/beam]
natural	$50k\lambda$	1.75	0.7
	$100k\lambda$	0.96	0.4
	$250k\lambda$	0.52	0.2
	$500k\lambda$	0.39	0.2
	no tapering	0.34	0.2
Briggs	no tapering	0.30	0.2

Table 2.1: ALMA beamsizes and estimated rms according to weighting scheme and tapering. Strongest tapering leads to larger beamsize and higher noise estimates. The noise profile changes from map to map, in the table we report an average noise within the primary beam of the maps.

2.2.2 Source detection

The search for sources was initially done with a visual inspection, and later verified with a source-finder Python script, developed and tested by myself. This tool first produces a pixel-by-pixel S/N map, that can be inspected to select the candidate location of a source.

In the script, flux measurements are carried out in two ways: peak flux (typical for radio astronomy) and integrated flux. The former is the traditional way to quantify flux in radio astronomy, where sources are most of the times unresolved. However, with such high ALMA resolution, the approximation of point-like, unresolved source may not work in all cases. This is why we also introduce integrated flux measurements, where we integrate the flux within fixed apertures. This method is supposed to better recover the intrinsic flux of resolved emission.

Flux is measured in units mJy/beam. Note that beamsize has an impact in determining integrated flux. The fixed aperture are chosen indicatively so that the flux of sources are maximized: if the aperture is too wide the relative contribution from the noise increases, if it is too narrow we miss extended emission (Béthermin et al. 2020).

Basing on the candidate locations of sources, this Python tool performs the following tasks:

- identify the brightest pixel of the emission spot (for the peak flux estimate);
- computes peak flux and integrated flux within fixed aperture, summing those pixels having flux >2xRMS. A different fixed aperture is chosen for each reduction setting:
  - $r = 1.4$" for natural weighting + tapering 50 kλ;
  - $r = 1$" for natural weighting + tapering 100kλ;
  - $r = 0.6$" for natural weighting + tapering 250kλ and 500kλ;
  - $r = 0.5$" for natural and Briggs weighting + no tapering;
- compute noise;
- quantify S/N for both peak flux and integrated flux;
- compute emission area, or the sum of the pixels inside the aperture which have at least >2RMS. Figure 2.4 shows an example of an ALMA source detected within the pointing of DKB01;

Figure 2.4, produced by the script, shows a heatmap indicating the emission area of the source DKB01-1, taken as an example, in the various cleanings. The emission area varies strongly as a function of beamsize: at 50kλ, the source is unresolved and can be considered point-like. Therefore, at such low-resolution we only see the PSF and the emission area is comparable with the beamsize. As we go to higher resolutions (lighter taperings), the beamsize becomes comparable with the size of the source and allows to explore its physical emission. In other words, the source becomes resolved.

Once we have the flux and noise measurement per each pixel and per each weighting configuration, we need to qualify sources. To confirm the presence of an ALMA source, the detections have to meet one common S/N criterion: they have to reach a 5σ detection in at least 3 out of the 6 different data configurations available. This criterion is chosen to make sure that the sources are significant: we want to rule out emission spots that have enough significance in a given resolution but are not properly detected at other resolutions. The choice of the 5σ criterion is suggested by the pixel S/N distribution of the flux

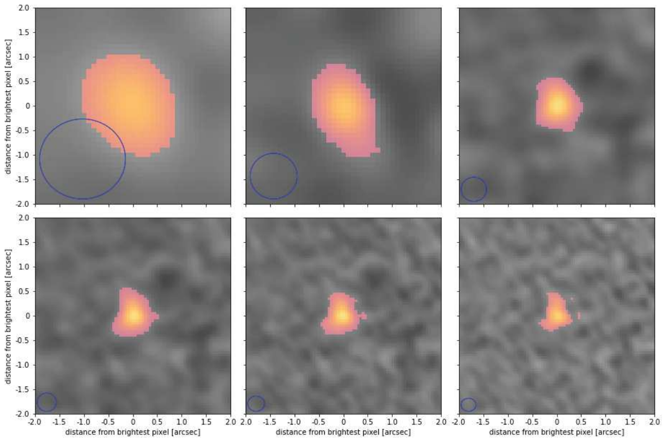
distance from brightest pixel [arcsec]
2.0
1.5
1.0
0.5
0
-0.5
-1.0
-1.5
-2.0
distance from brightest pixel [arcsec]

Figure 2.4: ALMA source DKB01-1, detail of detection shown in all different reduction schemes, as detected by the script. Top to bottom, left to right: Natural Weighting with 50, 100, 250, 500kλ tapering, Natural Weighting with no tapering, Briggs Weighting with no tapering. The beam for each tapering scheme is represented by a blue circle in the bottom left corner of the panel. Each panel is a 4”x4” square and each , centred on the peak of the emission. The axes are in pixels unit, meaning 0.1”/pixel for the 50 and 100kλ tapering and 0.05”/pixel for the other taperings. Coloured pixels correspond to the pixels associated to flux $> 2\sigma$ and make up the emission area of the source: the lighter the color, the brighter the pixel.

map (Figure 2.5). The bulk of the histogram is reasonably well-fitted by a Gaussian profile well centered around zero, as one would expect for pure noise; however, there is evidence of skewness associated to an excess of pixels with S/N>5. These pixels may represent real submm sources.

When setting the S/N cut we should account for completeness. A correction would need to be applied because weak sources are less likely to be recovered by source detection algorithms due to many different factors (instrumental noise or spurious emission mainly). However these correction operations are postponed to further stages of this project.

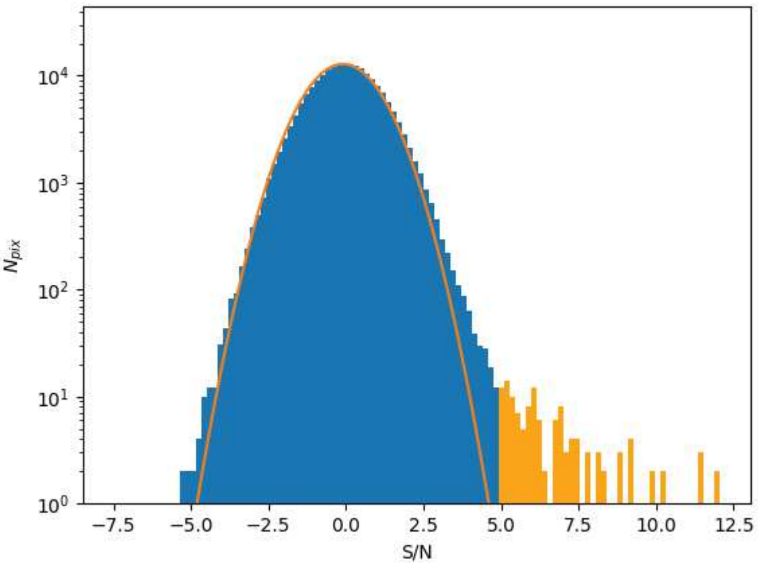

Figure 2.5: Pixel S/N distribution for DKB01, taken as an example, with natural weighting, no tapering. A Gaussian bell (solid line) fits well the histogram,, except for the signal excess, represented by the yellow bins.

2.3 Number counts

Quantifying the number density of SMGs within the Spiderweb field is part of the backbone of this project, since we aim to better constrain the overdensity estimated in Dannerbauer et al. (2014). Number counts are a key requirement to probe the protocluster nature of the field. In protocluster fields, number counts amount to several times the reference density extracted by blank field surveys found in literature.

The first step to compute number counts is to set up histograms with properly binned flux density. We computed two kinds of number counts: differential number counts are obtained by dividing the raw counts by the mean value of the bin and by the total observed area in this ALMA observation (counts per unit flux and area). Differential number counts represent the surface density of sources per observed flux density interval (dN/dS) of a cosmological population and they are a simple measure of source abundance and a powerful tool for model comparisons. In differential number counts, each source is associated to weight of $1/(A_e\mathrm{dS})$, where A_e is the effective detection area and dS is the flux density median of the binned distribution.

On the other hand, the so-called cumulative number counts are expressed in terms of counts per unit surface above a certain flux.

In order to test the flux calibration and consistency with previous number counts, in this work we work out both the differential and cumulative number counts at 870 μm. The aim is to evaluate the number density of the Spiderweb protocluster and possibly get more insights on the conclusions drawn by

Dannerbauer et al. (2014).

In the analysis that we carry out, we are going to compare our counts to the ones taken from literature, as well as the models used by other authors. As well as differential number counts are concerned, the most widespread fitting laws in literature include a Schechter function or a simpler broken powerlaw.

$$\text{Schechter form} \qquad \frac{dN}{dS} = \frac{N_0}{S_0}\left(\frac{S}{S_0}\right)^{-\gamma} e^{-\frac{S}{S_0}} \tag{2.1}$$

$$\text{Broken powerlaw} \qquad \frac{dN}{dS} = \begin{cases} N_0(S/S_c)^{\alpha} & \text{if} \quad S < S_0 \\ N_0(S/S_c)^{\beta} & \text{if} \quad S > S_0 \end{cases} \tag{2.2}$$

N indicates the counts per unit area, while S corresponds to the flux density. N_0 $[deg^{-2}]$ and S_0 $[mJy]$ are parameters that are estimated by the fit and depend on the dataset. γ represents the characteristic index of the Schechter function, while α and β are the two slopes of the broken powerlaw, in the two regimes splitted by the cut flux S_c. In most astrophysical samples, $1 < \gamma < 2$.

Cumulative number counts can be fitted with a the definite integral of the Schechter function, which gives rise to a lower incomplete Gamma function.

$$N(> S) \propto \int_{S_1}^{S_2} \left(\frac{S}{S_0}\right)^{-\gamma} e^{-\frac{S}{S_0}} \propto P(1-\gamma, S_2) - P(1-\gamma, S_1) \tag{2.3}$$

where P(s, α) isis the incomplete Gamma Function.

$$P(s, \alpha) = \frac{1}{\Gamma(s, \alpha)} \int_0^{\alpha} t^{s-1} e^{-t} dt \tag{2.4}$$

$\Gamma(s, \alpha)$ is the Gamma function. Alternatively, some authors use again a powerlaw.

This dataset lacks completeness correction: this will make our counts smaller than expected at the faint end of number counts distribution. Usually, one can define an effective area as the region of the map in which the noise pattern allow detection of a source at our S/N threshold. Effective area is computed as a function of flux $A_e(S)$ and has a monotonic trend as a function of flux. This means that at low fluxes the effective area is just a fraction of the total observed field. For sources >5mJy the effective area is basically equal to the observed area, thus the sample generally does not need a completeness correction.

Number counts also usually need other corrections due to known observational biases. For instance, flux densities are "boosted" due to two different factors. One of them is statistical (Eddington boosting), and applies to any counts of rare/common objects. Being the common object more abundant, the risk of mistaking a common object for a rare one is higher. Moreover, if common objects are mistaken as rare, then the error on the counting of the rare objects will be very high in fraction. For astronomical objects, it is common to assume that more sources are intrinsically faint than bright. Therefore, more faint source are randomly mistaken as brighter, so the bright counts are normally up-scattered. The second contribution to boosting is connected to confusion noise, as sources lying below the detection limit may be transferring flux to brighter objects. Another issue is represented by spurious sources: part of the sources may be fake, thus number counts overestimated. Finally, we also mention sample contamination: if a detection threshold is too severe, we have high completeness and low contamination, but reduce the size of the sample, thus its statistical significance. Montecarlo simulations can in principle correct for such issues, but we postpone such task to a future development of this work.

An exhaustive treatment of differential number counts, including all the bias effects, would thus be

$$\frac{dN}{dS} = \frac{1}{\Delta S} \sum_i \frac{1 - f_i}{A_e(S_i)} \tag{2.5}$$

where f_i is the spurios sources rate on the i-th bin, and $A_e(S_i)$ is the effective area at i-th flux bin.

Our references include interferometric number counts as well as number counts coming from single-dish surveys as a secondary reference.

2.4 Multi-wavelength data

A simple way to test the robustness of a source and infer its physical properties is counterpart matching: if images from the same field are available in other wavelengths, then we can look for emission in such maps at the location of the ALMA-detected source.

Flux densities depend on SED properties and the physical properties of DSFGs depend on the counterpart identification of the object. As already mentioned in the Introduction, long-wavelength measurements enjoy the property of negative K-correction, making submm observations in this band very convenient and allowing source detection up to high redshift. However, trying to study the same sources in other bands, redshift may have an impact and lead to misidentifications that can bias the physical characterization of the system under exam. Yet, a complete analysis of a population of candidate DSFGs needs a multiwavelength study.

Normally follow-ups are the most efficient way to narrow down the accuracy on the position of a source: if we cannot achieve higher resolution data for our target wavelength, an option can be finding a robust counterpart in a band with better resolution so we can constrain the coordinates of the source. That highlights the importance of a solid multiwavelength analysis. However, even with the high resolution of our ALMA data, an accurate counterpart matching will lead to a better characterization of the source in question.

We use exquisite multiwavelength photometry and catalogues, centred close to the HzRG MRC1138-262. Most of them do not cover all ALMA-observed sources due to a lack of coverage. We perform a simple counterpart matching using the instrument beamsize as matching radius.

2.4.1 MW data

A number of datasets covering the Spiderweb protocluster field at least partly is available.

$Ly\alpha$ imaging $Ly\alpha$ line (rest-frame wavelength at $1215.7A°$) is a renown tracer of star-formation, coming from neutral hydrogen of distant galaxies. Kurk et al. (2004a) reports VLT/FORS1 narrow-band imaging targeted at the $Ly\alpha$ line associated to ten different radio galaxies between redshift 2 and 5. Observations of a section of the LABOCA field (49 $arcmin^2$) provided a catalogue of 15 confirmed LAEs ($Ly\alpha$ emitters).

Optical/NIR imaging Exquisite, high-resolution datasets are available in the optical , where we have HST/ACS/WFC very deep 814 nm observations (5 different fields, mosaicked into a single map, each with an exposure time ≈38 min), taken on May 17th-22nd, 2005 (ID 10327, HST Cycle 13, PI: Holland Ford). We also include Spitzer IRAC ch1 dithered 30s observations ($3.6\mu m$, Seymour et al. 2007, Fazio et al. 2004).

From Dannerbauer et al. (2017) we use a sample of VLT/HAWK-I broad-band data in the Y, H and K_s band, in the NIR. Observations were taken in February, March 2012, April, May and July 2013 and January-February 2015 in service mode, with an average seeing $0.4" - 0.6"$. Dithered HAWK-I data were reduced using the ESO/MVM data reduction pipeline, using the standard reduction steps for NIR imaging data.

NIR imaging is also complemented by Subaru/MOIRCS and HST/NICMOS observations. MOIRCS covered a 50 $arcmin^2$ area with the narrow band NB2071 ($\lambda = 2.068\mu$m). Observations are reported and widely discussed in Koyama et al. (2013), ranging from redshift 2.13 to 2.17. HAEs (H_α emission) detection catalogues is also provided by Koyama et al. (2013), covering the $H\alpha 6563$ line at redshift z≈2.17. H_α emission is notoriously associated to star-forming activity, making it a good protocluster tracer. Shimakawa et al. (2018) also reports HAE catalogue from a deep H_α survey, based on narrow band imaging of the Spiderweb protocluster, again with Subaru/MOIRCS/NB2071.

For z≈2 galaxies, HST/NICMOS camera provide rest-frame optical, high-resolution images in two broad bands (110 and 160μm), discussed in detail in Zirm et al. (2008). These observations reach an AB limiting magnitude of m=24.9 at 110 and m = 25.1 at 160 μm.

Spitzer MIPS imaging MIR is investigated through archival Spitzer MIPS observations (24 μm, PI: Spencer Standford, Program ID: 20593), with 5'x5' field centred on the HzRG and cover a fraction of the LABOCA image (about 20%).

Herschel data FIR data is provided by the Herschel Space Observatory (Pilbratt et al. 2010, Poglitsch et al. 2010, Griffin et al. 2010). MRC 1138-262 field was observed as part of the project scientist guaranteed time (PI:

Telescope	**Instrument**	**Band**	**Spatial Resolution**
Hubble Space Telescope	ACS	814 nm	0.1"
	NICMOS	1.1μm	
		1.6μm	
Subaru	HSC	z ($\approx$ 900 nm)	0.6"
	MOIRCS	NB2071 (2.1μm)	0.5"
		K_s (2.1μm)	
Very Large Telescope	HAWK-I	Y	0.25"
		H	
		K_s	
	ISAAC	K_s	0.65"
Spitzer Space Telescope	IRAC	ch1 (3.6 μm)	2"
	MIPS	24μm	6.7"
Herschel Space Telescope	PACS	100 μm	7.2"
		160μm	11"
	SPIRE	250μm	18"
		350 μm	25"
		500μm	36"
Very Large Array		1.4 GHz	2"

Table 2.2: Available multi-wavelength database. Column (1) telescope site, (2) instrument employed for the observations, (3) investigated wavelength, (4) indicative beam size of the instrument in that band.

Altieri). Data are available in two Herschel PACS bands (100 and 160 μm) and three Herschel SPIRE bands (250, 350, 500 μm), with a catalogue of Herschel archival detections relative to this field. PACS images have 3σ sensitivities of 4.5 and 9.0 mJy at 100 and 160 μm respectively. SPIRE also achieves 3σ sensitivity of 7.5, 8.0, 9.0 mJy in the three bands. The flux maps cover 120 $arcmin^2$ and 900 $arcmin^2$ for PACS and SPIRE, so the latter covers the LABOCA map fully, while the former almost completely. Herschel catalogue was used for the counterpart matching.

VLA imaging Radio coverage at VLA (Napier, Thompson & Ekers 1983) 1.4 GHz (20 cm) is provided by April 1-12, 2002 observations in A configuration for a cumulative exposure time of 12h (ID AD0463, PI De Breuck). Data were observed in pseudo-continuum, spectral line mode with 7x3.125 MHz channels. The final 7.5'x7.5' image is characterized by a rms noise level of 19 μJy/beam and a beam of 2.7"x1.3". With a dynamic range of 10^4, this VLA observation is relatively shallow in comparison to other deep VLA follow-ups of submm fields.

Chapter 3

Results

In this chapter we present the measurements carried out on the ALMA 870 μm images. We present and discuss the two different flux estimates, peak flux and integrated flux, and compare them with the original LABOCA flux. Moreover, we present the results of the counterpart visual inspection.

3.1 Source catalogue

We applied our tool for source detection using the 5σ-significance detection criterion as explained in Section. 2.2.2, identifying 34 sources. Other 7 sources are added to the catalogue even though they achieve a lower S/N, between 3 and 5σ, but present evidence for counterparts at other wavelengths. They are thus included in our catalogue, that is composed of 41 sources.

Table 3.1 reports the complete catalogue of the ALMA sources extracted in this analysis. The first 5 characters of their ID identify the corresponding LABOCA source, while the last digit identifies the recorded detection in the ALMA field centered in the LABOCA source. The table also reports the coordinates (RA and DEC in J2000 format), peak flux measurement associated to the brightest pixel, noise estimate, aperture flux integrated within fixed aperture and S/N for both the flux estimates. All these values are shown for the different cleaning and tapering schemes.

ALMA-ID	Q	WS	RA hh:mm:ss	DEC dd:mm:ss	S_p [mJy/b]	N [mJy/b]	S/N_p	S_i [mJy/b]	S/N_i
DKB01-1	1	50	11:40:59.600	-26:30:39.20	3.83	0.59	6.51	2.24	3.82
		100	11:40:59.600	-26:30:39.10	3.79	0.33	11.42	3.48	10.48
		250	11:40:59.600	-26:30:39.15	3.12	0.2	15.93	3.78	19.32
		500	11:40:59.600	-26:30:39.15	2.69	0.17	15.67	4.04	23.48
		0	11:40:59.597	-26:30:39.15	2.47	0.17	14.98	4.07	24.68
		R03	11:40:59.600	-26:30:39.15	2.26	0.19	12.06	3.54	18.89
DKB01-2	1	50	11:41:0.003	-26:30:35.40	1.88	0.61	3.07	1.52	2.5
		100	11:40:59.966	-26:30:35.40	0.99	0.32	3.11	0.73	2.31
		250	11:40:59.966	-26:30:35.35	0.91	0.19	4.66	0.6	3.07
		500	11:40:59.966	-26:30:35.35	0.92	0.15	5.93	0.71	4.63
		0	11:40:59.966	-26:30:35.35	0.92	0.14	6.53	0.82	5.84
		R03	11:40:59.969	-26:30:35.35	1.04	0.15	6.83	0.82	5.39
DKB01-3	1	50	11:41:0.345	-26:30:31.30	3.77	1.21	3.12	1.86	1.54
		100	11:41:0.323	-26:30:31.80	3.03	0.44	6.84	2.53	5.70
		250	11:41:0.319	-26:30:31.90	2.68	0.27	10.06	2.87	10.78
		500	11:41:0.319	-26:30:31.90	2.39	0.23	10.52	3.07	13.51
		0	11:41:0.319	-26:30:31.90	2.21	0.22	9.91	3.05	13.67
		R03	11:41:0.323	-26:30:31.90	1.82	0.25	7.15	2.6	10.20

DKB01-4	2	50	11:40:59.749	-26:30:32.50	0.99	0.67	1.48	0.	0.
		100	11:40:59.772	-26:30:31.60	1.50	0.47	3.18	0.57	1.21
		250	11:40:59.772	-26:30:31.45	1.39	0.28	5.01	1.23	4.42
		500	11:40:59.776	-26:30:31.45	1.10	0.24	4.58	1.41	5.88
		0	11:40:59.779	-26:30:31.50	0.95	0.23	4.14	1.63	7.07
		R03	11:40:59.776	-26:30:31.55	0.86	0.26	3.37	1.18	4.64
DKB01-5	2	50	11:40:59.369	-26:30:43.60	2.24	1.22	1.83	0.	0.
		100	11:40:59.384	-26:30:43.50	1.99	0.55	3.64	1.11	2.03
		250	11:40:59.384	-26:30:43.50	1.95	0.35	5.53	1.47	4.16
		500	11:40:59.384	-26:30:43.50	1.73	0.30	5.79	1.72	5.74
		0	11:40:59.384	-26:30:43.50	1.56	0.29	5.40	1.85	6.35
		R03	11:40:59.366	-26:30:43.45	1.42	0.33	4.34	1.56	4.78
DKB02-1	1	50	11:40:53.206	-26:29:11.00	4.62	0.55	8.33	4.16	7.5
		100	11:40:53.213	-26:29:11.00	3.68	0.3	12.41	3.8	12.81
		250	11:40:53.213	-26:29:11.05	3.06	0.16	19.54	3.62	23.1
		500	11:40:53.213	-26:29:11.05	2.77	0.13	21.03	3.66	27.78
		0	11:40:53.217	-26:29:11.10	2.62	0.13	20.11	3.67	28.23
		R03	11:40:53.217	-26:29:11.10	2.38	0.15	15.74	3.42	22.65
DKB02-2	1	50	11:40:53.712	-26:29:11.80	1.34	0.81	1.66	0.	0.
		100	11:40:53.697	-26:29:11.80	1.65	0.37	4.42	1.03	2.76
		250	11:40:53.697	-26:29:11.75	1.54	0.21	7.43	1.51	7.25
		500	11:40:53.697	-26:29:11.80	1.41	0.17	8.1	1.76	10.14
		0	11:40:53.697	-26:29:11.80	1.29	0.17	7.69	1.75	10.43
		R03	11:40:53.697	-26:29:11.80	1.39	0.19	7.49	1.63	8.79
DKB02-3	1	50	11:40:53.787	-26:29:15.50	1.16	0.92	1.25	0.	0.
		100	11:40:53.779	-26:29:15.10	0.84	0.45	1.88	0.	0.
		250	11:40:53.794	-26:29:14.20	0.90	0.21	4.27	0.34	1.61
		500	11:40:53.794	-26:29:14.15	1.03	0.19	5.44	0.50	2.66
		0	11:40:53.794	-26:29:14.15	1.11	0.18	6.12	0.61	3.35
		R03	11:40:53.790	-26:29:14.15	1.25	0.21	6.03	1.04	5.02
DKB02-4	3	50	11:40:53.273	-26:29:11.30	2.31	0.70	3.31	0.18	0.26
		100	11:40:53.414	-26:29:11.20	0.53	0.28	1.87	0.	0.
		250	11:40:53.369	-26:29:11.90	0.46	0.17	2.77	0.14	0.82
		500	11:40:53.366	-26:29:11.90	0.45	0.14	3.3	0.23	1.71
		0	11:40:53.366	-26:29:11.90	0.43	0.13	3.35	0.25	1.91
		R03	11:40:53.366	-26:29:11.90	0.62	0.15	4.13	0.49	3.29
DKB02-5	3	50	11:40:52.818	-26:29:17.30	2.46	0.68	3.61	0.21	0.30
		100	11:40:52.878	-26:29:15.10	0.65	0.36	1.82	0.	0.
		250	11:40:52.859	-26:29:16.00	0.49	0.21	2.30	0.04	0.21
		500	11:40:52.859	-26:29:16.05	0.63	0.18	3.54	0.20	1.12
		0	11:40:52.859	-26:29:16.05	0.71	0.17	4.24	0.30	1.75
		R03	11:40:52.859	-26:29:16.10	0.95	0.19	5.05	0.61	3.23
DKB02-6	2	50	11:40:53.101	-26:29:17.40	0.43	0.55	0.77	0.	0.
		100	11:40:53.109	-26:29:17.30	0.96	0.35	2.72	0.25	0.70
		250	11:40:53.112	-26:29:17.35	0.79	0.16	4.90	0.76	4.71
		500	11:40:53.120	-26:29:17.40	0.69	0.14	5.04	0.89	6.51
		0	11:40:53.120	-26:29:17.45	0.66	0.13	5.10	0.85	6.53
		R03	11:40:53.120	-26:29:17.45	0.62	0.16	3.98	0.80	5.12
DKB02-7	2	50	11:40:53.779	-26:29:18.90	3.33	0.91	3.65	3.02	3.31
		100	11:40:53.801	-26:29:18.90	2.10	0.49	4.29	1.87	3.82
		250	11:40:53.820	-26:29:18.75	1.30	0.28	4.68	1.32	4.74
		500	11:40:53.820	-26:29:18.75	1.28	0.23	5.54	1.24	5.35
		0	11:40:53.820	-26:29:18.75	1.33	0.23	5.78	1.12	4.87
		R03	11:40:53.820	-26:29:18.75	1.20	0.27	4.86	1.08	4.08
DKB03-1	3	50	11:40:57.746	-26:30:47.80	2.54	0.67	3.77	1.43	2.13
		100	11:40:57.731	-26:30:47.40	1.24	0.38	3.25	1.45	3.80
		250	11:40:57.738	-26:30:47.15	0.76	0.24	3.20	0.73	3.07
		500	11:40:57.746	-26:30:47.10	0.68	0.20	3.43	0.73	3.70
		0	11:40:57.750	-26:30:47.10	0.68	0.19	3.59	0.62	3.32
		R03	11:40:57.716	-26:30:47.30	0.79	0.21	3.74	0.29	1.39
DKB03-2	3	50	11:40:58.394	-26:30:43.60	0.19	0.59	0.31	0.	0.
		100	11:40:58.379	-26:30:43.30	0.64	0.28	2.26	0.08	0.30
		250	11:40:58.379	-26:30:43.05	0.48	0.15	3.24	0.30	2.05
		500	11:40:58.379	-26:30:43.05	0.46	0.12	3.71	0.29	2.35
		0	11:40:58.379	-26:30:43.05	0.46	0.12	3.92	0.25	2.14
		R03	11:40:58.379	-26:30:43.10	0.47	0.14	3.39	0.23	1.70
DKB03-3	2	50	11:40:58.312	-26:30:34.10	2.88	1.53	1.88	0.	0.
		100	11:40:58.297	-26:30:34.50	2.23	0.45	4.92	1.97	4.35
		250	11:40:58.282	-26:30:34.50	1.41	0.31	4.56	1.85	5.95
		500	11:40:58.286	-26:30:34.45	1.12	0.26	4.26	2.0	7.61
		0	11:40:58.286	-26:30:34.45	1.08	0.26	4.17	1.60	6.19
		R03	11:40:58.286	-26:30:34.45	0.88	0.29	3.0	0.43	1.47
DKB03-4	2	50	11:40:58.171	-26:30:40.60	1.45	0.40	3.65	1.08	2.73
		100	11:40:58.193	-26:30:40.50	0.90	0.31	2.88	0.42	1.34
		250	11:40:58.189	-26:30:40.50	0.78	0.15	5.12	0.64	4.18
		500	11:40:58.189	-26:30:40.55	0.76	0.13	5.76	0.66	4.98
		0	11:40:58.193	-26:30:40.55	0.77	0.13	6.05	0.67	5.21
		R03	11:40:58.193	-26:30:40.55	0.69	0.15	4.65	0.44	2.98
DKB04-1	1	50	11:40:46.504	-26:25:39.60	2.11	0.73	2.90	0.61	0.84
		100	11:40:46.504	-26:25:39.60	2.46	0.31	7.84	1.58	5.04
		250	11:40:46.504	-26:25:39.65	2.43	0.14	16.97	2.43	16.93
		500	11:40:46.504	-26:25:39.70	2.29	0.13	17.71	2.65	20.46
		0	11:40:46.504	-26:25:39.70	2.17	0.13	16.96	2.68	20.94
		R03	11:40:46.504	-26:25:39.70	2.08	0.15	13.90	2.65	17.71

DKB04-2	1	50	11:40:46.914	-26:25:35.80	4.73	0.82	5.75	2.96	3.60
		100	11:40:46.921	-26:25:35.70	4.19	0.37	11.41	4.07	11.10
		250	11:40:46.918	-26:25:35.70	3.30	0.19	17.25	4.23	22.10
		500	11:40:46.921	-26:25:35.70	3.07	0.15	20.94	4.32	29.51
		0	11:40:46.921	-26:25:35.70	2.97	0.14	21.60	4.12	30.00
		R03	11:40:46.921	-26:25:35.70	2.90	0.15	19.07	3.20	21.07
DKB05-1	1	50	11:40:43.560	-26:23:37.70	7.53	0.68	11.02	7.08	10.36
		100	11:40:43.560	-26:23:37.70	6.34	0.37	16.97	6.50	17.40
		250	11:40:43.556	-26:23:37.70	5.05	0.20	25.51	6.35	32.06
		500	11:40:43.556	-26:23:37.75	4.24	0.16	26.70	6.83	43.01
		0	11:40:43.553	-26:23:37.75	3.78	0.15	24.78	6.73	44.14
		R03	11:40:43.553	-26:23:37.75	3.15	0.17	18.85	5.80	34.67
DKB05-2	1	50	11:40:44.483	-26:23:46.80	3.50	1.44	2.42	0.82	0.57
		100	11:40:44.498	-26:23:47.10	3.81	0.74	5.14	2.30	3.10
		250	11:40:44.505	-26:23:47.00	3.41	0.38	8.88	3.71	9.66
		500	11:40:44.505	-26:23:47.00	3.03	0.31	9.72	4.27	13.69
		0	11:40:44.505	-26:23:47.00	2.88	0.31	9.27	4.16	13.39
		R03	11:40:44.505	-26:23:47.00	2.83	0.37	7.72	4.10	11.17
DKB05-3	2	50	11:40:43.761	-26:23:49.40	4.10	1.48	2.76	1.76	1.19
		100	11:40:43.768	-26:23:47.80	2.46	0.38	6.39	2.41	6.26
		250	-26:23:47.75	-26:23:47.75	1.39	0.23	6.02	2.33	10.10
		500	-26:23:47.70	-26:23:47.70	1.05	0.19	5.43	2.47	12.76
		0	-26:23:47.70	-26:23:47.70	0.91	0.19	4.84	2.23	11.81
		R03	-26:23:47.40	-26:23:47.40	0.88	0.22	4.11	1.33	6.18
DKB05-4	2	50	11:40:43.739	-26:23:50.30	5.24	1.94	2.71	2.77	1.43
		100	11:40:43.739	-26:23:50.20	3.08	0.65	4.75	3.28	5.06
		250	11:40:43.727	-26:23:50.35	2.10	0.39	5.43	2.28	5.89
		500	11:40:43.727	-26:23:50.40	1.80	0.34	5.27	2.26	6.62
		0	11:40:43.727	-26:23:50.40	1.64	0.32	5.19	2.19	6.95
		R03	11:40:43.727	-26:23:50.45	1.47	0.33	4.41	1.81	5.42
DKB05-5	2	50	11:40:44.416	-26:23:37.20	2.46	1.36	1.81	0.	0.
		100	11:40:44.319	-26:23:37.00	1.35	0.46	2.96	0.64	1.39
		250	11:40:44.308	-26:23:37.05	1.29	0.22	5.79	1.19	5.34
		500	11:40:44.308	-26:23:37.10	1.0	0.19	5.15	1.48	7.65
		0	11:40:44.300	-26:23:36.85	0.97	0.18	5.38	1.67	9.25
		R03	11:40:44.300	-26:23:36.85	0.93	0.19	4.98	1.41	7.55
DKB05-6	2	50	11:40:43.560	-26:23:29.50	1.89	1.55	1.22	0.	0.
		100	11:40:43.560	-26:23:29.50	3.83	0.82	4.68	2.06	2.52
		250	11:40:43.560	-26:23:29.60	2.73	0.39	7.02	3.92	10.11
		500	11:40:43.556	-26:23:29.65	2.08	0.34	6.10	4.28	12.52
		0	11:40:43.545	-26:23:29.60	1.98	0.35	5.73	3.87	11.19
		R03	11:40:43.545	-26:23:29.60	1.82	0.37	4.96	4.19	11.41
DKB08-1	1	50	11:40:33.291	-26:31:22.80	5.40	1.0	5.42	5.36	5.38
		100	11:40:33.299	-26:31:22.80	3.80	0.40	9.43	4.21	10.44
		250	11:40:33.303	-26:31:22.75	2.92	0.24	12.13	3.73	15.50
		500	11:40:33.303	-26:31:22.75	2.49	0.22	11.12	3.90	17.42
		0	11:40:33.303	-26:31:22.75	2.27	0.22	10.34	3.85	17.55
		R03	11:40:33.303	-26:31:22.70	2.26	0.25	8.96	3.67	14.54
DKB08-2	2	50	11:40:34.096	-26:31:25.70	1.86	0.57	3.29	1.30	2.29
		100	11:40:34.111	-26:31:25.80	1.25	0.26	4.78	1.17	4.49
		250	11:40:34.115	-26:31:25.95	0.80	0.14	5.79	1.12	8.08
		500	11:40:34.115	-26:31:26.00	0.70	0.12	5.67	1.09	8.81
		0	11:40:34.115	-26:31:26.00	0.65	0.12	5.30	0.90	7.28
		R03	11:40:34.118	-26:31:26.05	0.74	0.15	5.04	0.74	5.06
DKB08-3	3	50	11:40:33.791	-26:31:20.20	1.26	0.99	1.27	0.	0.
		100	11:40:33.895	-26:31:21.10	1.05	0.41	2.60	0.25	0.62
		250	11:40:33.902	-26:31:21.30	0.88	0.19	4.66	0.64	3.42
		500	11:40:33.902	-26:31:21.35	0.75	0.15	4.83	0.73	4.74
		0	11:40:33.899	-26:31:21.40	0.72	0.15	4.86	0.82	5.55
		R03	11:40:33.899	-26:31:21.35	0.69	0.18	3.93	0.72	4.10
DKB08-4	2	50	11:40:34.603	-26:31:17.90	6.19	1.31	4.71	4.89	3.72
		100	11:40:34.595	-26:31:18.10	3.95	0.68	5.82	4.26	6.28
		250	11:40:34.573	-26:31:18.20	2.92	0.42	6.90	3.28	7.77
		500	11:40:34.569	-26:31:18.25	2.58	0.36	7.26	3.86	10.88
		0	11:40:34.569	-26:31:18.25	2.37	0.34	6.93	3.72	10.89
		R03	11:40:34.569	-26:31:18.25	2.45	0.40	6.19	3.79	9.59
DKB10-1	1	50	11:40:44.047	-26:22:12.70	4.87	1.16	4.19	2.58	2.22
		100	11:40:44.025	-26:22:12.90	4.93	0.61	8.11	3.97	6.54
		250	11:40:44.025	-26:22:12.90	3.76	0.30	12.75	5.10	17.28
		500	11:40:44.025	-26:22:12.90	2.98	0.26	11.43	5.57	21.36
		0	11:40:44.021	-26:22:12.95	2.57	0.25	10.30	5.63	22.51
		R03	11:40:44.021	-26:22:12.95	2.19	0.30	7.35	4.95	16.64
DKB10-2	1	50	11:40:43.809	-26:22:11.20	2.55	1.06	2.40	0.77	0.73
		100	11:40:43.891	-26:22:11.30	1.65	0.56	2.97	0.85	1.52
		250	11:40:43.861	-26:22:12.50	1.55	0.30	5.20	0.97	3.26
		500	11:40:43.857	-26:22:12.50	1.57	0.26	5.97	1.12	4.23
		0	11:40:43.857	-26:22:12.50	1.54	0.25	6.27	1.18	4.81
		R03	11:40:43.857	-26:22:12.50	1.24	0.27	4.65	1.10	4.13
DKB10-3	2	50	11:40:43.928	-26:22:24.50	2.94	1.76	1.67	0.	0.
		100	11:40:43.928	-26:22:24.30	3.34	0.71	4.69	1.95	2.75
		250	11:40:43.924	-26:22:24.40	2.28	0.33	7.00	3.42	10.51
		500	11:40:43.924	-26:22:24.40	1.68	0.30	5.69	3.76	12.74
		0	11:40:43.924	-26:22:24.40	1.49	0.30	5.02	3.50	11.77
		R03	11:40:43.928	-26:22:24.35	1.62	0.35	4.60	2.99	8.51

DKB11-1	1	50	11:40:38.271	-26:31:55.90	3.57	0.79	4.54	2.53	3.22
		100	11:40:38.279	-26:31:55.90	2.49	0.37	6.82	2.89	7.90
		250	11:40:38.283	-26:31:55.85	1.92	0.24	7.97	1.98	8.20
		500	11:40:38.283	-26:31:55.85	1.67	0.18	9.07	2.05	11.16
		0	11:40:38.283	-26:31:55.80	1.48	0.17	8.66	2.09	12.23
		R03	11:40:38.290	-26:31:55.85	1.46	0.19	7.8	2.19	11.73
DKB11-2	3	50	11:40:38.227	-26:31:55.30	2.02	1.0	2.02	0.01	0.01
		100	11:40:38.100	-26:31:54.40	1.15	0.51	2.26	0.26	0.51
		250	11:40:38.100	-26:31:54.40	1.05	0.29	3.61	0.84	2.90
		500	11:40:38.107	-26:31:54.30	0.98	0.24	3.99	1.11	4.54
		0	11:40:38.111	-26:31:54.25	0.98	0.23	4.22	1.07	4.61
		R03	11:40:38.111	-26:31:54.25	1.43	0.25	5.68	0.71	6.78
DKB13-1	1	50	11:40:47.908	-26:27:47.50	1.35	0.56	2.42	0.55	0.98
		100	11:40:47.856	-26:27:48.80	1.31	0.45	2.92	0.62	1.38
		250	11:40:47.871	-26:27:48.65	1.02	0.21	4.87	0.95	4.51
		500	11:40:47.871	-26:27:48.65	1.05	0.19	5.65	0.83	4.51
		0	11:40:47.871	-26:27:48.65	1.06	0.18	5.98	0.80	4.54
		R03	11:40:47.871	-26:27:48.65	1.17	0.21	5.69	0.89	4.34
DKB13-2	3	50	11:40:48.206	-26:27:41.70	1.06	0.78	1.36	0.	0.
		100	11:40:48.303	-26:27:42.40	0.94	0.27	3.42	0.50	1.82
		250	11:40:48.292	-26:27:42.30	0.84	0.18	4.60	0.52	2.82
		500	11:40:48.292	-26:27:42.30	0.80	0.16	4.96	0.62	3.86
		0	11:40:48.292	-26:27:42.30	0.77	0.16	4.85	0.69	4.33
		R03	11:40:48.288	-26:27:42.30	0.97	0.18	5.44	0.76	4.29
DKB13-3	2	50	11:40:48.742	-26:27:53.40	0.60	0.71	0.85	0.	0.
		100	11:40:48.772	-26:27:52.90	0.94	0.46	2.04	0.04	0.08
		250	11:40:48.772	-26:27:52.85	1.26	0.23	5.57	0.77	3.40
		500	11:40:48.772	-26:27:52.85	1.12	0.19	5.87	1.12	5.86
		0	11:40:48.772	-26:27:52.90	1.06	0.19	5.48	1.30	6.68
		R03	11:40:48.772	-26:27:52.90	1.08	0.24	4.60	1.17	4.95
DKB14-1	1	50	11:40:42.358	-26:27:13.70	5.07	0.66	7.71	3.64	5.53
		100	11:40:42.358	-26:27:13.70	4.88	0.28	17.18	4.43	15.53
		250	11:40:42.358	-26:27:13.70	4.31	0.14	30.90	4.87	34.90
		500	11:40:42.358	-26:27:13.70	3.95	0.13	31.38	5.07	40.20
		0	11:40:42.354	-26:27:13.70	3.83	0.12	30.85	5.08	40.87
		R03	11:40:42.354	-26:27:13.70	3.78	0.13	28.00	4.61	34.20
DKB14-2	2	50	11:40:42.938	-26:27:16.80	3.05	0.60	5.07	2.51	4.18
		100	11:40:42.931	-26:27:16.70	1.89	0.32	5.91	1.95	6.07
		250	11:40:42.931	-26:27:16.85	1.21	0.23	5.32	1.24	5.43
		500	11:40:42.931	-26:27:16.90	1.10	0.20	5.49	1.30	6.52
		0	11:40:42.931	-26:27:16.95	1.07	0.19	5.52	1.33	6.84
		R03	11:40:42.935	-26:27:16.90	1.23	0.23	5.39	1.66	7.29
DKB16-1	1	50	11:41:2.373	-26:27:45.90	2.17	0.48	4.56	2.62	5.50
		100	11:41:2.395	-26:27:45.00	1.12	0.24	4.71	1.06	4.45
		250	11:41:2.395	-26:27:45.00	0.91	0.14	6.36	0.90	6.25
		500	11:41:2.395	-26:27:45.00	0.78	0.12	6.31	0.90	7.29
		0	11:41:2.336	-26:27:45.90	0.91	0.13	7.29	0.89	7.11
		R03	11:41:2.339	-26:27:45.90	0.87	0.14	6.41	0.83	6.09
DKB16-2	1	50	11:41:2.373	-26:27:45.90	2.17	0.48	4.56	2.62	5.50
		100	11:41:2.343	-26:27:46.00	1.19	0.22	5.31	1.39	6.17
		250	11:41:2.339	-26:27:45.95	0.97	0.15	6.58	0.97	6.59
		500	11:41:2.339	-26:27:45.95	0.92	0.13	7.04	0.87	6.65
		0	11:41:2.339	-26:27:45.05	0.68	0.12	5.61	0.89	7.27
		R03	11:41:2.395	-26:27:45.05	0.71	0.13	5.32	0.74	5.51
DKB16-3	2	50	11:41:2.879	-26:27:35.90	4.65	1.71	2.72	2.09	1.23
		100	11:41:2.894	-26:27:36.00	3.13	0.75	4.18	2.58	3.43
		250	11:41:2.894	-26:27:35.95	2.45	0.49	4.98	2.40	4.88
		500	11:41:2.894	-26:27:35.85	2.15	0.39	5.45	2.93	7.44
		0	11:41:2.894	-26:27:35.85	2.09	0.37	5.65	2.70	7.30
		R03	11:41:2.894	-26:27:35.90	2.09	0.41	5.08	2.88	6.99

Table 3.1: Tracked ALMA sources. (1) source ID, (2) quality factor, (3)-(4) RA and DEC both in J2000 format (hh:mm:ss and dd:mm:ss respectively), (5) peak flux [mJy/beam] (6) noise [mJy] quantified with ring method, also used as an estimate for the error on the flux, (7) S/N for peak flux, (8) integrated flux [mJy], (9) S/N for integrated flux.

These detections are associated to a quality flag to characterize their robustness. This flag is based on S/N and also distance from the center. In fact, we have already highlighted the behaviour of noise in the source extraction chapter: Figure 2.3 showed that noise increases as a function of the distance from the center, but also that its steepness grows as well. After about 10”, the noise pattern becomes suddenly large. Because of this, a source detected at the very edge of the ALMA fields should be considered with much more care, despite the fact that the noise computation method that we built is modelled so as it adapts the region in which sources are found by probing the surrounding field. Quality factor Q=1 is reserved to prominent, secure sources, either lying in the primary beam region and or in the edge but with high S/N ($\gtrsim$7). Sources with quality factor 2 are still considered secure, as they achieve the general criterion (S/N$\geq$5), but may be lying in the edge of the pointing. Finally, we add a quality factor Q=3 category, including those 7 sources that do not meet the 5σ criterion but just a 3σ threshold. In spite of the lower S/N, these sources are still included in the catalogue as they show evidence of having counterparts at other wavelengths. Distribution of the S/N values for the whole sample is shown in Fig. 3.1. In this figure, we see that stringent taperings (50, 100 kλ) show histograms that are skewed towards low S/N. This may be due to the higher rms pattern associated to heavy tapering, responsible for dampening the signal-to-noise ratio.

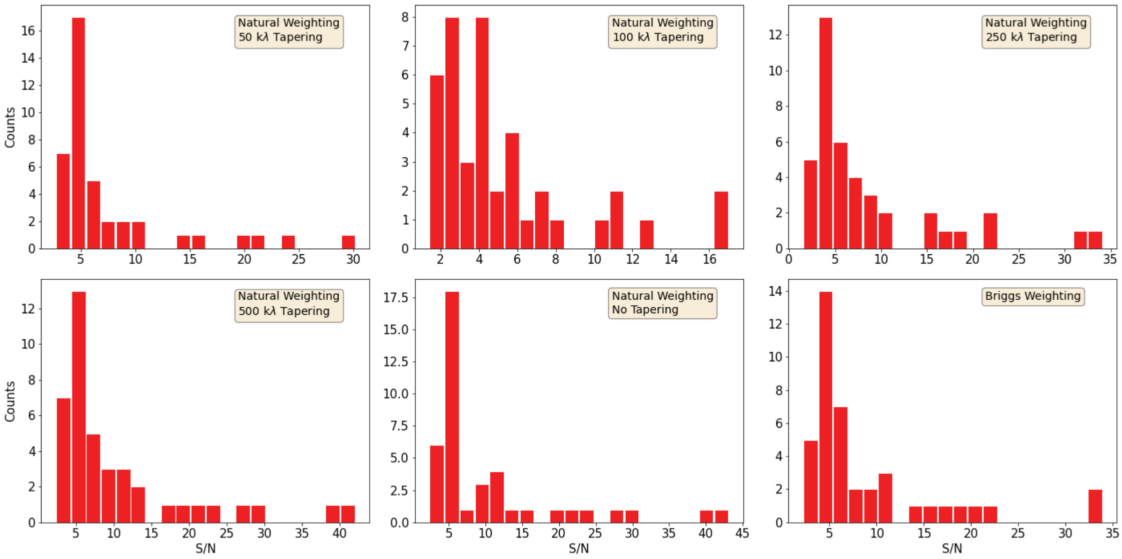

Figure 3.1: S/N distribution of all sources, displayed in the 6 different resolutions, using best flux estimator. Note that a source qualify as such when achieving 5σ in at least 3 configurations out of 6: this is why we see that even low S/N bins may be populated. Stringent taperings (50, 100 kλ) present densely populated low-S/N bins. This may be due to the higher rms pattern associated to heavy tapering, responsible for dampening the signal-to-noise ratio.

3.2 Multiplicity

In the past, interferometric follow-ups of bright, single-dish-selected sub-mm sources highlighted that a fraction of them may be a blend of multiple individual SMGs, which are unresolved under single-dish beams, that are typically

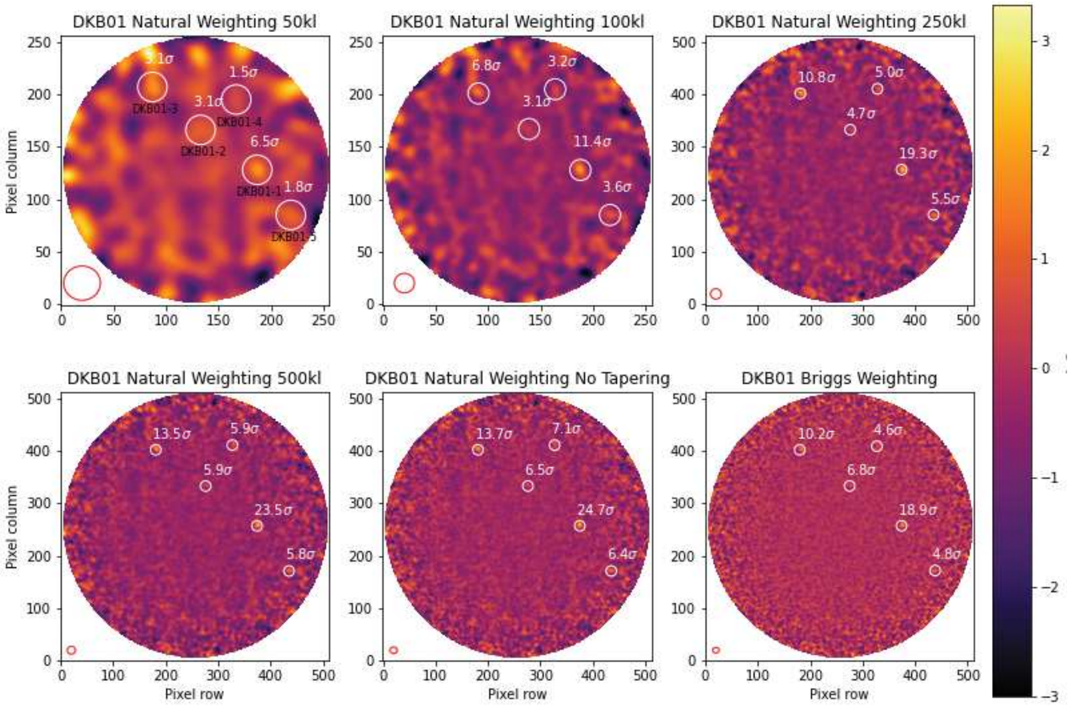

Figure 3.2: ALMA primary beam-corrected flux maps for LABOCA detection DKB01. From top to bottom, left to right: Natural Weighting with Tapering 50kλ, Natural Weighting with Tapering 100kλ, Natural Weighting with Tapering 250kλ, Natural Weighting with Tapering 500kλ, Natural Weighting with No Tapering, Briggs Weighting. White circles indicate the ALMA detections in this pointing. Beamsize on the bottom left (red ellipse) changes with the settings.

$\gtrsim$ 15" (Karim et al. 2013, Hodge et al. 2013, Simpson et al. 2015, Stach et al. 2018, Hill et al. 2018, Cairns et al. 2022). These bright SMGs split up into a number of fainter sources (usually with flux densities between 1 and 4 mJy, Stach et al. 2018), escaping poor resolution single-dish observations but revealed in the interferometric maps. This effect was referred to as "multiplicity" by Karim et al. (2013) and Simpson et al. (2015). ALMA made it easier to resolve those sub-mm blobs and explore the lower-flux end of the population of SMGs. In our case, the impressing ALMA resolving power is able to shed light on the LABOCA observations. In fact, ALMA deblends LABOCA sources into multiple detections that are candidate DSFGs, solving the confusion problem.

Of the 13 LABOCA sources targeted with this ALMA observation, 11 show evidence for multiplicity. Going in order from the lower multiplicity to the higher one, we have first LABOCA sources DKB04, DKB11 and DKB14 splitting into two ALMA detections each. DKB10, DKB13 and DKB16 split in 3 different sources, while DKB03, DKB08 split in four. DKB01 splits up in 5 different detections, and DKB05 divides into 6. Finally, DKB02 shows the highest multiplicity rate with seven different ALMA sources. To quantify the multiplicity of the sample, every LABOCA source is splitting on average into 3.7 ALMA detections, which is more than the average multiplicity found in the literature (2 to 3).

Figure 3.2 shows the detections revealed in the ALMA pointing of DKB01, indicated by the white circles in the 6 different weighting configurations. In this figure we also witness how heavy tapering causes the resolution to degrade, and this effect can be so marked that sources may be not visible. Signal-to-noise is reported next to the detection. All ALMA detections are reported in A.1. LABOCA sources DKB06 and DKB09 revealed no ALMA detection. In the evaluation made by Dannerbauer et al. (2014), DKB06 was already ruled out from the protocluster, while the membership of DKB09 was "to be defined". The fact that the fields of DKB06 and DKB09 show no detection may be due to the fact that the original LABOCA source splits in several faint sources that are all below the rms threshold of the ALMA observations. DKB06 and DKB09 both have LABOCA fluxes of $\approx$ 7 mJy. Being the rms=0.2 mJy in the lowest noise configuration and being our S/N threshold equal to 5, the minimum flux density of a source in our dataset is $\approx$1 mJy. This means that to make up for the LABOCA flux we would need $\gtrapprox$7 sources. In this case, the two maps do not show strong evidence for sources not even at 4σ, so this hypothesis seems unlikely. Another option could be that LABOCA sources DKB06 and DKB09 could be fake, even though both sources were detected at 3.9 σ by LABOCA. However, DKB09 was the only source of the LABOCA dataset for which Dannerbauer et al. (2014) did not find any Herschel counterparts.

Fig. 3.3 shows the relative position of the ALMA sources, in a coordinate system centered in the coordinates of the corresponding LABOCA detection DKB01, taken as an example. We note that the coordinates agree for all the weighting configurations, except for 50kλ that indeed has the lowest resolution. In any case, the disagreement between the different cleanings are $<$1". Different ALMA-detected SMGs inside the same map are typically separated by $>$3", corresponding to a minimum physical scale of about 25 kpc at this redshift.

Multiplicity fraction is defined as the number of single-dish SMGs that split up in multiple interferometric sources. Our multiplicity fraction is higher than the typical fraction reported in literature (about 40 to 60%, Karim et al. 2013, Stach et al. 2018, Hill et al. 2018, Cairns et al. 2022). We also point out that the number of galaxies we detect around a sub-mm emission is dependent on the sensitivity limit we set for our observations.

We note that our new ALMA detections mostly fall inside the LABOCA beam (FWHM = 19"), which means that most of these sources were blended and were altogether measured by LABOCA as a single emission spot. However, there are also cases in which ALMA detections fall at distances $\gtrapprox$ 10" from the coordinates of the LABOCA detection at the centre of the map, meaning outside the LABOCA beamsize. The distribution of distances of the detected ALMA sources from the associated LABOCA detection are represented in Figure 3.4, with a median of 6.7" and showing no particular trend. ALMA sources are detected with uniform probability within the ALMA pointing, mostly within the LABOCA beamsize. 6 sources are detected just outside the LABOCA beam. 3 of these sources all belong to the DKB05 pointing

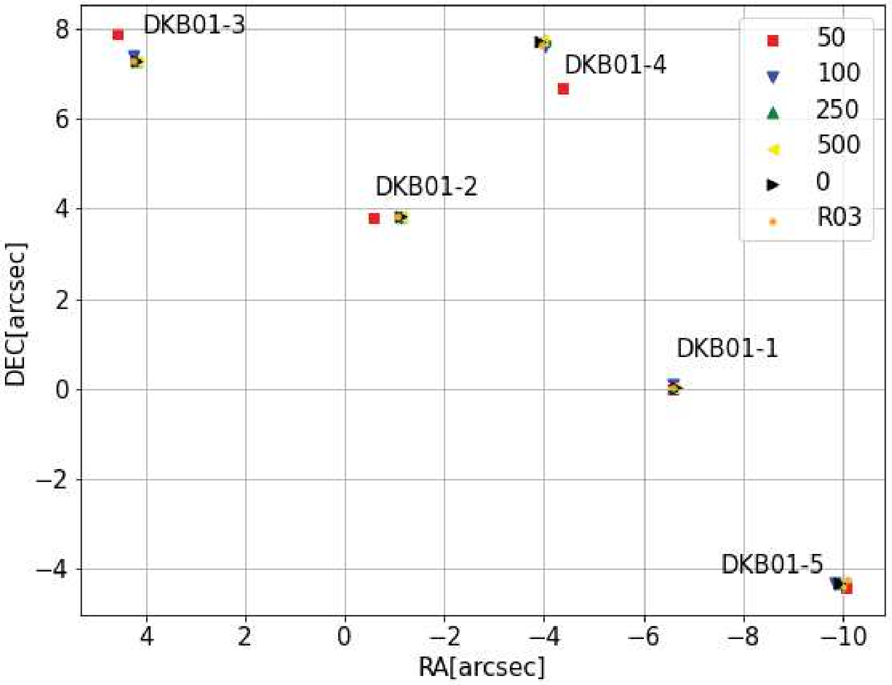

Figure 3.3: DKB01 ALMA sources, different shapes and colors are associated to different cleaning/tapering schemes. The coordinates obtained from different weighting configurations agree with high precision. Only 50kλ tapering (red squares) shows evidence of shifts, that are however $<$1”.

(DKB05-2, DKB05-4, DKB05-6). It could be that these sources were not detected by LABOCA as separate sources, meaning that it is possible that they were lying below the detection threshold ($\approx$ 3mJy). Moreover, undetected sources in single-dish instruments may contribute to noise (source confusion), lowering S/N and making faint source detection even harder.

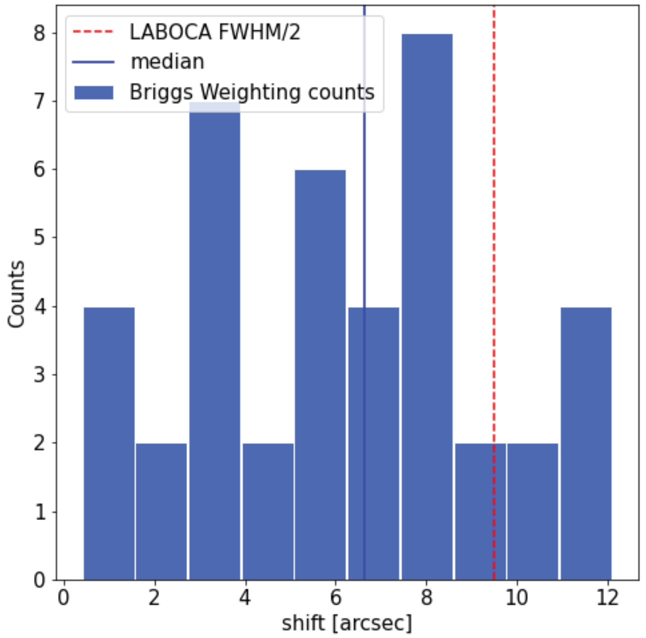

Figure 3.4: Counts of sources per distance from the center of the ALMA pointing. Vertical dashed line represents half of the LABOCA beamsize. 35 out of 41 sources are comprised within the LABOCA beamsize, 6 are maximum 2" outside of it. Blue solid line represents the median of the sample, equal to 6.7".

3.3 Flux measurements

After evaluating multiplicity, we switch to flux analysis: this involves peak flux and integrated flux, that we computed for all sources in the script. For flux analysis and number counts analysis we use all the quality flags. All the plots for the flux measurements of the single ALMA sources can be found in the appendix A.2. As an example, Figure 3.5 shows peak flux and integrated flux of the ALMA detections DKB01-1, DKB01-2, DKB01-3, DKB01-4 and DKB01-5 as a function of the beamsize in the different cleanings.

From Fig.3.5, we note that peak flux grows almost linearly as a function of beamsize, since heavy tapering allows to enhance the sensitivity to extended flux emission and recover the total flux by measuring the peak flux. This is because setting the threshold for the baseline at 50kλ guarantees that we are using just the smallest baselines available by the interferometric array. Smaller baselines give access to wider spatial scales. On the other hand, when we analyse untapered images, in order to maximise resolution, we may lose flux, since the long baselines only catch the smallest spatial scales in the real source plane.

Integrated flux has the opposite behaviour: with stringent tapering and wide beamsizes, the flux is spread over a wide area, that also includes more noise, causing an underestimation of the total flux. In high-resolution, compact configurations, narrower beamsizes better match the emission profile of the sources, making integrated flux a better estimator. In this case the beamsize is more compatible with the size of the galaxy, so the risk of including flux which is not associated to the brightness profile of the source is lower. Larger baselines allow to access the fine details of the image, the role of the wider spatial scales loses relevance. In this way, whilst obtaining high-resolution images, we lose the contribution to the flux associated to the outer part of the luminosity profile of the source.

These two trends can be seen very clearly in the top left panel of Fig.3.5, presenting the flux measurement of the ALMA source DKB01-1, but are evident even in the other panels, except for DKB01-2. In these sources we can observe that the rising trend of the peak flux and the decreasing trend of the integrated flux with respect to beamsize meet at a given configuration. The configuration at which the two trends cross, meaning where peak flux and integrated flux roughly correspond, is the configuration at which the source starts being resolved. For beamsizes smaller than that, the source can be considered resolved and the integrated flux becomes the best flux estimator.

Moreover, there is another interesting feature, visible in the panels of Fig. 3.5: the trend of the integrated flux shows a peak in one of the compact configurations (usually at 500kλ tapering or no tapering), and then a decrease for the smaller beamsizes. This could give us an indication of the angular size of the dust emission in the sky: when the beamsize becomes too narrow, we are cutting out the wings of the emission profile, thus causing a loss of flux, meaning that the source is over-resolved.

However, there are ALMA sources that are do not show this trend: for example, the trend of peak flux and integrated flux of DKB01-2 in Fig.3.5 is unclear and hard to interpret. We can just say that the source is probably unresolved at all configurations. It is also very faint, exposing our measurements to statistical fluctuations. The trends of peak flux and integrated flux can be seen also in the flux measurements of many other ALMA sources (A.2). In other cases, we do not see the trends, meaning that the source is faint and/or unresolved.

It is interesting to do a further check on the relationship between peak flux and integrated flux for a given ALMA source. Figure 3.6 (left panel) shows the ratio between peak flux and integrated flux as a function of the ratio between the source area and the synthesized beam area. The flux ratio should be in fact inversely proportional to the area ratio.

$$S_{peak} = S_{int}\frac{\Omega_{beam}}{\Omega_{source}} \tag{3.1}$$

Our measurements follow the trend, apart from a scale factor of ≈1.4. Moreover, the right panel also reports the correlation between peak flux and integrated flux, which are scattered around the $S_{peak} = S_{int}$ line. As expected, peak flux is greater than integrated flux for stringent tapering, while integrated flux is bigger in the lightly tapered, high resolution images.

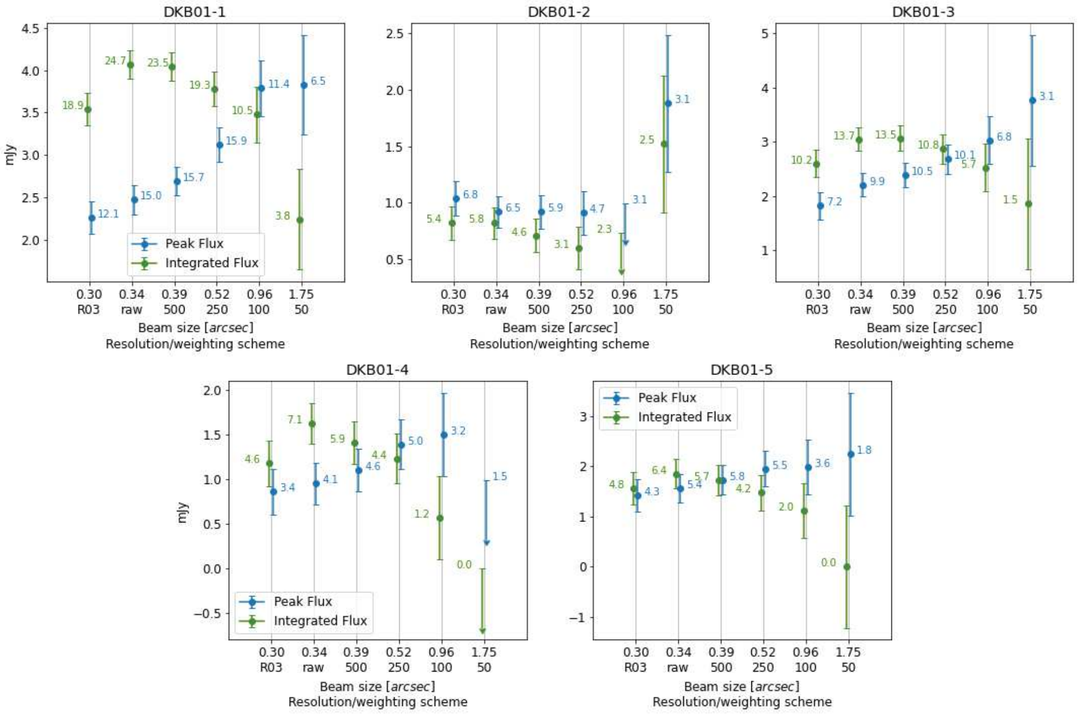

Figure 3.5: Peak flux and integrated flux for all 5 ALMA DKB01 sources. S/N is reported next to the dots. We note that in all panels but DKB01-2 there is a trend for the fluxes. Peak flux grows with beamsize, since extended configurations of heavy tapering allow to recover the total flux by measuring the peak flux. Integrated flux has the opposite behaviour, since with stringet tapering and wide beamsize, the flux is spread around a wide area, that also includes more noise, causing an underestimation of the total flux. On the other hand, in high-resolution, compact configurations, narrower beamsizes better match with the emission profile of the sources, making integrated flux a better estimator. DKB01-2 does not show such behaviour, meaning that the source may be unresolved in all configurations.

From this discussion we can conclude that for each source, a "best" flux estimator is available depending on whether or not the emission is resolved. For a given tapering scheme (and therefore for a given beamsize), if the peak flux is larger than the integrated flux, it means that the source is unresolved, or point-like, and the peak flux is the best estimate for the total flux. On the other hand, if the integrated flux is larger than the peak flux, then it means that the emission area associated to the source is larger than the beam, i.e the source is resolved and can be explored with the beamsize of the instrument. In this case the best estimate for the flux corresponds to the integrated flux.

For the first part of the discussion (flux measurements) of this work, we compare both fluxes, while for the number counts, we will use always the best flux estimator, meaning the one that best fits the source according to whether or not it is resolved by the instrument.

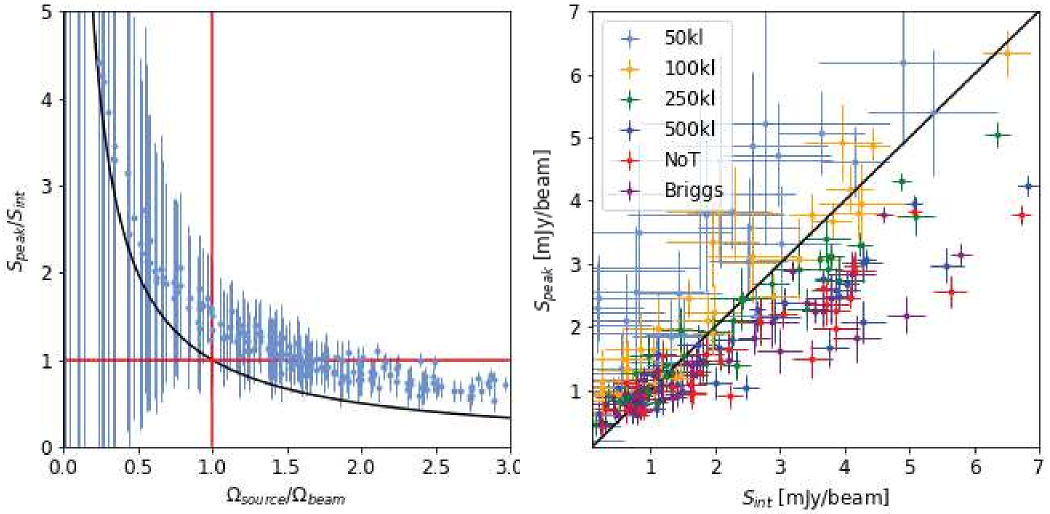

Figure 3.6: Left panel: ratio between peak flux and integrated flux as a function of the ratio between the source area and the synthesized beam area. The black line represents the expected inverse proportionality. The red cross highlights the position along which the peak flux corresponds the integrated flux, and thus the synthesized beam should correspond to the emission area of the source. Right panel: correlation between peak flux and integrated flux: different colors represent different weighting schemes. Horizontal and vertical errorbars are given by the estimated uncertainty on the fluxes (noise).

3.4 Flux comparison with LABOCA

As shown in the previous paragraph, ALMA resolution power dramatically reduces source confusion and enables deblending the LABOCA detections, that split into multiple sources. Flux measurements of these ALMA sources allows an unprecented comparison to LABOCA flux measurements: we want to compare the sum of the fluxes of the ALMA detections to the LABOCA flux. As already mentioned, we measured the flux in two ways: peak flux and integrated flux. Table 3.1 showed both values for every ALMA source. In this section, we discuss both quantities in our analysis, in order to see how they behave with respect to the original LABOCA flux.

Figure 3.7 includes 11 plots, one for each ALMA pointing in which we found detections, displaying the sum of the individual ALMA sources flux, compared to the LABOCA flux density measurement reported by Dannerbauer et al. (2014). In these plots we use both peak flux and integrated flux, and also the best flux estimator for each ALMA source. Errors on ALMA flux density measurements are given by the noise estimated on the surroundings with our "ring" method. The summed ALMA flux is given for each different tapering scheme.

By looking at the different plots of Figure 3.7, we note that the peak and integrated fluxes behave similarly to the case of the individual detections reported in Fig.3.5, with the peak flux growing and the integrated flux decreasing as a function of beamsize. Also, the average position of the peak of integrated flux trend may be suggesting that the average size of the dust emission measured by ALMA is between 0.3 and 0.5 arcsec.

Figure 3.8 is another way to represent this trend: we plot the percentage of flux recovered with respect to LABOCA as a function of the different taperings, with a different color assigned to each LABOCA detection. Peak flux is represented in the left panel, integrated flux in the right one. Overall, flux recovery fractions oscillate between 50 and 150%, apart from DKB05, for which the fraction is well above 100% for all taperings. We note as well that DKB03, DKB11 and DKB13 all have low recovery rates, of about 60-70%, both for peak flux and integrated flux.

We decide to compare the LABOCA fluxes using the sum of the "best fluxes" of the ALMA single sources in the different taperings, as reported in Table 3.2, instead of separately evaluating peak and integrated flux.

From Table 3.2 we can see that in 6 cases out of 11 the most stringent tapering (50kλ) recovers more flux than LABOCA, which is taken as a reference for this analysis. To further quantitatively support our study, we can compute the weighted average of the recovery rate for every resolution, which we display in Table 3.3, using the best flux estimator. Table 3.3 shows in fact that the average ALMA to LABOCA flux ratio at 50kλ tapering is higher than 1.

Instead, at 100kλ tapering the average fraction is close to 1. According to Table 3.2, 100kλ best flux is compatible with LABOCA in 7 cases out of

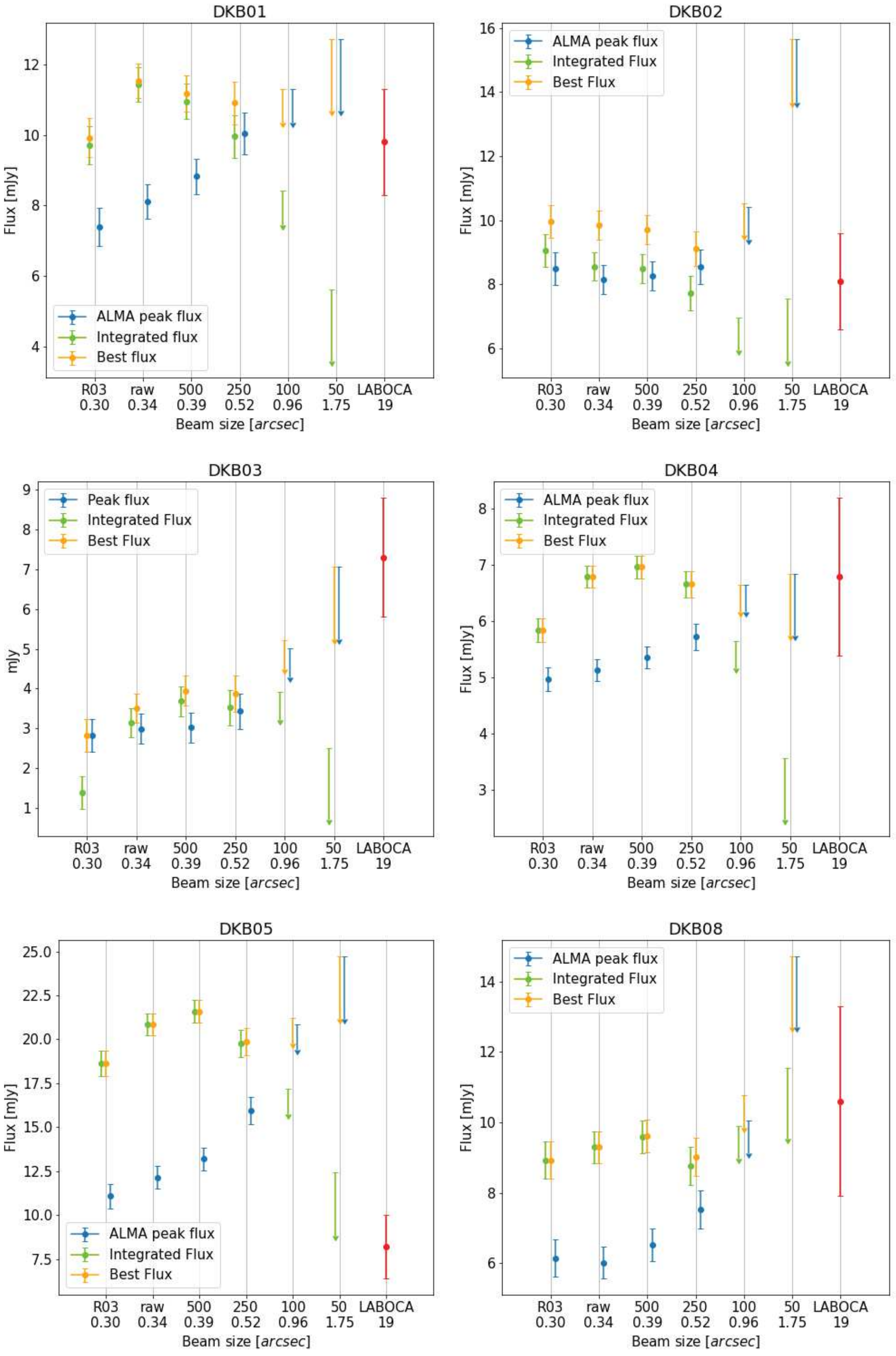
DKB01
Flux [mJy]
ALMA peak flux
Integrated flux
Best flux
DKB02
ALMA peak flux
Integrated Flux
Best Flux
DKB03
mJy
Peak flux
Integrated Flux
Best Flux
DKB04
DKB05
DKB08
R03 0.30
raw 0.34
500 0.39
250 0.52
100 0.96
50 1.75
LABOCA 19
Beam size [arcsec]

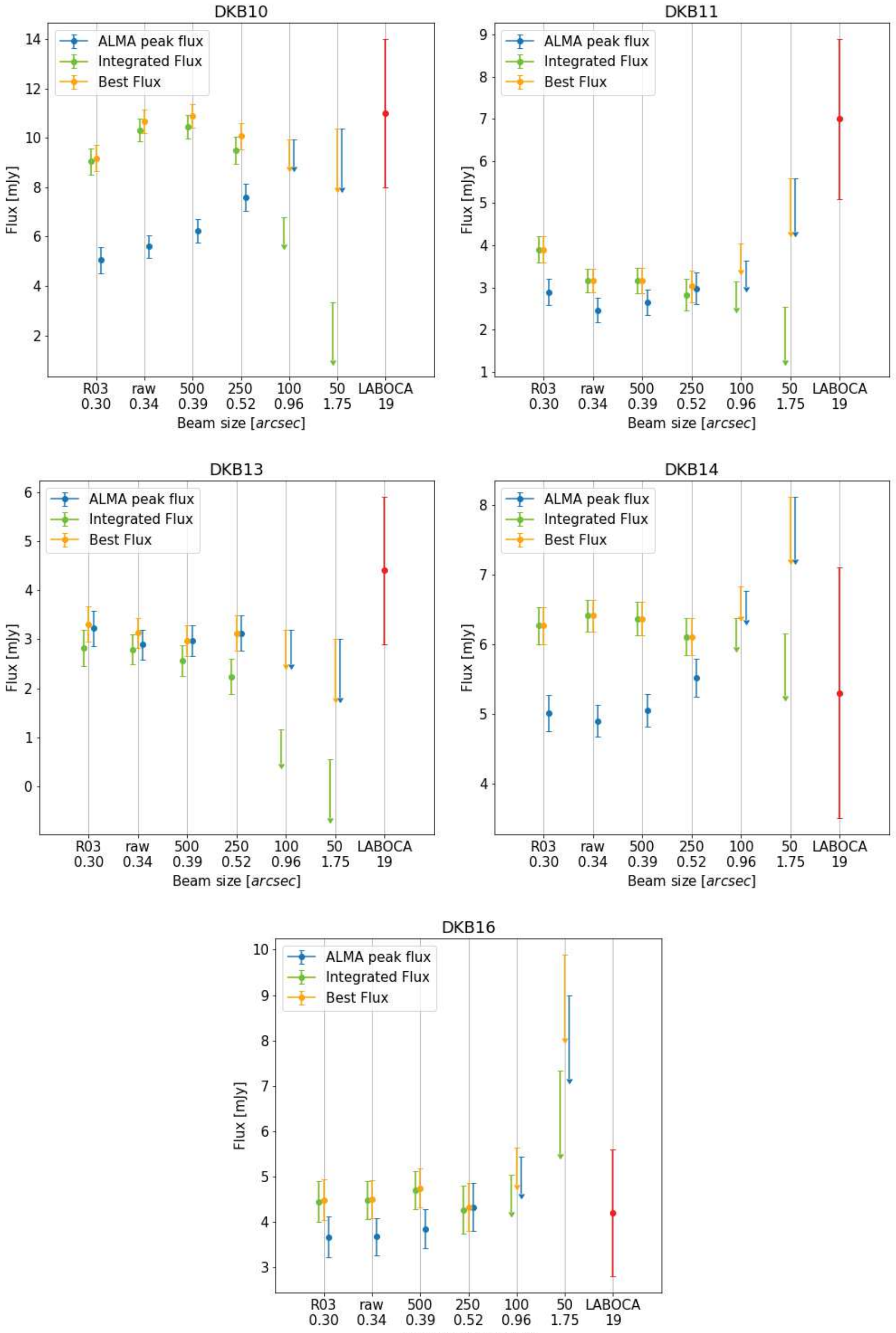

Figure 3.7: The sum of the individual ALMA sources flux is compared to the LABOCA flux density measurement reported by Dannerbauer et al. (2014). We use both flux estimators, peak flux and integrated flux, and also the best flux estimator for each ALMA source. Errors on ALMA flux density measurements are given by the noise estimated on the surroundings with our "ring" method. The summed flux is given for each different tapering scheme. We observe the same behaviour previously discussed in the single-source flux plots: peak flux growing as a function of beamsize, integrated flux peaking at small beamsizes.

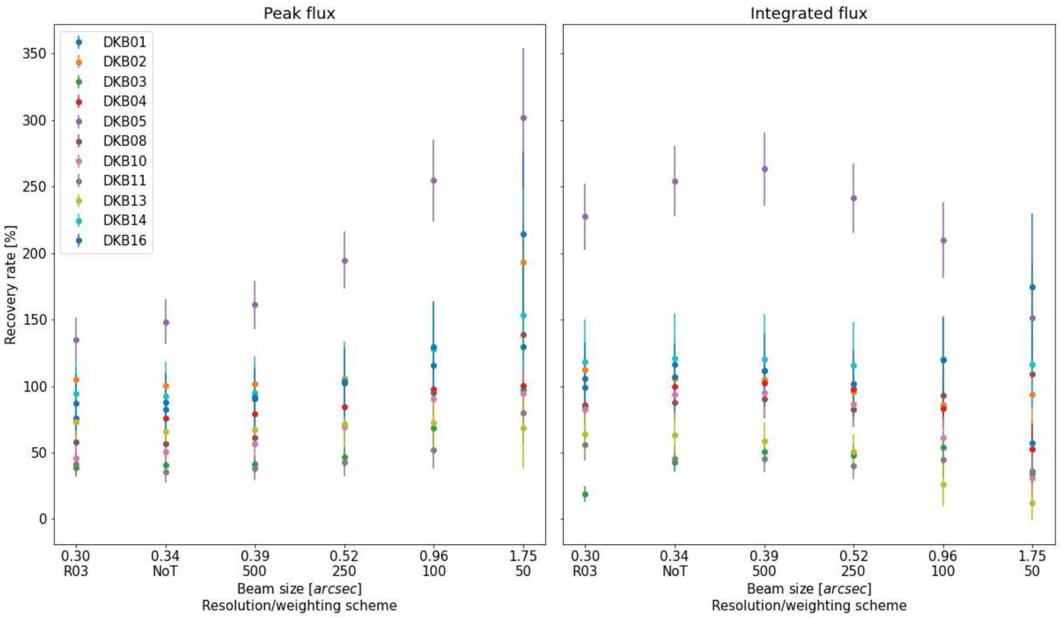

Figure 3.8: Plots of recovery rates in percentage, we display both peak flux (left panel) and integrated flux measurements (right panel). We can see how peak flux at heavy tapering recovers more flux, while integrated flux recovers more flux with high-resolution, light tapering.

11. DKB03, DKB05, DKB11 and DKB13 do not match within 1σ, where σ is the sum of the uncertainties of LABOCA and ALMA. DKB05 has much more ALMA flux than expected from LABOCA at all resolutions. This could be due to source confusion affecting the bolometer: in fact we notice that in this field, 3 ALMA detections (DKB05-2, DKB05-4 and DKB05-6) lie outside the beamsize of LABOCA. Therefore, these ALMA sources could be escaping detection in the LABOCA maps, contributing to noise rather than to the emission. If we sum the flux of the only three sources that are rigorously inside the LABOCA beam, we get a recovery rate of $(125 \pm 21)\%$ at 100kλ, which now is a match if we also consider the uncertainty of LABOCA fluxes. In the three other cases (DKB03, DKB11, DKB13) our main hypothesis is that there may be other sources lying below ALMA flux sensitivity at this wavelength. If this hypothesis held, intrinsic multiplicity for the Spiderweb field could be even higher than predicted by this work.

After correcting for DKB05, ALMA flux at 100kλ is compatible for LABOCA within 1σ uncertainty in 8 out of 11 cases, which is the highest fraction among all taperings. In Figure 3.9 we plot the ratio S_{ALMA}/S_{LABOCA}, using the ALMA 100kλ best flux, as a function of the flux of the original LABOCA source. The uncertainty is given by the quadrature between LABOCA and ALMA errorbars.

Finally, light-tapered or not tapered images gather on average about 80% of the LABOCA flux (Table 3.3). This could mean that, even using integrated flux, with not tapered or lightly tapered flux maps we may be losing a fraction

LABOCA id	LABOCA flux [mJy]	ALMA recovered flux [mJy]					
		50kλ	100kλ	250kλ	500k	NoT	Briggs
DKB01	9.8 ± 1.5	12.7 ± 2.0	11.3 ± 1.0	10.9 ± 0.6	11.2 ± 0.5	11.5 ± 0.5	9.9 ± 0.5
DKB02	8.1 ± 1.5	15.65 ± 2.0	10.5 ± 1.0	9.1 ± 0.5	9.7 ± 0.5	9.9 ± 0.4	10.0 ± 0.5
DKB03	7.3 ± 1.5	7.1 ± 1.8	5.2 ± 0.7	3.9 ± 0.4	4.0 ± 0.4	3.5 ± 0.4	2.8 ± 0.4
DKB04	6.8 ± 1.4	6.8 ± 1.1	6.7 ± 0.5	6.7 ± 0.2	7.0 ± 0.2	6.8 ± 0.2	5.85 ± 0.2
DKB05	8.2 ± 1.8	24.7 ± 3.6	21.2 ± 1.5	19.9 ± 0.8	21.6 ± 0.7	20.9 ± 0.6	18.7 ± 0.7
DKB08	10.6 ± 2.7	14.7 ± 2.0	10.8 ± 0.9	9.0 ± 0.5	9.6 ± 0.5	9.3 ± 0.4	8.9 ± 0.5
DKB10	11.0 ± 3.0	10.4 ± 2.4	9.9 ± 1.1	10.1 ± 0.5	10.9 ± 0.5	10.7 ± 0.5	9.2 ± 0.5
DKB11	7.0 ± 1.9	5.6 ± 1.3	4.0 ± 0.6	3.0 ± 0.4	3.2 ± 0.3	3.2 ± 0.3	3.9 ± 0.3
DKB13	4.4 ± 1.5	3.0 ± 1.2	3.2 ± 0.7	3.1 ± 0.4	3.0 ± 0.3	3.1 ± 0.3	3.3 ± 0.4
DKB14	5.3 ± 1.8	8.1 ± 1.3	6.8 ± 0.6	6.1 ± 0.4	6.4 ± 0.3	6.4 ± 0.3	6.3 ± 0.4
DKB16	4.2 ± 1.4	9.9 ± 1.8	5.6 ± 0.8	4.3 ± 0.5	4.8 ± 0.4	4.5 ± 0.4	4.5 ± 0.5

Table 3.2: Comparison between LABOCA flux and ALMA-recovered "best" flux.

Resolution	S_{ALMA}/S_{LABOCA}
50kl	1.21 ± 0.09
100kl	0.99 ± 0.05
250kl	0.84 ± 0.04
500kl	0.86 ± 0.04
NoT	0.83 ± 0.04
R03	0.78 ± 0.04

Table 3.3: Weighted average of recovery rate of all sources at each resolution, based on best flux.

of the intrinsic flux of the source, for the sake of high resolution. This is called missing flux issue or SSP (short-spacing problem, Braun & Walterbos 1985, Faridani et al. 2017). However, another explanation could be that the missing flux could be due to possible missing ALMA sources with low S/N.

We note that on a theoretical level, the heaviest tapering (50kλ) should be our first choice at recovering extended emission. However, in this configuration setting, the resolution is so low and the noise pattern is so high that in some cases ($\approx 30\%$ of our catalogue) the source have very low S/N and we have a hard time in properly viewing and locating it at 5σ. For this reason, the 100kλ tapering turns out to be the best option to recover the LABOCA flux.

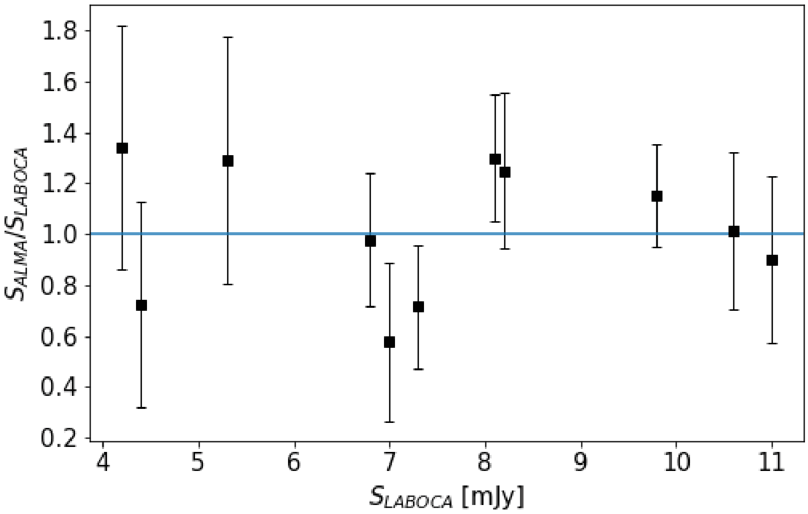

Figure 3.9: Recovery fraction for flux density ALMA/LABOCA, using ALMA tapering at 100 kλ. See that uncertainties are generally higher for faint sources. Errrobars are given by the quadrature between LABOCA and ALMA errrors. We recover the LABOCA original flux within 1σ in 8 out of 11 sources. Note that the ratio DKB05 was substituted with the one obtained by only summing the three source strictly lying within the LABOCA beam.

3.5 Counterpart matching

In this section we present the result of a visual comparison of the extracted 870μm ALMA sources with datasets at other wavelengths, taking note of the possible counterparts. This will possibly be the basis for future SED fitting, to recognize the nature of the source as well as its physical features. Counterparts in a given band are searched within a matching radius given by the spatial resolution of the specific instrument used in that band. Not all available datasets have full coverage.

Table 3.4 reports the global fraction of sources for which we found counterparts in the observations available at different wavelengths. Note that in general counterpart identification of a sub-mm population can be affected by the sky surface density of sources at the matching wavelength, as well as by the sensitivity of the used dataset. In B we show Table B.1, reporting whether or not we found a candidate counterpart per each ALMA detection and per each available dataset.

Of the possible available bands, we note that optical/NIR range is useful to probe the physical nature of the the population that we are observing: SMGs should be partially or significantly obscured in this wavelength regime. They should be instead more visible in the FIR, which is closer to the emission peak of dust continuum.

Radio counterparts are also useful to probe the SMG nature of the submm emission. In fact, radio sources are relatively rare, making candidate counter-

Telescope/Instrument/Band	**Match Rate**
HST/ACS/814nm	58%
HST/NICMOS/1.1μm	40%
HST/NICMOS/1.6μm	40%
Subaru/MOIRCS/NB2071	40%
Subaru/MOIRCS/K_s	47%
VLT/HAWK-I/Y	29%
VLT/HAWK-I/H	34%
VLT/HAWK-I/K_s	39%
VLT/ISAAC/K_s	43%
Spitzer/IRAC/ch1	74%
Spitzer/MIPS/24μm	74%
VLA 1.4GHz	35%
Chandra	5%
Catalogue	**Match Rate**
HAEs (Koyama et al. 2013)	27%
HAEs (Shimakawa et al. 2018)	21%
LAEs (Kurk et al. 2004a)	10%

Table 3.4: Visual match rate between ALMA sources and the available bands and catalogues.

parts more likely to be unique. On the contrary, optical catalogues are often crowded in detections, creating the issue of multiple matching (also due to the large beamsizes). Large beamsizes have always been an issue: they lead to large uncertainties in the determination of the position of submm sources and possibly to multiple matching. Multiple matching hinders the determination of the true coordinates of a given source.

Catalogues of galaxies with $H\alpha$ in emission (also known as HAEs) can provide information about unobscured star formation, assuming that we are able to detect the H_α, which is a signpost of star formation, at this redshift. HAE counterparts were detected for this protocluster in Dannerbauer et al. (2014), so we inspect the available catalogues for our ALMA sources as well.

We report an example of counterpart matching of our ALMA sources in the VLT/HAWK-I/K_s band (NIR), which is among the deepest maps available for this field. Figure 3.10 shows the ALMA maps (left panels) compared to the corresponding region in the NIR (right panels), where the ALMA sources are marked with a 1" circle, and color-coded based on the quality factor of the sources.

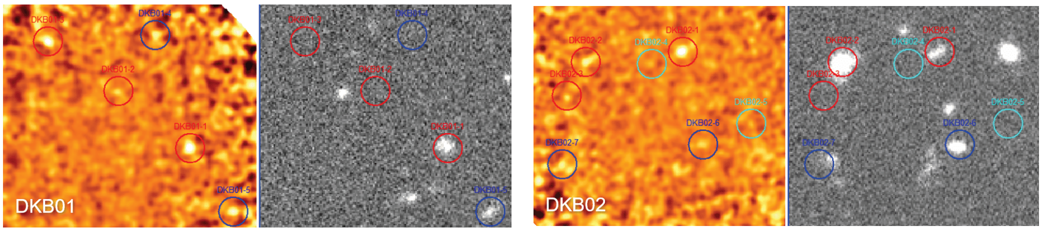
DKB01-3
DKB01-4
DKB01-2
DKB01-1
DKB01-5
DKB01
DKB01-3
DKB01-4
DKB01-2
DKB01-1
DKB01-5
DKB02-2
DKB02-4
DKB02-1
DKB02-3
DKB02-5
DKB02-6
DKB02-7
DKB02
DKB02-2
DKB02-4
DKB02-1
DKB02-3
DKB02-5
DKB02-6
DKB02-7

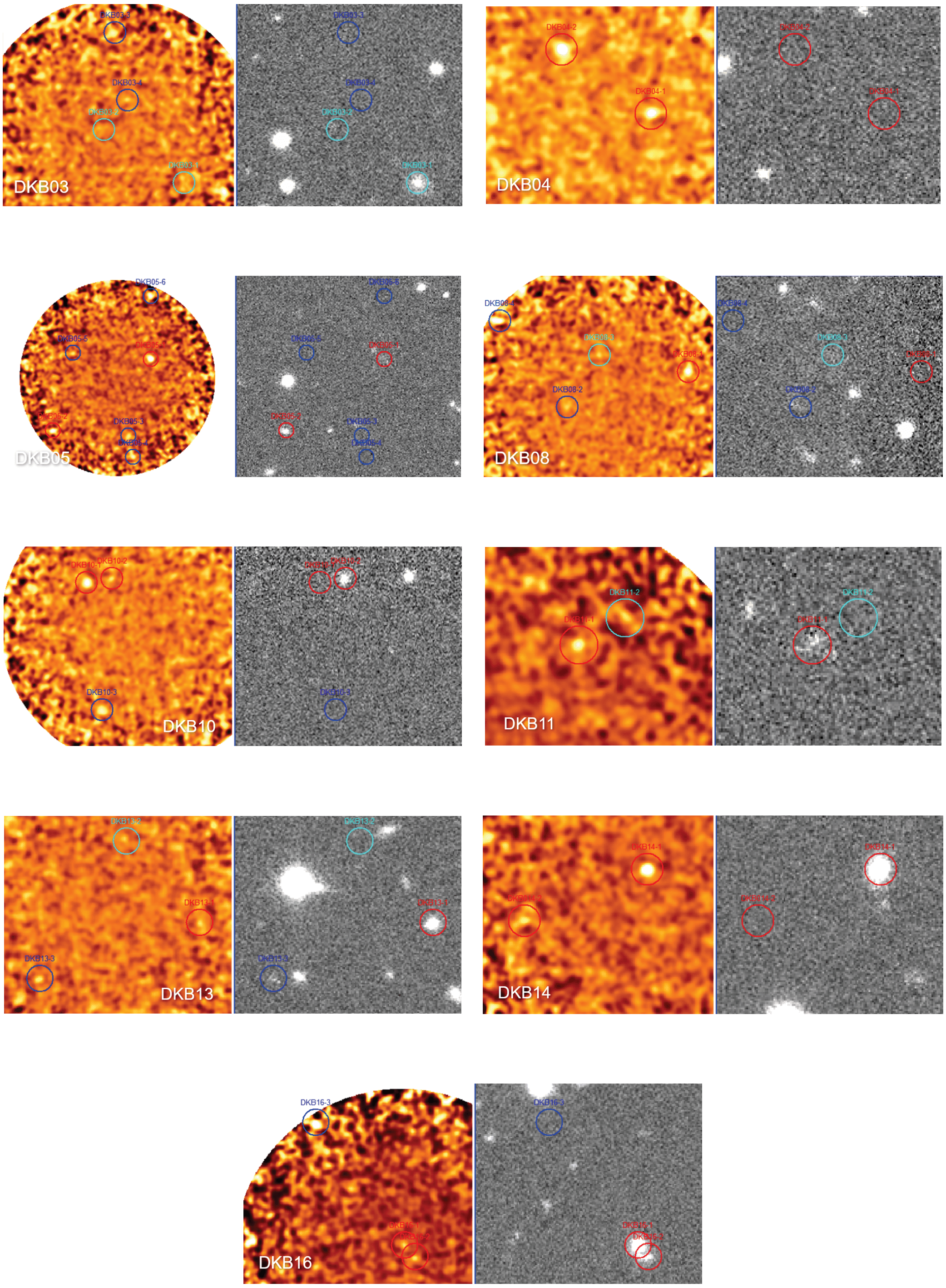
DKB03
DKB04
DKB05
DKB08
DKB10
DKB11
DKB13
DKB14
DKB16

Figure 3.10: Comparison between our natural-weighted, 250kλ-tapered ALMA flux maps (left panels) with the K_s band, probed by VLT/HAWK-I (right panels). Circles mark the detected ALMA sources, color-coded based on the quality factor: red for Q=1, blue for Q=2, cyan for Q=3.

3.5.1 NIR/Optical counterpart matching

Optical Matching large submm beamsize with the extremely narrow ones from optical astronomy can yield very high failure rates. This issue has always affected single-dish instruments in the submm regime. In our case, ALMA beamsizes are comparable with the FWHM of the most exquisite optical devices. HST yields a detection rate of 58% at 814 nm. We keep in mind that we are investigating sub-millimiter galaxies, that are heavily obscured in the optical regime by definition. Therefore, we do not expect a high matching rate for this population in the optical, but rather at longer wavelengths, depending on the depth of the other bands.

NIR The datasets available from HST/NICMOS 1.1μm and 1.6μm filters have a poor coverage of the LABOCA field. Just 5 ALMA detections are also covered by these data, and 2 of them show the presence of a counterpart. VLT HAWK-I filters (Y,H,K_s (Fig.3.10), centred at wavelengths 1, 1.6 and 2.1μm) cover all ALMA detections and show a counterpart identification rate of 29%, 34% and 39% respectively. Broad K_s band was also investigated by VLT ISAAC, where the counterpart rate is found to be 43%, and by Subaru/MOIRCS, with a 47% rate. These fractions are slightly higher than what we found in VLT/HAWK-I in the same wavelength regime, but this could be due to different sensitivities of the surveys. Narrow band observations at the same wavelength are also provided by Subaru/MOIRCS/NB2071, for which we report a 40% match rate with our ALMA catalogue.

NIR data are also available through Spitzer/IRAC (3.6 μm) and the reported rate is ≈74%, but just covering approximately half of the investigated field (19 of the sources detected by ALMA). IRAC is characterized by a beamsize (and thus a matching radius) of 2”, which is shorter than the average separation between the sources of the ALMA detections. This makes the identification process less plagued by multiple matching and thus more reliable.

MIR The reported rate for MIPS (24 μm) is ≈74%. MIPS covers the same region as IRAC, meaning 19 ALMA sources, and each IRAC alleged counterpart is also associated to a MIPS counterpart. MIPS matching rate, with a matching radius of 6.7”, is less reliable and would probably require the counterpart matching method to be more refined than our simple visual one. Correlating sub-mm sources with these MIPS mid-infrared emission spots is often a complicated task, due to extra factors like the presence of PAHs absorption and emission features altering IR dust continuum for z<4 (Casey, Narayanan & Cooray 2014).

3.5.2 FIR cross-identifications

This wavelength is close to our ALMA observations: FIR observations probe the dust continuum around the peak. We remind that the peak of dust emission at this redshift should be placed between 300 and 600μm. Being FIR sources surface density much higher than radio, whilst not as high as optical catalogues, FIR matching is a great second alternative for counterpart identification.

We exploit data from Herschel/PACS and SPIRE. Catalogues in this range are extremely crowded (large surface density) and Herschel beamsizes (see

Table 3.4) are larger than the average separation between sources. Therefore, finding the true positions of sources is a cumbersome task. PACS 100μm seems to have a higher match rate than the 160μm filter. This is in line with the predicted behaviour: in this regime the SED should be rising towards the peak, so the higher λ, the brighter the detected sources should be. Therefore, we expect a higher number of counterparts (cf. Dannerbauer et al. 2010).

SPIRE bands should reveal the SMG population, since it could be probing emission between the peak and the long-λ tail of the dust continuum emission. However, we should keep into account the 3σ sensitivities of the datasets that we have, that are 7.5, 8 and 9 mJy in the three bands (250, 350 and 500μm): it can be very hard to detect faint sources with these low sensitivities. Moreover, SPIRE band have very large beamsizes (18", 25" and 36" in the three bands), so there would be large uncertainties on detection rates, and source blending may affect SPIRE detections dramatically (Dannerbauer et al. 2014). Further analysis would be needed to shed light on such counterparts.

Regarding flux, according to the behaviour of the dust blackbody radiation model, sources with redshift between 2 and 3 should peak in the observed 350μ band. This is because the emission shifts of a factor (1+z) and the rest frame peak of dust emission is usually at between 100 and 200μm (see 1.1). This means that at 500μm we predict our ALMA-detected sources to be brighter than at 870μm, and thus we expect to find counterparts. Using the blackbody approximation in the Rayleigh-Jeans limit ($S_\nu \propto \nu^2$), we expect the flux densities of our ALMA sources to range between 3 and 12 mJy at 500μm.

3.5.3 Radio counterparts

Radio identification (ID) of counterparts has been extremely useful in the past, in particular the one performed with VLA 1.4GHz band, due to the documented correlation between radio and FIR flux densities in star-forming galaxies. Evidence for the aforementioned radio-FIR correlation is connected to radio synchrotron emission of Supernova remnants, which like dust is an end product of luminous, massive stars (Murphy 2009, Ivison et al. 2010). Moreover, radio galaxies are much less frequent than optically bright objects, therefore the risk of multiple matching is reduced. On the other hand, the downside of radio matching is that a high fraction of submm sources do not have a radio counterpart at all.

Dannerbauer et al. (2004) report that about 60% of the SMGs detected by MAMBO in the NTT Deep Field region for which VLA coverage is available has a radio counterpart. Chapman et al. (2003) and Barger, Cowie & Wang (2007) report similar fractions, with a radio counterpart identification rate of 66% for bright submm emission ($\gtrsim$5 mJy) and of 40% to 50% for fainter sources. We can compare these results with the identification that we worked out between our sub-mm sample and VLA 1.4 GHz data: only three sources lie above have fluxe densities greater than 5 mJy (DKB05-1, DKB10-1 and DKB14-1) and 2 of them (DKB05-1 and DKB14-1) seem to have a clear radio counterpart, thus our results overlaps with the reference from literature for bright sources.

Instead, if we consider our whole ALMA sample, whose median is around 1 mJy, we get a radio counterpart matching rate of about 36%, which is below the one reported in the reference for shallow detections. One reason for this could be the limited dynamic range of the VLA dataset, caused by the strong emission of MRC1138-262. This makes our VLA map shallow in comparison to other deep VLA integrations of submillimeter fields (Morrison et al. 2010). It is also well-documented that the fraction of SMGs with robust counterparts is a function of the sensitivity of the radio dataset (Biggs et al. 2011). It would be important to investigate such relation in our sample as well. From our initial, visual analysis, there seems to be a connection between bright 870 μm emitters and radio counterparts.

We also show some diagnostics plots, used by Ivison et al. (2002) to further investigate the correlation between radio and sub-mm emission. In Figure 3.11 we show three panels displaying the cumulative distribution of the radio counterpart identification rate versus ALMA 870μm flux, S/N and noise respectively. The left panel of Fig. 3.11 shows that the counterpart identification rate is 40% for higher fluxes, while it decreases to 25% in the 1-3 mJy bins. This could be linked to the well-known radio-sub-mm flux correlation: faint sources in the submm are also faint in the radio, therefore the fainter the source, the fainter its radio counterpart and the harder its identification (Biggs et al. 2011).

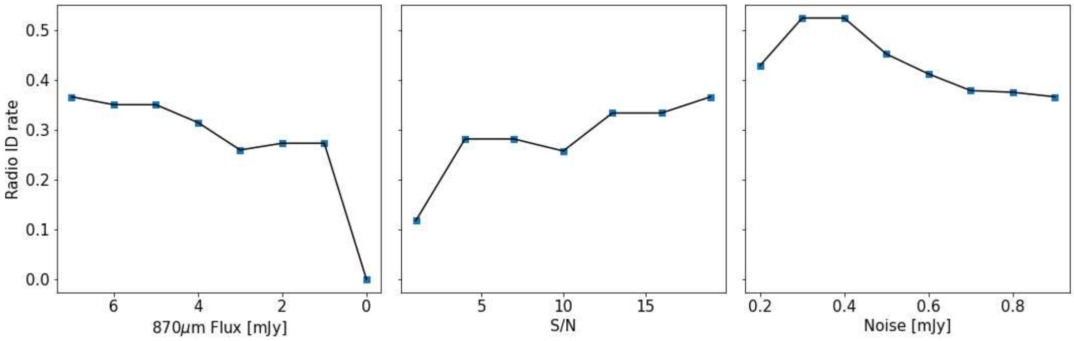

Figure 3.11: Cumulative radio-870μm identification rate versus 870μm flux (left panel), S/N (middle panel) and noise (right panel).

The middle panel shows again the same rate but as a function of S/N of the sources. This shows a weak trend between signal-to-noise ratio and matching rate, suggesting an anticorrelation between the two sources. This supports the idea that weak sub-mm sources are probably associated to radio sources that are faint as well, and therefore harder to detect.

A slight trend can be noticed in the right panel, that plots the radio counterpart matching rate as a function of the noise associated to the regions in which the sources lie. There is thus weak evidence for a correlation between low-noise regions and the presence of a radio counterpart. This hypothesis

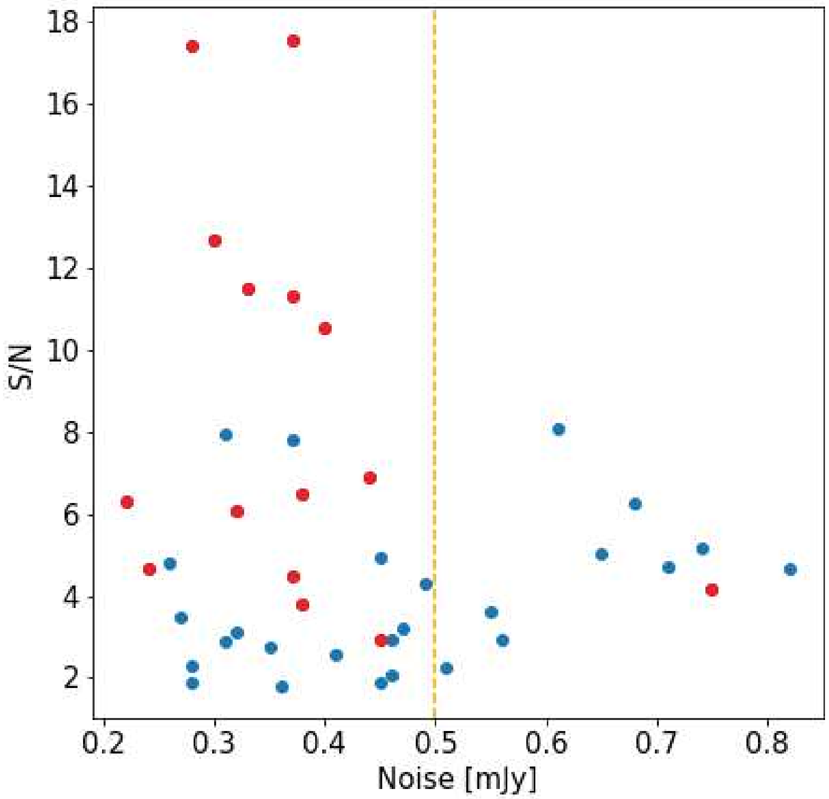

Figure 3.12: Noise versus S/N of the ALMA 870μm sample. The sources showing evidence for a radio counterpart are shown in red. There seems to be a preference towards sources lying in less noisy regions displaying a radio counterpart.

seems to be confirmed quite clearly by Fig. 3.12, where we can see that almost all radio counterparts are found for those submm sources lying in regions where noise is below 0.5mJy. In fact, for the low noise (<0.5 mJy) sources, the counterpart identification rate rises to 45%, which is completely compatible with Chapman et al. (2003) and Barger, Cowie & Wang (2007). On the other hand, the rate for sources lying in noisy regions (>0.5 mJy/beam) is just 10%.

This may suggest confirms that sources lying on the edge of the ALMA pointing should be treated with more care.

3.5.4 HAEs counterpart matching

Young stars emit radiation that can ionise the surrounding gas. Hydrogen recombination leads to H_α emission (rest frame λ=656 nm), which is known to be a great indicator for unobscured star formation, lying in the optical range (Kennicutt 1998). This means that a submm emission showing evidence of being correlated with an HAE can be considered a DSFG (Dannerbauer et al. 2014). We assume we can detect this line at the redshift of the Spiderweb galaxy with a narrow band filter: indeed, Koyama et al. (2013) and Shimakawa et al. (2018) were able to detect the redshifted H_α line in the Spiderweb field (z=2.2), meaning at a wavelength of $\lambda \approx 2.1 \mu m$. Both these works provided a catalogue of HAEs, even though they do not have full coverage of the LABOCA Spiderweb field as reported in Dannerbauer et al. (2014) (30/41 for Koyama and 24/41 for Shimakawa).

The counterpart matching identification rates are 27% for the Koyama et al. (2013) catalogue and 21% for the Shimakawa et al. (2018) catalogue. Dannerbauer et al. (2014) suggested a higher fraction (seven out of eleven LABOCA detections are claimed to have HAE counterparts). However, we should point out that single-dish surveys like the ones carried out with LABOCA tend to comprise blended sources, so this could explain the slightly higher fraction. As a further reference, Zhang et al. (2022) single-dish analysis report 10 secure HAEs counterparts from a population of 97 SMGs detected in two massive protoclusters at z=2.24, BOSS1244 and BOSS1542.

Chapter 4

Number counts

Number counts are a useful tool to evaluate the number density in a given field for a population of astronomical objects. Figure 4.1 reports the flux histogram for the different weighting schemes and taperings, using the best flux estimate, meaning the peak flux for unresolved sources and integrated flux for resolved ones. Each bin represents the number of sources counted in each flux interval. We immediately point out that our counts for sources with flux density <1mJy could be underestimated, since we are using a conservative detection threshold of 5σ, and the maps with the lowest noise have an rms of about 0.2 mJy.

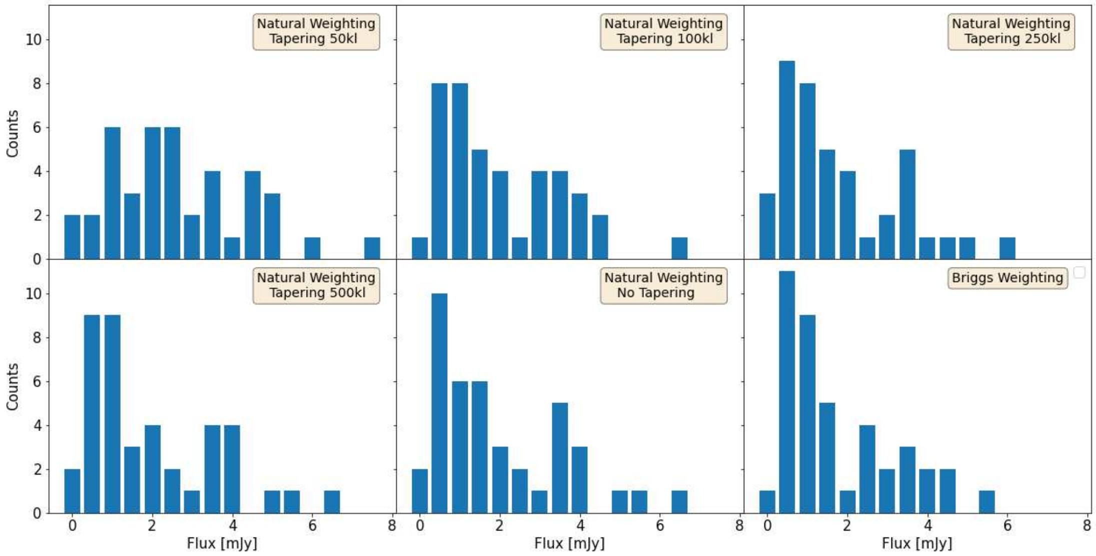

Figure 4.1: Raw counts of ALMA sources per unit flux, in all the different cleanings.

Dividing the counts by the width of the bin and by the total observed area yields the differential number counts $[mJy^{-1}deg^{-2}]$. Summing the raw counts for fluxes above a certain threshold and dividing by the observed area produces the cumulative number counts $[deg^{-2}]$. We point out that differential and cumulative number counts should provide the same physical information, but there may be discrepancies between the two: in fact, differential number counts are more sensitive to Poissonian errors, or shot noise, in the counting of sources per each bin (Franco et al. 2018). Cumulative counts are less sensitive to this effect, as they include sources going from a lower flux limit up.

The width of the bins can be chosen according to the needs of the analysis. Wide bins ensure proper population of the bin, but the covered flux range is poorly sampled. On the other hand, narrow bins probe the flux range nicely, but may be strongly affected by random deviations and suffer from large errorbars. We select 1mJy-wide intervals, meaning linearly equally spaced flux bins (like in Simpson et al. 2015, Stach et al. 2018).

We hereby present ALMA 870 μm number counts and compare them with other ALMA surveys. For the discussion of the number counts we make use of the best flux estimate for the source, meaning peak flux for point-like sources and integrated flux for resolved ones.

4.1 Number counts in literature

We now briefly discuss the papers taken as main reference in this work. We mainly used papers that come from interferometric surveys, as we can perform a direct comparison, but even two references based on single-dish surveys were also included. We summarize the main properties (flux sensitivity and spatial resolution) of the papers used here as a reference in Table 4.1.

Karim et al. (2013) report the counts of SMGs in the 870 um band observed by ALMA and previously detected by LABOCA in the LABOCA Extended Chandra Deep Field South Sub-millimeter Survey (LESS). It is proven that such counts broadly agree with previous single-dish counts. Differential number counts are fitted with a broken power-law. Simpson et al. (2015) provide continuum 870 μm ALMA maps from the UKIDSS survey, drawn from S2CLS, and analyses number counts, modelled with a broken power-law and compared with other blank fields, including Karim et al. (2013) broken powerlaw, and Weiß et al. (2009), finding a good agreement. Oteo et al. (2016) report ALMA number counts of DSFGs at 870 um and 1.2mm (rescaled), only cumulative. For flux conversion, we used the empirical flux ratios reported in Franco et al. (2018), meaning $S_{1.1mm}/S_{870\mu m} = 0.56$ and $S_{1.1mm}/S_{1.2mm} = 1.29$. Stach et al. (2018) provide the results from AS2UDS, an 870um continuum Survey with ALMA, of sources drawn from S2CLS. Both differential and cumulative number counts are provided. These are compared with Geach et al. (2016), as well as Karim et al. (2013) and Hill et al. (2018), and fitted with broken powerlaws. Franco et al. (2018) presents an ALMA Survey at 1.1 mm, called GOODS ALMA, extracted from the optical GOODS-South field. Both differential and cumulative number counts are available, the former fitted with a Schechter function, the latter with a broken powerlaw. Hatsukade et al. (2018) reports number counts from the ALMA survey of GOODS-S at 1.1mm (ASAGAO). ASAGAO is a deep field for a 250 kλ-tapered map with beamsize 0.51”x0.45”.

Survey	λ	type	size	θ	σ [mJy/b]	Reference
LESS	870μm	P	-	0.3"	0.4	Karim et al. (2013)
S2CLS	870μm	P	-	0.8"	0.26	Simpson et al. (2015)
GOODS-S	1.1mm	M	$69'^2$	0.6"	0.18	Franco et al. (2018)
SSA22 field	1.1mm	M	2'x3'	0.7"	0.06	Umehata et al. (2017)
ALMACAL	870μm	M	$19'^2$	0.5"	0.03	Oteo et al. (2016)
S2CLS	870μm	M	$50'^2$	0.15"	0.25	Stach et al. (2018)
GOODS-S	1.2mm	M	$26'^2$	0.5"	0.06	Hatsukade et al. (2018)
ECDFS	870μm	M	$5\circ^2$	19"	1.25	Weiß et al. (2009)
S2CLS	850μm	M	30'x30'	15"	1.2	Geach et al. (2016)

Table 4.1: We report the observing frequency, indicative angular resolution and flux sensitivity of our main references for the number counts treatment. The "type" of the survey specifies whether the work is based on a wide flux map (M) or just follow-up pointings on pre-selected sources (P). In case a whole survey map is presented, its size is also given. Above the double line we have interferometric ALMA surveys, below that we find single-dish surveys, from LABOCA and SCUBA-2 respectively.

Finally, we used the survey presented in Umehata et al. (2017), investigating the SSA22 field at 1.1mm. Umehata et al. (2017) report a protocluster at z=3.09, which shows a possible excess of differential and cumulative number counts with respect to the blank fields. The authors carry out a comparison with the blank field counts by Karim et al. (2013), Oteo et al. (2016), Simpson et al. (2015) and provide evidence for an overdensity. For this reason, this paper can guide us through recognizing the overdensity in the Spiderweb protocluster too.

We should mention the role of the FoV of the instrument in computing number counts. Fovs larger than a few square degrees may suffer less from cosmic variance uncertainty and affect number counts. This is because SMGs are thought to be a tracer of the underlying matter field (Hickox & LESS Collaboration 2012, Chen et al. 2016), thus the variance that we should associate to the counts should be given by shot noise but also cosmic variance. In the case of narrow FoVs (like ALMA), the latter prevails.

As far as single-dish surveys are concerned, we studied the work by Geach et al. (2016), which is based on the S2CLS (Scuba-2 Cosmology Legacy Survey), the biggest survey of its kind ($\approx 5°$), at 850 μm and serves as a blank field. It provides both differential and cumulative number counts, fitted with a Schechter function and an integrated Schecther function, respectively. A 15-20% increase of the observed counts on the scales of the GOODS-N field is reported. The analysis carried out in Weiß et al. (2009) is also based on a single-dish survey on the Extended Chandra Deep Field South (ECDFS) observed with LABOCA on the APEX telescope. Despite the source confusion that affects the flux maps, the differential source counts in the full field are well described by a power law that matches the results from other fields.

4.2 ALMA number counts

In this section we introduce the number counts associated to the ALMA detections of the Spiderweb protocluster field and present the proper comparisons with literature. We point out that redshift has a key role in evaluating the number counts of the field: in order to have a reliable overdensity, we need to determine the membership of our ALMA sources to the protocluster. To do that, ideally we would need spectroscopic redshift, for example from emission lines. Lacking spectroscopic information, one can also use photometric redshifts. However, in this work we did not estimate redshift of the sources. Further development of the project shall include redshift determination, either spectroscopically or with photometry.

When computing number counts, we use the LABOCA map area, making the implicit assumption that where LABOCA did not detect sources, there are none. We also keep in mind that Dannerbauer et al. (2014) found evidence of an overdensity of a factor at least 2 with respect to the reference blank field (Weiß et al. 2009) in the 56 $arcmin^2$ region observed by LABOCA where the noise is <1.9mJy/beam, where 14 of the 16 originally detected LABOCA sources are found (Fig. 1.6). We should point out that for 2 of them (DKB13 and DKB14) Dannerbauer et al. (2014) computed a FIR photometric redshift which is incompatible with Spiderweb. In the pointings of DKB13 and DKB14 we found multiple ALMA sources (3 and 2 respectively), so at least one of the sources would probably produce a photometric redshift incompatible with z=2.16. However, all the ALMA sources will need to be assigned their own redshift measurement. At this stage, we include the sources anyway, knowing that further development of the work will need to include an exhaustive analysis of redshift.

Moreover, a separate evaluation of the number density was carried out in the very core of the protocluster field, in a 4' diameter (2 Mpc at this redshift) region encompassing 6 of the sources of the LABOCA catalogue (DKB01, DKB02, DKB03, DKB05, DKB07, DKB12, DKB16) whose membership was confirmed either by spectroscopic or FIR photmetric redshift (Figure 1.7).

We carry out our analysis in the same two subregions of the LABOCA map, using our ALMA detections instead. We should clarify that we are using ALMA single pointings around LABOCA-selected sources, without observing the rest of the field explored by the bolometer. We thus carry out the number counts analysis using our ALMA follow-up catalogue but referring to the whole field. This treatment also requires a correction factor for the total area, adjusting for the fact that we did not target all the LABOCA sources (Karim et al. 2013). This correction is presented in Equation 4.1, in which the effective ALMA area is given by the single-dish observed area, multiplied by the ratio between the number of sources with an interferometric followup and the total number of single-dish detected sources.

$$A_{ALMA} = \frac{N_{maps}(ALMA)}{N_{sources}(LABOCA)} \cdot A_{LABOCA} \tag{4.1}$$

Differential and cumulative number counts for the two different areas are pre-

S	N_d	dN/dS_2 $10^2(mJy^{-1}deg^{-2})$	N_c	N_2(>S) $10^2(deg^{-2})$	N_d	dN/dS_2 $10^2(mJy^{-1}deg^{-2})$	N_c	N_2(>S) $10^2(deg^{-2})$
0.5	9	7.4±2.5	34	27.8±4.8	7	26.8±10.1	25	95.5±19.1
1.5	10	8.2±2.6	25	20.5±4.1	7	26.8±10.1	18	68.8±16.2
2.5	5	4.1±1.8	15	12.3±3.2	3	11.5±6.6	11	42.0±12.7
3.5	7	5.7±2.2	10	8.2±2.6	7	26.7±10.1	8	30.6±10.8
4.5	2	1.6±1.2	3	2.5±1.4	0	-	1	3.8±3.8
5.5	0	-	1	0.8±0.8	0	-	1	3.8±3.8
6.5	1	0.8±0.8	1	0.8±0.8	1	3.8±3.8	0	3.8±3.8

Table 4.2: ALMA 870 μm differential and cumulative number counts are reported for 100kλ-tapered maps. Column 1 (S) shows the center of the flux bin, columns 2 and 3 (N_d and dN/dS) report the counts per bin and the differential counts, while columns 4 and 5 (N_c and N(>S)) report cumulative raw counts and cumulative counts per unit area. The left table represents the subregion with area $56 arcmin^2$, while the right table reports the counts for the innermost region of $13 arcmin^2$.

sented in Table 4.2. We show the counts derived from natural weighting, 100kλ tapered maps as an example.

We start by discussing the wider, $56 arcmin^2$ area, which includes all LABOCA sources but DKB08 and DKB10. Of the 14 LABOCA sources, three were not targeted by this ALMA program, as previously mentioned, leaving us with 11 ALMA follow-ups out of 14 bolometric sources. According to equation 4.1, we need to apply a correction factor of 11/14 to the $56 arcmin^2$ surface. Figures 4.2 and 4.3 show the counts represented in the different cleanings. Differential number counts represented in Fig. 4.2 does not seem to show evidence for an overdensity. On the contrary, we see underdensity in the low flux bins counts, when compared to literature works that investigate the same flux regime (Hatsukade et al. 2018, Franco et al. 2018). In fact, we note that our points flatten instead of following the increasing steepness of the distribution when moving towards lower fluxes. However, we know that at this flux (<1mJy) we are at the edge of our detection limit, while Franco et al. (2018) and Hatsukade et al. (2018) present deeper ALMA surveys: the former detect sources brighter than 0.7 mJy at 1.1mm, the latter reach flux sensitivities of 60μJy/beam at 1.2mm.

Moreover, we know that our sample is affected by incompleteness and boosting. In particular, completeness corrections are necessary when going to such low fluxes: according to the simulations performed by Franco et al. (2018) based on the depth of their measurements, a sample of sources with flux density $\lesssim$1 mJy and of size $\approx$ 0.3" is only $\approx$30% complete. This fraction will be even lower with the poorer sensitivity of our ALMA catalogue. Finally, we note that the correction we applied to get the effective area (Equation 4.1) is correct in the flux range covered by LABOCA (>3mJy). Below such limit, the number counts derived from our ALMA maps should be considered biased since the observations were taken in the vicinity of a bright sub-millimetre source, so they may be under-representative of the dim end of the population (Karim et al. 2013).

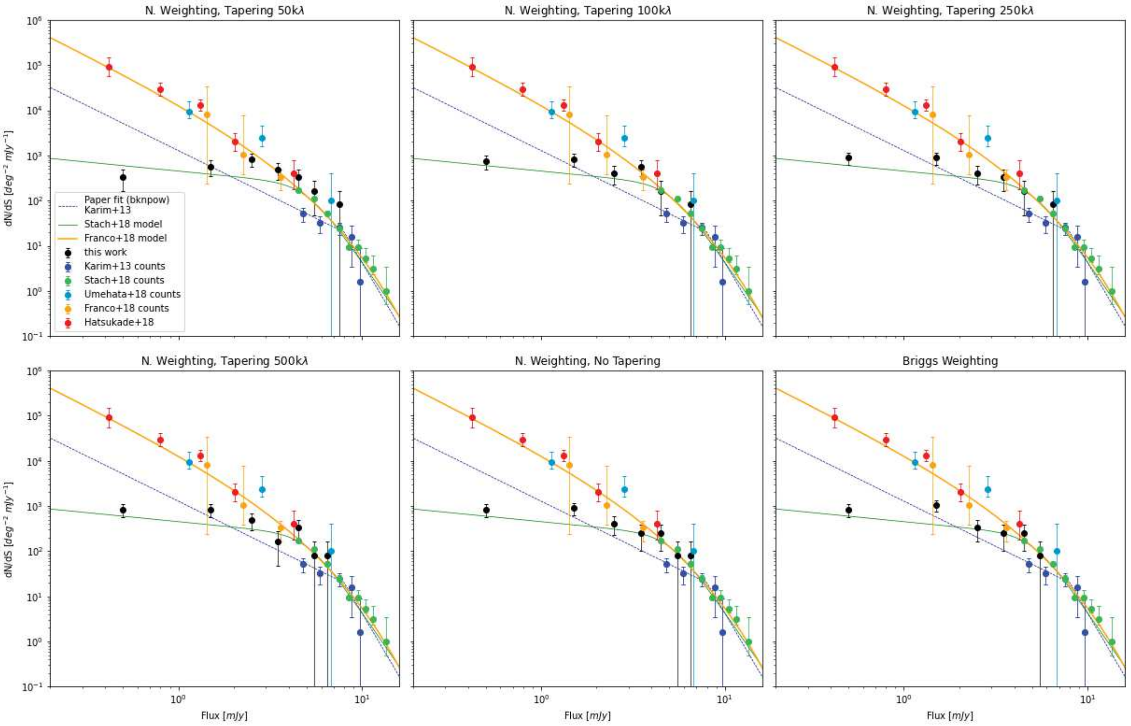

Figure 4.2: Differential number counts (black dots) within $56 arcmin^2$ region in the different cleanings.

Regarding the higher flux bins (>1mJy) we enter the regime where ALMA comfortably detects sources at 5σ and the counts agree with previous interferometric surveys of blank fields. The highest-flux bin (7-8 mJy) lies slightly above the blank fields (an overdensity factor of about 1.5), and matches with the count reported by Umehata et al. (2017) (cyan dots), who reported the counts in the core of a well-studied protocluster at z=3.09 in the SSA22 field. This match is more evident in the three top panels, where we have the heavy-medium taperings and thus flux should be better recovered and protected from the missing flux issue.

Clues for overdensity can be instead observed in the cumulative number counts (Figure 4.3). Cumulative number counts are less sensitive to undercounting of single bins, so they should be less affected by completeness and less affected by our ALMA detection limit. Except for the faintest flux bin, which is still underdense, the other counts lie globally above the models of blank field surveys. For sources with flux densities >2mJy, where the issue of completeness and detection should be significantly reduced, we report a number density $N(> 2mJy) = 0.34 arcmin^{-2}$, which is ≈2.6 times larger than predicted by the blank field survey analysed by Simpson et al. (2015), who report a number density of $0.13 arcmin^{-2}$ at this flux. This is compatible with the overdensity factor reported by Dannerbauer et al. (2014), who claimed that the overdensity ratio of the LABOCA sources in this region were above the single-dish bland field survey of Weiß et al. (2009) of a factor between 2 and 4.

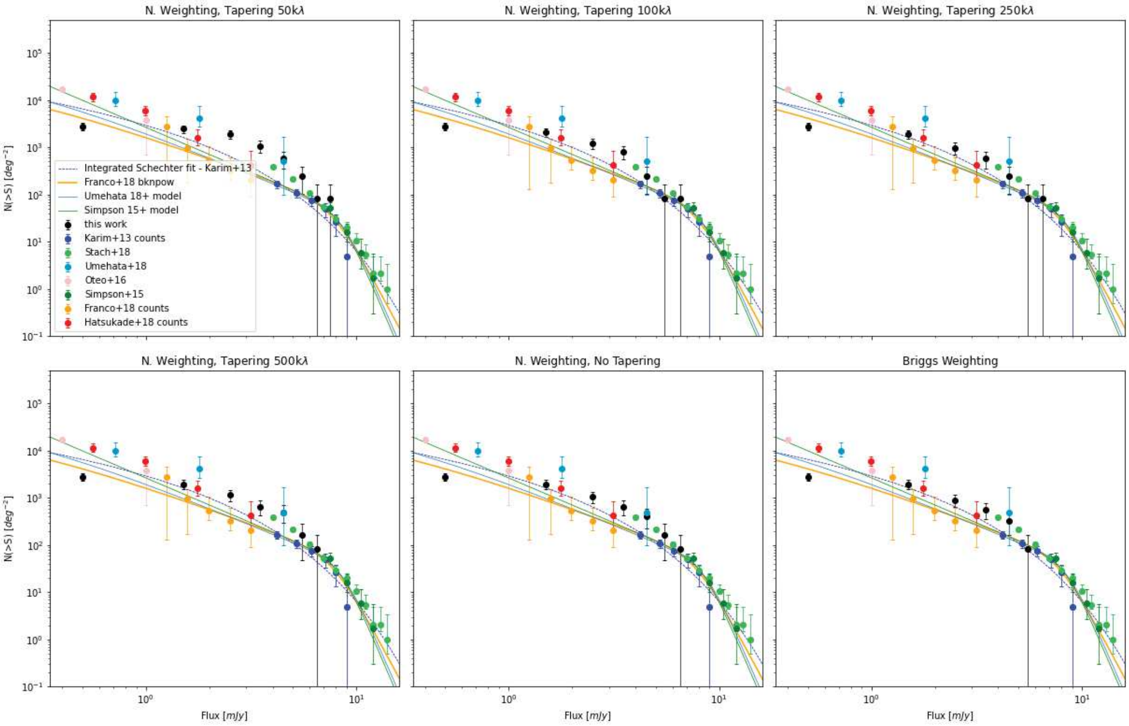

Figure 4.3: Cumulative number counts (black dots) within $56arcmin^2$ region in the different cleanings.

Moreover, for the heaviest taperings (50 and 100 kλ), our counts match with the z=3 protocluster overdensity levels reported by Umehata et al. 2017.

To better constrain the overdensity factor, we can move to the core of the Spiderweb protocluster and focus on a ≈4' diameter region where 50% of the LABOCA observations are concentrated. Dannerbauer et al. (2014) reported an overdensity factor two times higher than the one given for the larger region. We carry out a number counts analysis for this subregion, using again equation 4.1 to get an effective area through a correction factor of 6/8. Figures 4.4 and 4.5 display the differential and cumulative number counts carried out in this narrower region, always considering the different cleanings and taperings in the panels. In this case, the evidence for overdensity is much more clear. We can see again the completeness and flux limit issues, that affect primarily differential number counts (Fig.4.4). In this figure, we observe that all the differential counts above 2mJy lie comfortably above the interferometric models at all resolutions, and also slightly above the protocluster counts by Umehata et al. (2017).

The situation is more clear in cumulative number counts, as they are less affected by completeness. The counts lie above the reference blank field surveys and above the z=3 protocluster counts, even suggesting the presence of a denser protocluster. Considering the area of the very core, we get a number density of $N(S > 2mJy) = 1.2arcmin^2$, which is ≈9 times the value predicted by Simpson et al. (2015). This would confirm the hypothesis proposed by Dan-

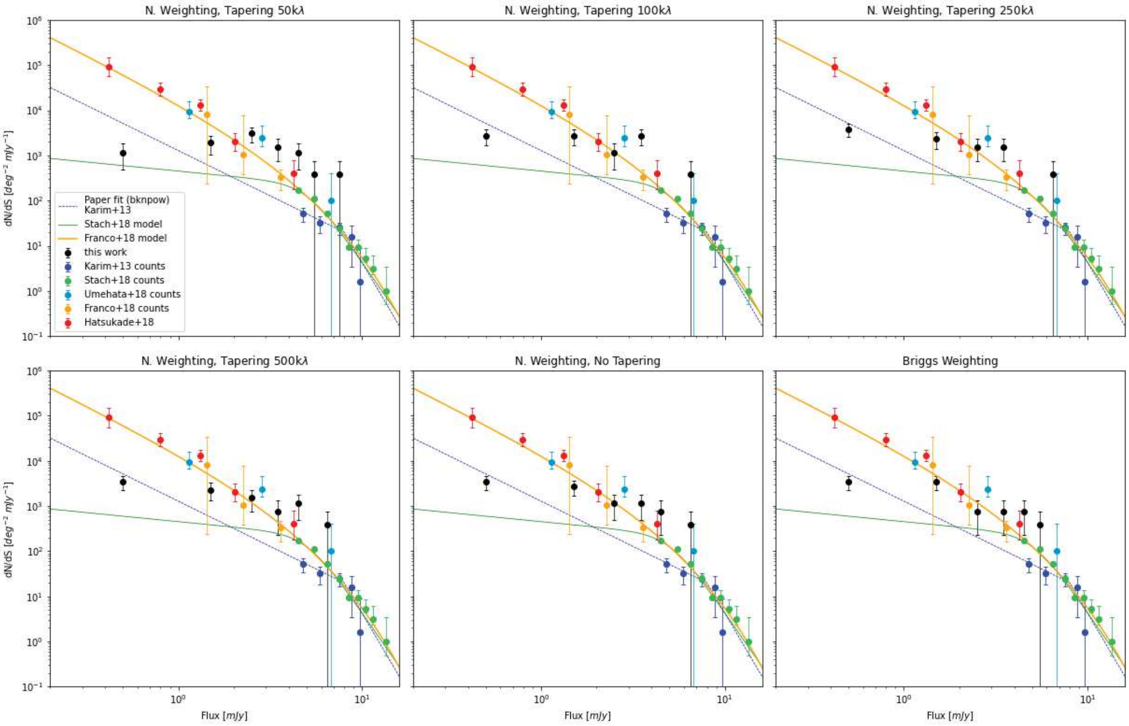

Figure 4.4: Differential number counts (black dots) within $13 arcmin^2$ region in the different cleanings.

nerbauer et al. (2014) and validate the protocluster nature of the Spiderweb field.

We also add that that removing the sources labelled with quality flag "3", that are considered as tentative, has a negligible impact on the number counts. In fact, these sources all belong to the lower flux bins, that we do not consider reliable in our analysis due to completeness and our ALMA flux limit. Moreover, we point out that of the 34 ALMA sources included in the $56 arcmin^2$ subregion, 5 are sub-detections of DKB13 and DKB14, whose photometric redshift is incompatible with Spiderweb according to Dannerbauer et al. (2014). At least one of the ALMA detections per each pointing will have a redshift incompatible with Spiderweb, maybe more than that. This means that a redshift estimation would rule them out, making our counts slightly overestimated.

We also add a comparison between our ALMA protocluster core counts and single-dish blank field surveys, to highlight the importance of not mixing light-heartedly source counts coming from interferometric surveys and single dish instruments. Figures 4.6 and 4.7 show the number counts computed in the smaller $13 arcmin^2$ area in comparison with the single-dish surveys Weiß et al. (2009) and Geach et al. (2016). Our interferometric counts still lie above the single-dish models and show evidence of overdensity, even though it is less marked. It is in fact documented that single-dish surveys tend to overestimate source counts and up-scatter the distribution of bright source (Karim et al. 2013, Simpson et al. 2015, Franco et al. 2018). This is mostly due to source

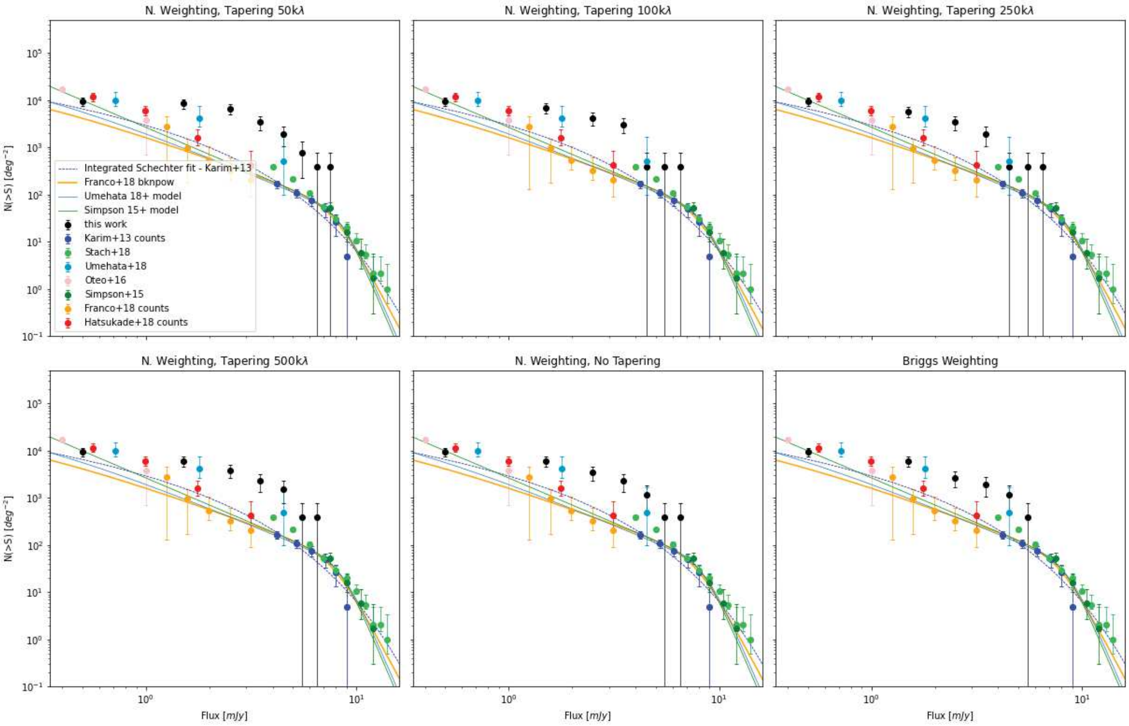

Figure 4.5: Cumulative number counts (black dots) within $13arcmin^2$ region in the different cleanings.

blending, that causes multiple faint sources to be mistaken as single bright sources, as detections in single-dish surveys are convolved into larger beams.

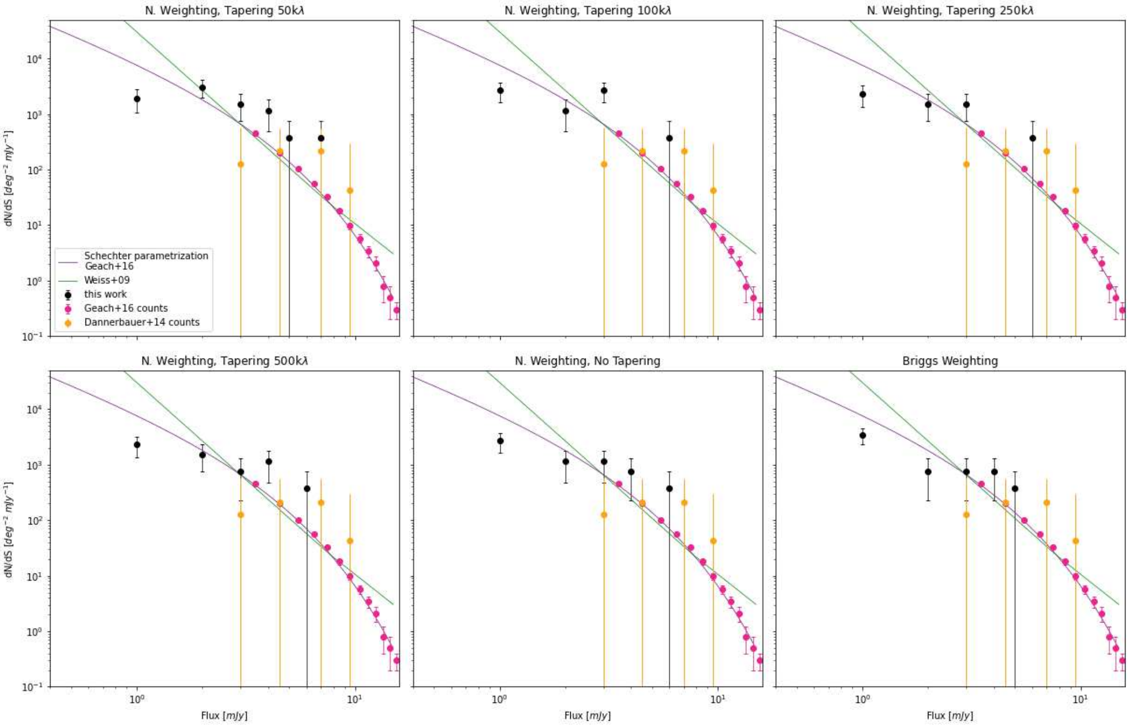

Figure 4.6: ALMA 870μm differential number counts ((black dots)) compared to single-dish surveys.

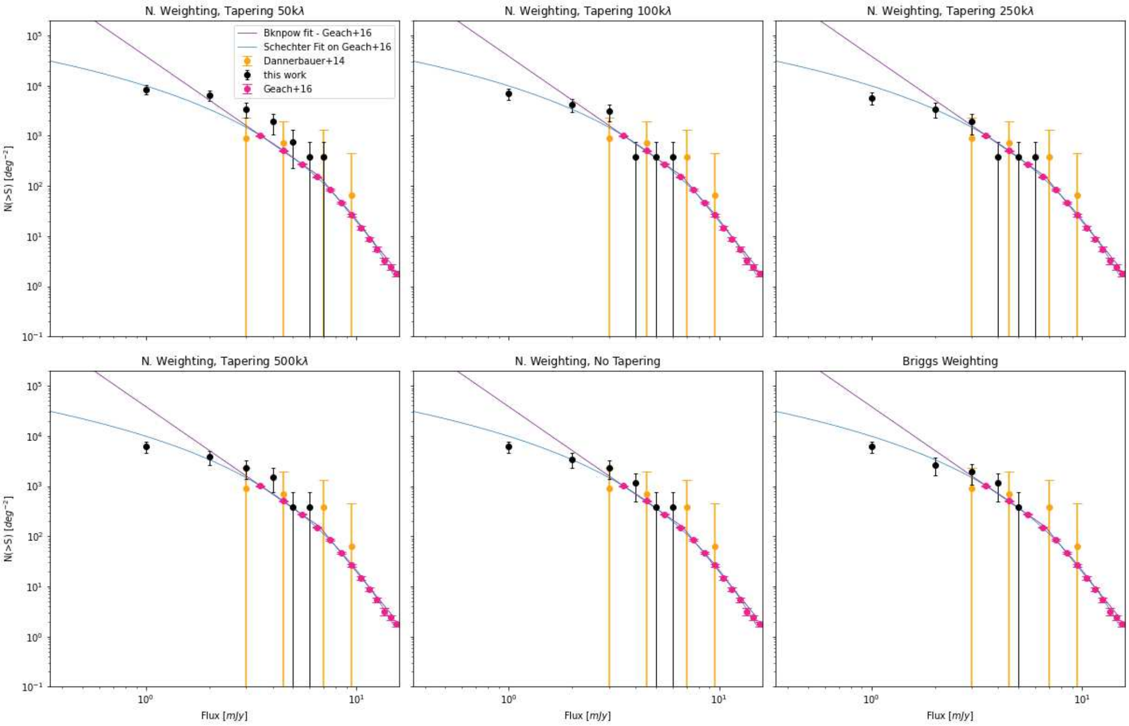

Figure 4.7: ALMA 870μm cumulative number counts (black dots) compared to single-dish surveys.

Chapter 5

Discussion and Outlook

We have presented 870μm ALMA follow-up photometry of 13 LABOCA sources, selected from a wide, 140 $arcmin^2$ field centred on the HzRG MRC1138-262 (Spiderweb) and considered to host a protocluster structure based on the SMGs source counts (Dannerbauer et al. 2014). We observed 13 of the 16 LABOCA sources reported by Dannerbauer et al. (2014) with ALMA and produced 870 μm dust continuum flux maps. These maps bring relevant insights for this field, thanks to a beamsize down to 0.3" and a flux sensitivity down to ≈0.17 mJy. The ALMA dataset are CLEANed with 6 different weighting and tapering methods.

Detections and multiplicity In the 13 ALMA 870μm pointings, we detect 41 ALMA sources, 34 achieving 5σ significance in at least 3 out of 6 weighting configurations, and 7 achieving 3σ detection but having evidence for counterparts. This unveiled the multiplicity of the LABOCA detections. Literature provides abundant evidence of at least a fraction of bright SMGs being blends of multiple fainter sub-mm emissions (Karim et al. 2013, Hodge et al. 2013, Simpson et al. 2015, Stach et al. 2018, Hill et al. 2018, Cairns et al. 2022): this work confirms and goes beyond this trend, revealing a notably high multiplicity. In fact, on average 3.7 ALMA sources are revealed per each single-dish detection, which is a high number with respect to the average multiplicity level reported by the works above, which is around 2-3. Our high multiplicity could be due to an intrinsic richness of sources of the field, which is considered to be a protocluster (Dannerbauer et al. 2014).

Counterpart analysis We set up a counterpart analysis exploiting the exquisite multiwavelength data available for the MRC1138-262 field. We report counterpart identification rates with a matching radius equal to the beamsize of each instrument. We found a NIR matching rate between 30 and 47%, considering HST/NICMOS, Subaru/MOIRCS and VLT/HAWK-I and ISAAC probing the wavelength range between 1.1μm and 2.1μm. We also found that about 40% of all ALMA sources have a counterpart in at least one of the bands of PACS or SPIRE (FIR).

These rates imply that there is a consistent fraction of our sources that are obscured at optical and NIR wavelengths, and that are only visible in the sub-mm regime, because they are covered in dust. This was already foreseen by the high SFR that we found for the field. This is an important result, showing that classical optical surveys based on the UV-optical-NIR systematically miss a fraction of star forming galaxies that may be significantly contributing to the star formation rate density of the Universe. The existence of such objects is also addressed by Franco et al. (2018) and Gruppioni et al. (2020), that study the so-called "HST-dark" galaxies, meaning dusty galaxies not visible at UV-optical-NIR wavelengths.

This would impact our current knowledge about the amount of star formation, which is based on unobscured stellar emission, represented by the plot we showed in the Introduction (Fig.1.5, Madau & Dickinson 2014). Future perspectives on this topic include adding obscured SMG contribution to the state-of-the-art modelling of star formation rate.

We used radio counterpart matching for some diagnostics plots. We found that fainter sources are less likely to reveal radio counterparts, due to the radio to sub-mm flux correlation. From the analysis of the counterpart rate with respect to the noise associated to our sources, we found that radio matches are mostly associated to low-noise regions. This suggest that we should treat with care ALMA sources detected outside the primary beam, where the noise pattern increases rapidly.

Flux measurements We measure the flux of the sources both using peak flux and integrated flux within a fixed aperture. We notice that in some cases integrated flux is higher than peak flux, suggesting that we may be dealing with resolved sources. Thus, we take the peak flux as the best flux estimate for the unresolved sources and integrated flux for the resolved ones. We witness that peak flux and integrated flux are a function of the beamsize: as the beamsize increases, the peak flux grows, better recovering resolved emission with larger beamsizes, while integrated flux decreases. In fact, peak flux is an inefficient flux estimate with narrow beams, that do not recover extended emission: in these cases we need to use integrated flux. At the tapering where integrated flux is maximised, the beamsize provides an indication of the size of the source. Most sources have sizes between 0.3" and 0.5", consistently with what literature predicts for optical galaxies at this redshift (van der Wel et al. 2014).

Moreover, we compare the flux we recovered from the ALMA sources within the same pointing with the original LABOCA flux. We observed that high-resolution settings cause a flux loss (about 20%), as predicted by "missing flux" problem, renown but poorly addressed in literature (Braun & Walterbos 1985, Faridani et al. 2017). We conclude that LABOCA flux is best recovered with heavier tapering, that allows to collect extended emission. We also noticed that natural weighting and 100 kλ tapering seem to offer the best S_{ALMA}/S_{LABOCA} ratio (equal to 0.99±0.05) among the available taperings.

Flux measurements also allow to estimate two key parameters to characterize the field: Star Formation Rate (SFR) and Infrared Luminosity (L_{IR}).

In order to compute L_{IR} and SFR, we follow the empirical formulas indicated by Kennicutt (1998).

$$L_{FIR} = 2.1 \cdot 10^{12} \frac{S_{1.2mm}}{mJy} L_{\odot} \tag{5.1}$$

$$SFR = \frac{L_{FIR}}{5.8 \cdot 10^{9}} M_{\odot}/yr \tag{5.2}$$

However, flux measurements in this work are carried out in a different band. Therefore we make use of empirical flux ratios reported in Franco et al. (2018): $S_{1.1mm}/S_{870\mu m} = 0.56$ and $S_{1.1mm}/S_{1.2mm} = 1.29$. Therefore, we can infer the 1.2mm flux basing on our ALMA measured-flux. Doing so, we can rescale equation 5.1 into

$$L_{FIR} = 9.1 \cdot 10^{11} \frac{S_{870\mu m}}{mJy} L_{\odot} \tag{5.3}$$

We can thus derive the total IR luminosity, using the total flux of all the sources recovered by ALMA. After the conclusions suggested in the previous section, we use 100kλ tapered flux as we claim it to be the best at recovering flux amongst those available. $S^{tot}_{100k\lambda} = 103.1 \pm 6.6$ mJy, and thus, using equation 5.3, we get $L^{tot}_{IR} = (9.4 \pm 0.6) \cdot 10^{13} L_{\odot}$. This is the overall infrared luminosity of the observed ALMA sources. From this, we can compute the overall SFR associated to the field, that is $SFR = (1.6 \pm 0.1) \cdot 10^{4} M_{\odot}/yr$. Moreover, assuming a sphere of 4 Mpc diameter, we also get a star formation rate density $SFRD = (1290 \pm 103)\ M_{\odot}yr^{-1}Mpc^{-3}$ in physical volume. This value is consistent within 2σ with the reference value given by Dannerbauer et al. (2014). This result is reasonable, as we showed that the LABOCA flux used in such paper is overall recovered.

However, to provide a direct comparison with Star Formation History plots in Madau & Dickinson (2014), we introduce the SFRD in the co-moving volume by dividing by a factor $(1+z)^3$. This leads to a $SFRD = (41 \pm 3) M_{\odot}yr^{-1}cMpc^{-3}$ in co-moving volume, compatible with the estimate for this field given by Jin et al. (2021). This SFRD is higher ≈2.5 orders of magnitude above the reported cosmic SFRD in random fields (Madau & Dickinson 2014).

Such high comoving SFRD shows that we are dealing with a rather extreme population of objects, that currently do not fit well within the models for optical star formation. These results show that obscured star formation could account for a significant fraction of the global star formation activity of the Universe at high redshift.

Number counts We construct differential and cumulative number counts of the SMGs detected by ALMA. We compare the counts derived from our dataset to blank-field surveys (Karim et al. 2013, Simpson et al. 2015, Oteo et al. 2016, Franco et al. 2018, Stach et al. 2018, Hatsukade et al. 2018) and also to another protocluster field (Umehata et al. 2017). We find weak evidence for overdensity in the cumulative number counts for sources lying within the $56 arcmin^2$ map selected by Dannerbauer et al. (2014) and with flux >2mJy (a factor approximately 2.6 higher than blank field references). Moreover, the inner, 4' diameter circular region of the protocluster reveals a very clear overdensity, visible both in the differential and the cumulative number counts. Here, the ratio with respect to the blank field surveys reaches a factor ≈9 for sources brighter than 2 mJy. These results point in the direction of the Spiderweb field being a protocluster field: in the narrower region we are sampling the very core and obtain a prominent excess with respect to blank field surveys, while in the wider region we include the outskirts of the structure and our counts are lower.

These results are also important in the context of the search for protoclusters: literature suggested that SMGs are signposts of overdensities in the early Universe (Stevens et al. 2003, De Breuck et al. 2004, Greve et al. 2007, Priddey, Ivison & Isaak 2008, Stevens et al. 2010, Carrera et al. 2011, Rigby et al. 2013), where optical surveys cannot reach. Our work also reinforces the idea that SMGs are excellent tracers of protoclusters at high redshift, and are thus an excellent target to explore models for galaxy and cluster formation and evolution.

Outlook In a future refinement of this work, measured flux should be deboosted to account for Eddington effect. We also point out that flux analysis may need completeness correction in the source detection analysis, that can possibly be applied through Montecarlo simulations. This would also result in an improvement of number counts of sources belonging to the dim end of the distribution.

Evaluating the redshifts of the ALMA sources spectroscopically would also be a significant improvement of the work, allowing to confirm the protocluster membership of the sources in the catalogue. To do this, we could study emission lines in the FIR (like CO) or in the optical, which is however less feasible since we would be pointing at dust-obscured objects. A CO catalogue on this field is available in Jin et al. (2021) and could be used in the future to confirm membership to the cluster and also infer the physical properties of the sources.

Multiwavelength analysis can also be improved with more refined p-statistics instead of a rigid matching radius method. Moreover, adding flux measurements in the other bands we would be able to build complete SEDs, ranging from UV to FIR and sub-mm. This would help us estimating photometric redshifts, but also stellar masses and SFR.

The softwares used for photometric analysis at this stage include CASA, CARTA and SAOImageDS9, to view flux maps and create region files, TOPCAT, and Python scripts for source detection and to perform flux measurements.

Bibliography

Barger, A. J., L. L. Cowie, A. H. Blair, et al. (2022), *Apj* 934, 56.

Barger, A. J., L. L. Cowie & W. H. Wang (2007), *ApJ* 654, 764–781.

Baugh, C. M., C. G. Lacey, C. S. Frenk, et al. (2005), *MNRAS* 356, 1191–1200.

Bennett, C. L., D. Larson, J. L. Weiland, et al. (2013), *ApJs* 208, 20.

Béthermin, M., Y. Fudamoto, M. Ginolfi, et al. (2020), *AAP* 643, A2.

Biggs, A. D., R. J. Ivison, E. Ibar, et al. (2011), *MNRAS* 413, 2314–2338.

Blain, A. W. & M. S. Longair (1993), *MNRAS* 264, 509–521.

Blain, Andrew W., Ian Smail, R. J. Ivison, et al. (2002), *Phys. Rep.* 369, 111–176.

Bower, Richard G. & Michael L. Balogh (2004), *Clusters of Galaxies: Probes of Cosmological Structure and Galaxy Evolution* 3, 325.

Braun, R. & R. A. M. Walterbos (1985), *AAP* 143, 307–312.

Cairns, J., D. L. Clements, J. Greenslade, et al. (2022), *arXiv e-prints*.

Calzetti, Daniela, Lee Armus, Ralph C. Bohlin, et al. (2000), *ApJ* 533, 682–695.

Carilli, C. L. & F. Walter (2013), *ARAA* 51, 105–161.

Carrera, Francisco, M. Page, JA Stevens, et al. (2011), *MNRAS* 413, 2791 –2807.

Casey, Caitlin M. (2012), *MNRAS* 425, 3094–3103.

Casey, Caitlin M., Desika Narayanan & Asantha Cooray (2014), *Phys. Rep.* 541, 45–161.

Cassata, Paolo, Daizhong Liu, Brent Groves, et al. (2020), *ApJ* 891, 83.

Chapman, S. C., A. J. Barger, L. L. Cowie, et al. (2003), *ApJ* 585, 57–66.

Chen, Chian-Chou, Ian Smail, Rob J. Ivison, et al. (2016), *ApJ* 820, 82.

Crill, B. P., P. A. R. Ade, D. R. Artusa, et al. (2003), *ApJs* 148, 527–541.

Daddi, E., H. Dannerbauer, D. Stern, et al. (2009), *ApJ* 694, 1517–1538.

Dannerbauer, H., E. Daddi, G. E. Morrison, et al. (2010), *ApJl* 720, L144–L148.

Dannerbauer, H., J. D. Kurk, C. De Breuck, et al. (2014), *A&A* 570, A55.

Dannerbauer, H., M. D. Lehnert, B. Emonts, et al. (2017), *AAP* 608, A48.

Dannerbauer, H., M. D. Lehnert, D. Lutz, et al. (July 2002), *ApJ* 573, 473–484.

Dannerbauer, H., M. D. Lehnert, D. Lutz, et al. (2004), *ApJ* 606, 664–682.

De Breuck, C., F. Bertoldi, C. Carilli, et al. (2004), *AAP* 424, 1–12.

Downes, A. J. B., J. A. Peacock, A. Savage, et al. (1986), *MNRAS* 218, 31–62.

Dunlop, J. S., R. J. McLure, A. D. Biggs, et al. (2017), *MNRAS* 466, 861–883.

Faridani, Shahram, F. Bigiel, Lars Flöer, et al. (2017), *Astronomische Nachrichten* 339.

Fazio, G. G., J. L. Hora, L. E. Allen, et al. (2004), *ApJs* 154, 10–17.

Franco, M., D. Elbaz, M. Béthermin, et al. (2018), *AAP* 620, A152.

Geach, J. E., J. S. Dunlop, M. Halpern, et al. (2017), *MNRAS* 465, 1789–1806.

Geach, James E., James S. Dunlop, Mark Halpern, et al. (2016), *Zenodo*, 57792.

Genzel, Reinhard, Andrew J. Baker, Linda J. Tacconi, et al. (2003), *ApJ* 584, 633–642.

Greve, T. R., F. Bertoldi, Ian Smail, et al. (2005), *MNRAS* 359, 1165–1183.

Greve, T. R., D. Stern, R. J. Ivison, et al. (2007), *MNRAS* 382, 48–66.

Griffin, M. J., A. Abergel, A. Abreu, et al. (2010), *AAP* 518, L3.

Gruppioni, C., M. Béthermin, F. Loiacono, et al. (2020), *AAP* 643, A8.

Hatsukade, Bunyo, Kotaro Kohno, Yuki Yamaguchi, et al. (2018), *PASJ* 70, 105.

Hickox, Ryan C. & LESS Collaboration (2012), *American Astronomical Society Meeting Abstracts* 219, 416.04.

Hildebrand, R. H. (1983), *QJRAS* 24, 267–282.

Hill, Ryley, Scott C. Chapman, Douglas Scott, et al. (2018), *MNRAS* 477, 2042–2067.

Hodge, J. A., A. Karim, I. Smail, et al. (2013), *ApJ* 768, 91.

Holland, W. S., E. I. Robson, W. K. Gear, et al. (1999), *MNRAS* 303, 659–672.

Hopkins, Andrew M. & John F. Beacom (2006), *ApJ* 651, 142–154.

Hughes, David H., Stephen Serjeant, James Dunlop, et al. (1998), *NAT* 394, 241–247.

Ivison, R. J., T. R. Greve, Ian Smail, et al. (2002), *MNRAS* 337, 1–25.

Ivison, R. J., B. Magnelli, E. Ibar, et al. (2010), *AAP* 518, L31.

Jin, S., H. Dannerbauer, B. Emonts, et al. (2021), *AAP* 652, A11.

Karim, A., A. M. Swinbank, J. A. Hodge, et al. (2013), *MNRAS* 432, 2–9.

Kennicutt Robert C., Jr. (1998), *ARAA* 36, 189–232.

Kovács, A., S. C. Chapman, C. D. Dowell, et al. (2006), *ApJ* 650, 592–603.

Koyama, Yusei, Tadayuki Kodama, Ken-ichi Tadaki, et al. (2013), *MNRAS* 428, 1551–1564.

Kurk, J., B. Venemans, H. Röttgering, et al. (2004a), *Astrophysics and Space Science Library* 301, 141.

Kurk, J. D., L. Pentericci, R. A. Overzier, et al. (2004b), *AAP* 428, 817–821.

Kurk, J. D., L. Pentericci, H. J. A. Röttgering, et al. (2001), *Astrophysics and Space Science Supplement* 277, 543–546.

Lamarre, J. M., J. L. Puget, F. Bouchet, et al. (2003), "The Planck High Frequency Instrument, a third generation CMB experiment, and a full sky submillimeter survey", *NAR* 47.11-12, 1017–1024.

Madau, Piero & Mark Dickinson (2014), *ARAA* 52, 415–486.

Mather, J. C., E. S. Cheng, Jr. Eplee R. E., et al. (1990), *ApJl* 354, L37.

McMullin, J. P., B. Waters, D. Schiebel, et al. (2007), vol. 376, 127.

Morrison, Glenn E., Frazer N. Owen, Mark Dickinson, et al. (2010), *ApJs* 188, 178–186.

Murphy, Eric J. (2009), *ApJ* 706, 482–496.

Napier, P.J., A.R. Thompson & R.D. Ekers (1983), *Proceedings of the IEEE* 71, 1295–1320.

Oteo, I., R. J. Ivison, L. Dunne, et al. (2018), *ApJ* 856, 72.

Oteo, I., M. A. Zwaan, R. J. Ivison, et al. (2016), *ApJ* 822, 36.

— (2017), *ApJ* 837, 182.

Overzier, Roderik A. (2016), “The realm of the galaxy protoclusters. A review”, *AAPR* 24, 14.

Pentericci, L., J. D. Kurk, C. L. Carilli, et al. (2002), *AAP* 396, 109–115.

Pentericci, L., J. D. Kurk, H. J. A. Röttgering, et al. (2000), *AAP* 361, L25–L28.

Pentericci, L., G. K. Miley & B. P. Venemans (2007), ASPCS 380, 219.

Pilbratt, G. L., J. R. Riedinger, T. Passvogel, et al. (2010), *AAP* 518, L1.

Poglitsch, A., C. Waelkens, N. Geis, et al. (2010), *AAP* 518, L2.

Priddey, R. S., R. J. Ivison & K. G. Isaak (2008), *MNRAS* 383, 289–296.

Rigby, E. E., N. A. Hatch, H. J. A. Röttgering, et al. (2013), *MNRAS* 437, 1882–1893.

Sanders, D. B. & I. F. Mirabel (1996), *ARAA* 34, 749.

Schediwy, Sascha (2013), “A Clock for the Square Kilometre Array”, Conference Paper, 031.

Seymour, Nick, Daniel Stern, Carlos De Breuck, et al. (2007), *ApJs* 171, 353–375.

Shim, Hyunjin, Dongseob Lee, Yeonsik Kim, et al. (2022), *MNRAS* 514, 2915–2935.

Shimakawa, Rhythm, Yusei Koyama, Huub J. A. Röttgering, et al. (2018), *MNRAS* 481, 5630–5650.

Simpson, J. M., Ian Smail, A. M. Swinbank, et al. (2015), *ApJ* 807, 128.

Siringo, G., E. Kreysa, A. Kovács, et al. (2009), “The Large APEX BOlometer CAmera LABOCA”, *AAP* 497, 945–962.

Smail, Ian, R. J. Ivison & A. W. Blain (1997), *ApJl* 490, L5–L8.

Smail, Ian, R. J. Ivison, A. W. Blain, et al. (2002), *MNRAS* 331, 495–520.

Sousa, S.G., N.C. Santos, C. Israelian, et al. (2011), *A&A* 533, A141.

Spilker, Justin S., Katherine A. Suess, David J. Setton, et al. (2022), *AJl* 936, L11.

Stach, Stuart M., U. Dudzevičiūtė, Ian Smail, et al. (2019), *MNRAS* 487, 4648–4668.

Stach, Stuart M., Ian Smail, A. M. Swinbank, et al. (2018), *ApJ* 860, 161.

Steinhauser, Dominik, Sabine Schindler & Volker Springel (2016), “Simulations of ram-pressure stripping in galaxy-cluster interactions”, *AAP* 591, A51.

Stern, Daniel, Raul Jimenez, Licia Verde, et al. (2010), *JCAP* 2010, 008.

Stevens, J. A., R. J. Ivison, J. S. Dunlop, et al. (2003), *NAT* 425, 264–267.

Stevens, J. A., Matt J. Jarvis, K. E. K. Coppin, et al. (2010), *MNRAS* 405, 2623–2638.

Tanaka, M., C. De Breuck, B. Venemans, et al. (2010), *AAP* 518, A18.

Trudeau, A., J. P. Willis, D. Rennehan, et al. (2022), *MNRAS* 515, 2529–2547.

Umehata, Hideki, Yoichi Tamura, Kotaro Kohno, et al. (2017), *ApJ* 835, 98.

van der Wel, A., M. Franx, P. G. van Dokkum, et al. (2014), *ApJ* 788, 28.

Weiß, A., A. Kovács, K. Coppin, et al. (2009), *ApJ* 707, 1201–1216.

Wylezalek, D., J. Vernet, C. De Breuck, et al. (2013), *MNRAS* 428, 3206–3219.

Zhang, Yuheng, Xian Zhong Zheng, Dong Dong Shi, et al. (2022), *MRAS* 512, 4893–4908.

Zirm, Andrew W., S. A. Stanford, M. Postman, et al. (2008), *AJ* 680, 224–231.

Appendix A

Detections and flux analysis

A.1 ALMA flux maps

We hereby display all the ALMA flux maps used in this analysis, signaling the sources with a white circle, whose size corresponds to the fixed size employed for the integrated flux. The red circle on the bottom right represents the beamsize for that weighting configuration. Per each detection, signal-to-noise ratio associated to best flux is reported. ALMA pointing associated to the LABOCA sources DKB06 and DKB09 showed no ALMA detections.

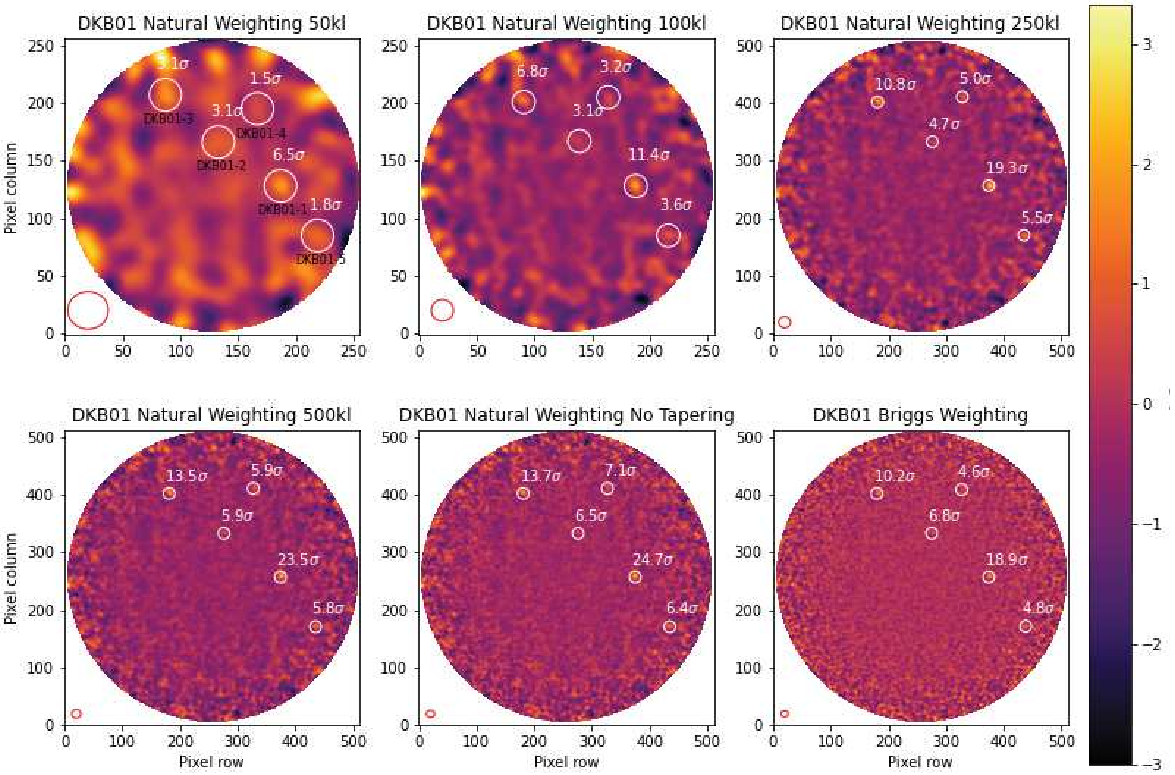

DKB01 Natural Weighting 50kl

DKB01 Natural Weighting 100kl

DKB01 Natural Weighting 250kl

DKB01 Natural Weighting 500kl

DKB01 Natural Weighting No Tapering

DKB01 Briggs Weighting

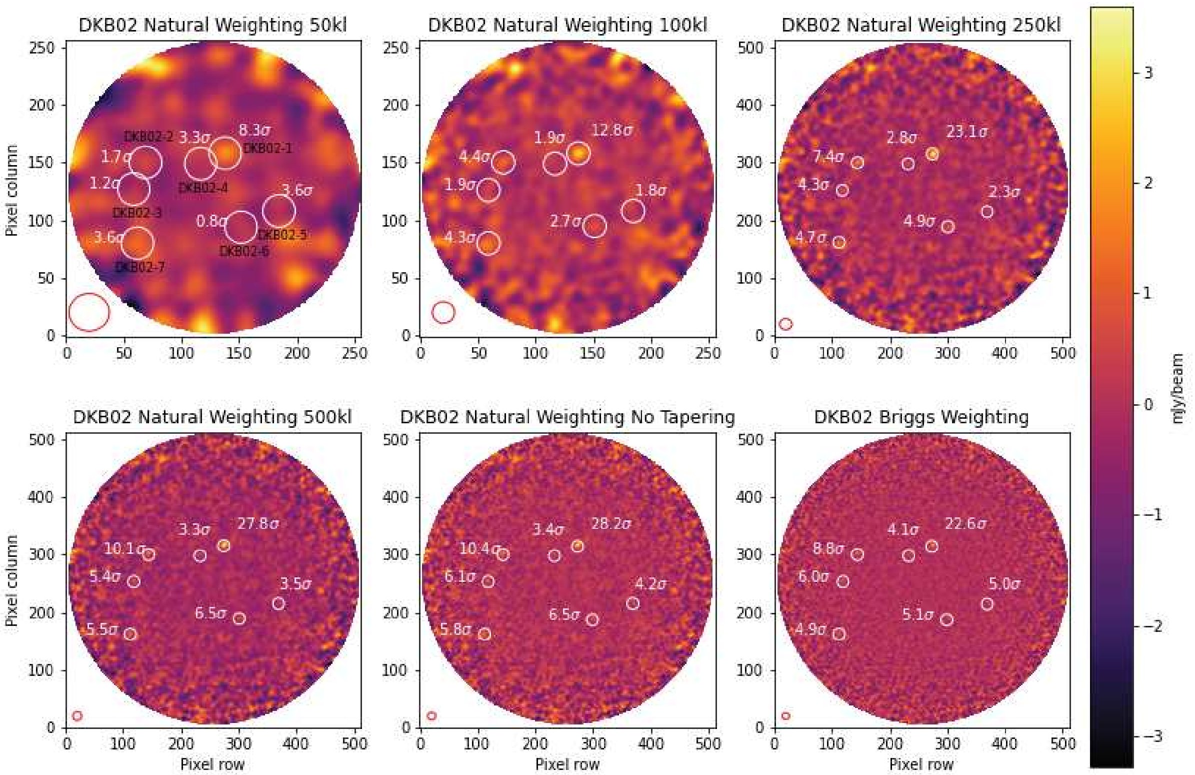
DKB02 Natural Weighting 50kl
DKB02 Natural Weighting 100kl
DKB02 Natural Weighting 250kl
DKB02 Natural Weighting 500kl
DKB02 Natural Weighting No Tapering
DKB02 Briggs Weighting
Pixel column
Pixel row
mJy/beam
DKB02-1
DKB02-2
DKB02-3
DKB02-4
DKB02-5
DKB02-6
DKB02-7
8.3σ
3.3σ
1.7σ
1.2σ
3.6σ
0.8σ
3.6σ
12.8σ
1.9σ
4.4σ
1.9σ
1.8σ
2.7σ
4.3σ
23.1σ
2.8σ
7.4σ
4.3σ
2.3σ
4.9σ
4.7σ
27.8σ
3.3σ
10.1σ
5.4σ
3.5σ
6.5σ
5.5σ
28.2σ
3.4σ
10.4σ
6.1σ
4.2σ
6.5σ
5.8σ
22.6σ
4.1σ
8.8σ
6.0σ
5.0σ
5.1σ
4.9σ

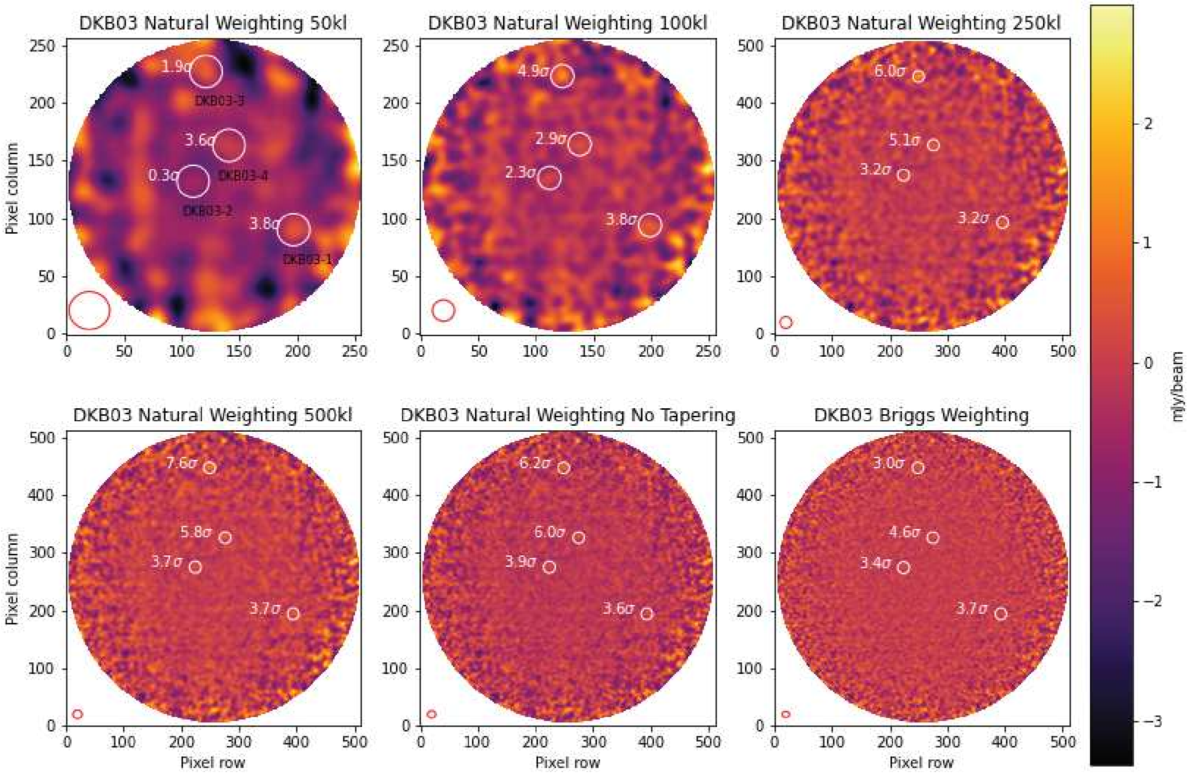
DKB03 Natural Weighting 50kl
DKB03 Natural Weighting 100kl
DKB03 Natural Weighting 250kl
DKB03 Natural Weighting 500kl
DKB03 Natural Weighting No Tapering
DKB03 Briggs Weighting
Pixel column
Pixel row
mJy/beam
DKB03-1
DKB03-2
DKB03-3
DKB03-4
1.9σ
3.6σ
0.3σ
3.8σ
4.9σ
2.9σ
2.3σ
3.8σ
6.0σ
5.1σ
3.2σ
3.2σ
7.6σ
5.8σ
3.7σ
3.7σ
6.2σ
6.0σ
3.9σ
3.6σ
3.0σ
4.6σ
3.4σ
3.7σ

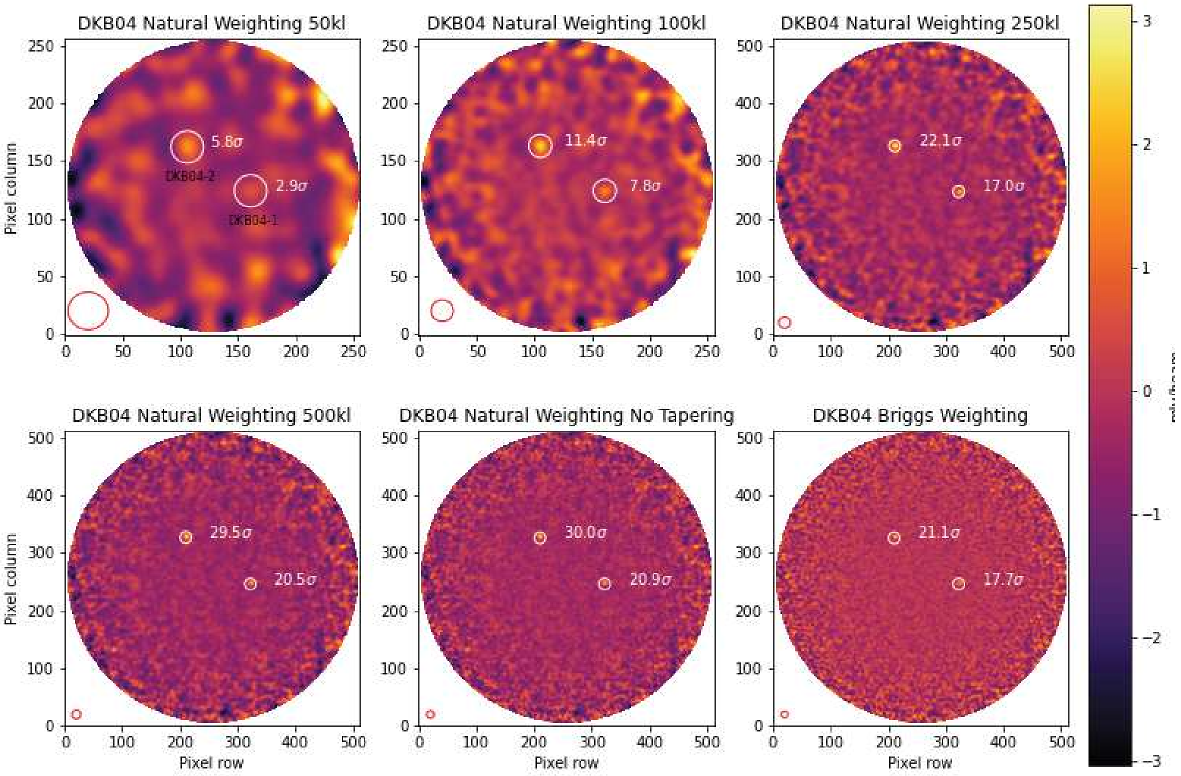

DKB04 Natural Weighting 50kl
5.8σ
DKB04-2
2.9σ
DKB04-1
DKB04 Natural Weighting 100kl
11.4σ
7.8σ
DKB04 Natural Weighting 250kl
22.1σ
17.0σ
DKB04 Natural Weighting 500kl
29.5σ
20.5σ
DKB04 Natural Weighting No Tapering
30.0σ
20.9σ
DKB04 Briggs Weighting
21.1σ
17.7σ
Pixel column
Pixel row
mJy/beam

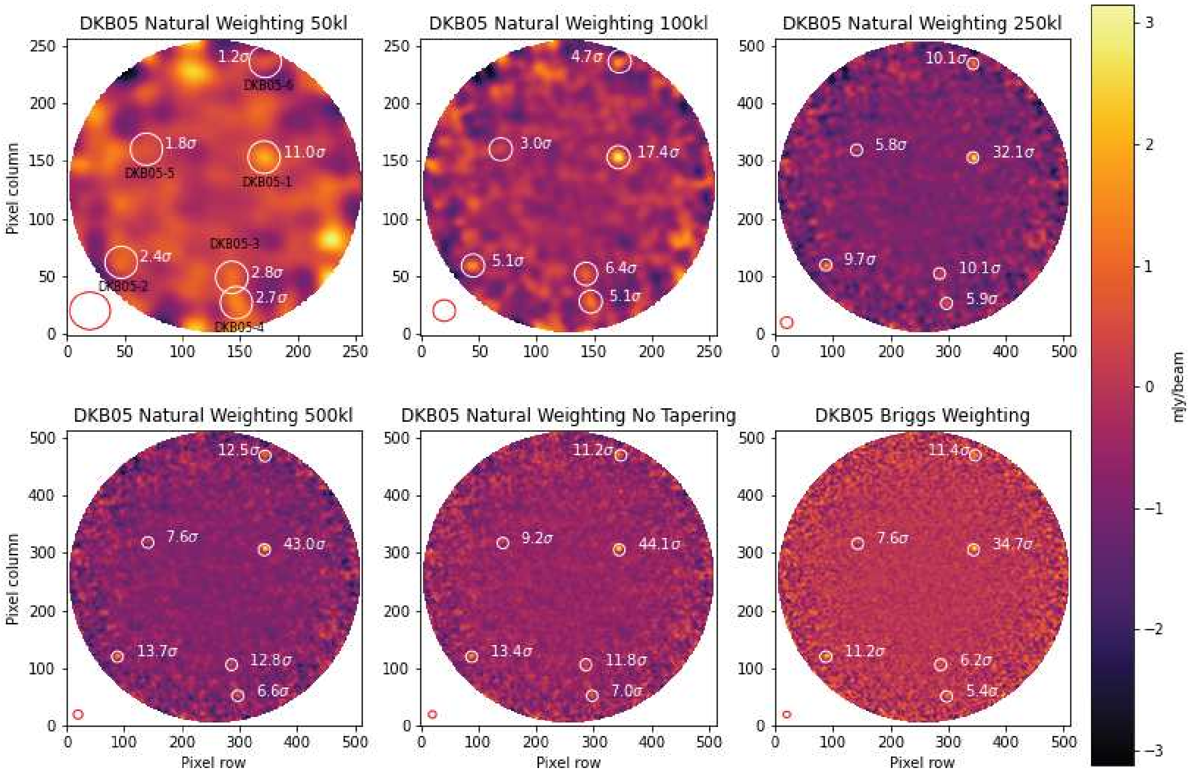

DKB05 Natural Weighting 50kl
1.2σ
DKB05-6
1.8σ
DKB05-5
11.0σ
DKB05-1
DKB05-3
2.4σ
DKB05-2
2.8σ
2.7σ
DKB05-4
DKB05 Natural Weighting 100kl
4.7σ
3.0σ
17.4σ
5.1σ
6.4σ
5.1σ
DKB05 Natural Weighting 250kl
10.1σ
5.8σ
32.1σ
9.7σ
10.1σ
5.9σ
DKB05 Natural Weighting 500kl
12.5σ
7.6σ
43.0σ
13.7σ
12.8σ
6.6σ
DKB05 Natural Weighting No Tapering
11.2σ
9.2σ
44.1σ
13.4σ
11.8σ
7.0σ
DKB05 Briggs Weighting
11.4σ
7.6σ
34.7σ
11.2σ
6.2σ
5.4σ
Pixel column
Pixel row
mJy/beam

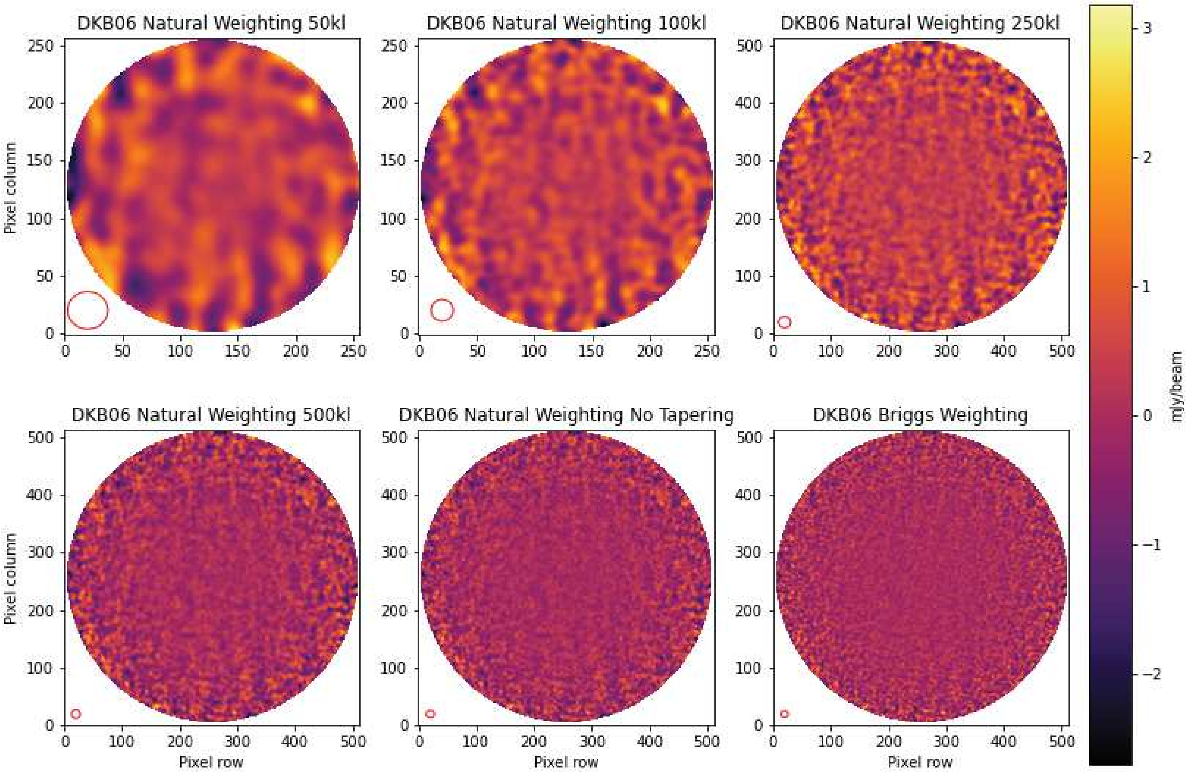
DKB06 Natural Weighting 50kl
DKB06 Natural Weighting 100kl
DKB06 Natural Weighting 250kl
DKB06 Natural Weighting 500kl
DKB06 Natural Weighting No Tapering
DKB06 Briggs Weighting
Pixel column
Pixel row
0
50
100
150
200
250
300
400
500
mJy/beam
3
2
1
0
−1
−2

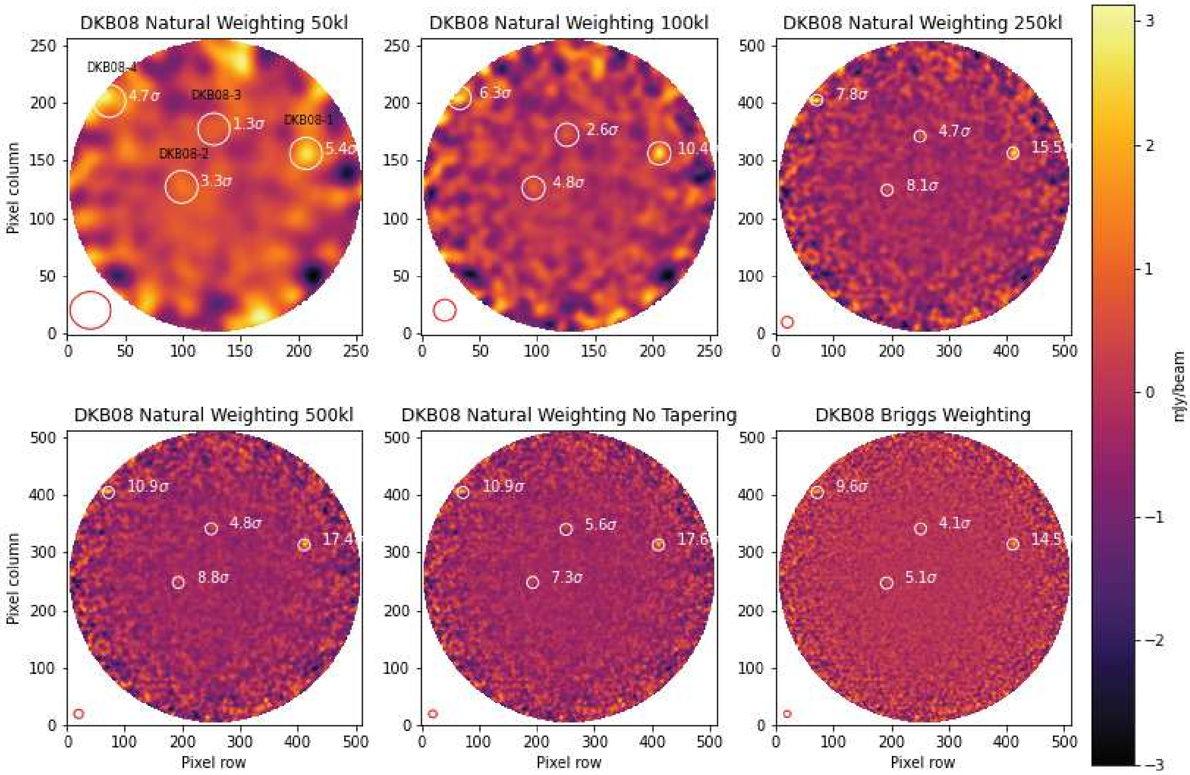
DKB08 Natural Weighting 50kl
DKB08-4
4.7σ
DKB08-3
1.3σ
DKB08-1
5.4σ
DKB08-2
3.3σ
DKB08 Natural Weighting 100kl
6.3σ
2.6σ
10.4
4.8σ
DKB08 Natural Weighting 250kl
7.8σ
4.7σ
15.5
8.1σ
DKB08 Natural Weighting 500kl
10.9σ
4.8σ
17.4
8.8σ
DKB08 Natural Weighting No Tapering
10.9σ
5.6σ
17.6
7.3σ
DKB08 Briggs Weighting
9.6σ
4.1σ
14.5
5.1σ
Pixel column
Pixel row
0
50
100
150
200
250
300
400
500
mJy/beam
3
2
1
0
−1
−2
−3

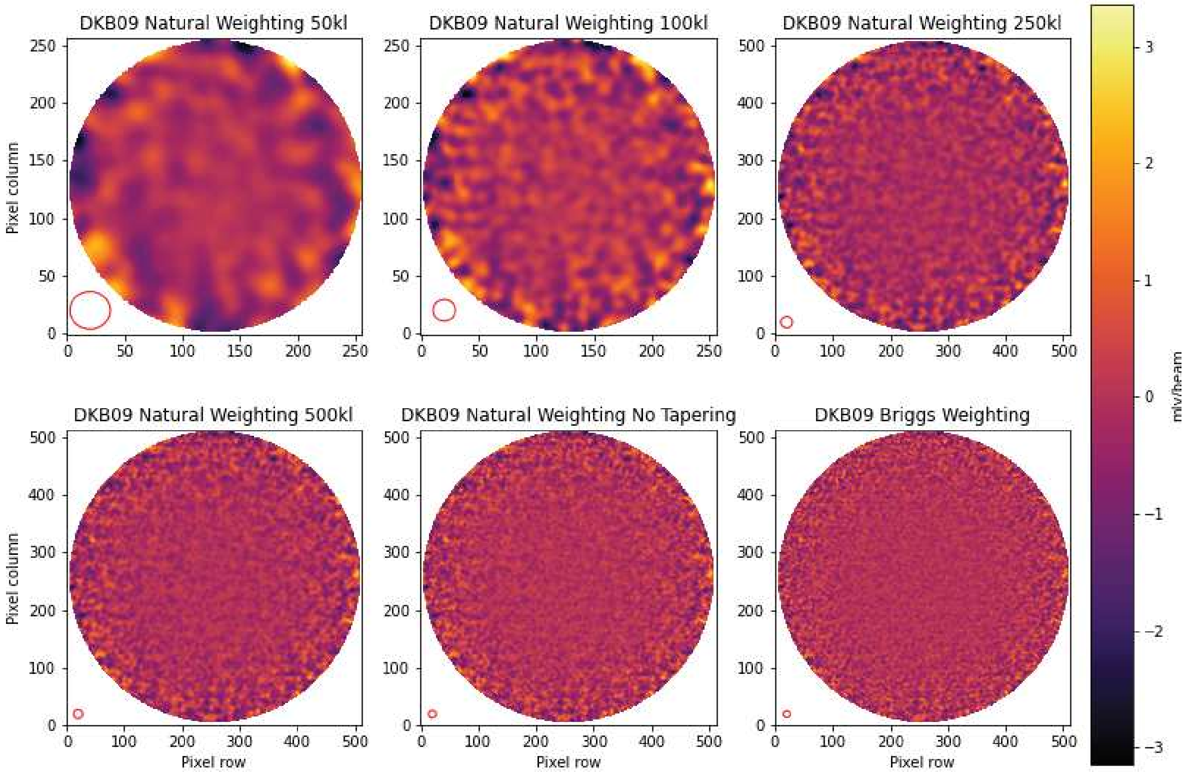
DKB09 Natural Weighting 50kl
DKB09 Natural Weighting 100kl
DKB09 Natural Weighting 250kl
DKB09 Natural Weighting 500kl
DKB09 Natural Weighting No Tapering
DKB09 Briggs Weighting
Pixel column
Pixel row
mJy/beam
3
2
1
0
−1
−2
−3

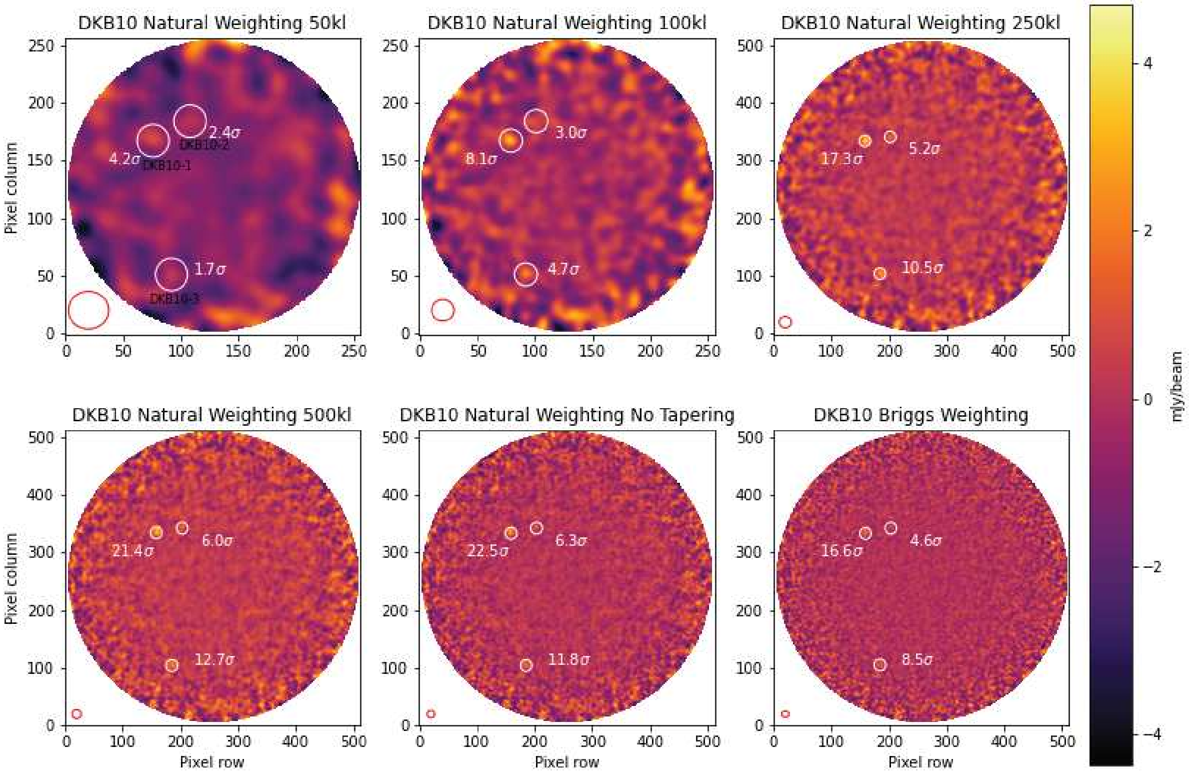
DKB10 Natural Weighting 50kl
4.2σ
DKB10-1
2.4σ
DKB10-2
1.7σ
DKB10-3
DKB10 Natural Weighting 100kl
8.1σ
3.0σ
4.7σ
DKB10 Natural Weighting 250kl
17.3σ
5.2σ
10.5σ
DKB10 Natural Weighting 500kl
21.4σ
6.0σ
12.7σ
DKB10 Natural Weighting No Tapering
22.5σ
6.3σ
11.8σ
DKB10 Briggs Weighting
16.6σ
4.6σ
8.5σ
Pixel column
Pixel row
mJy/beam
4
2
0
−2
−4

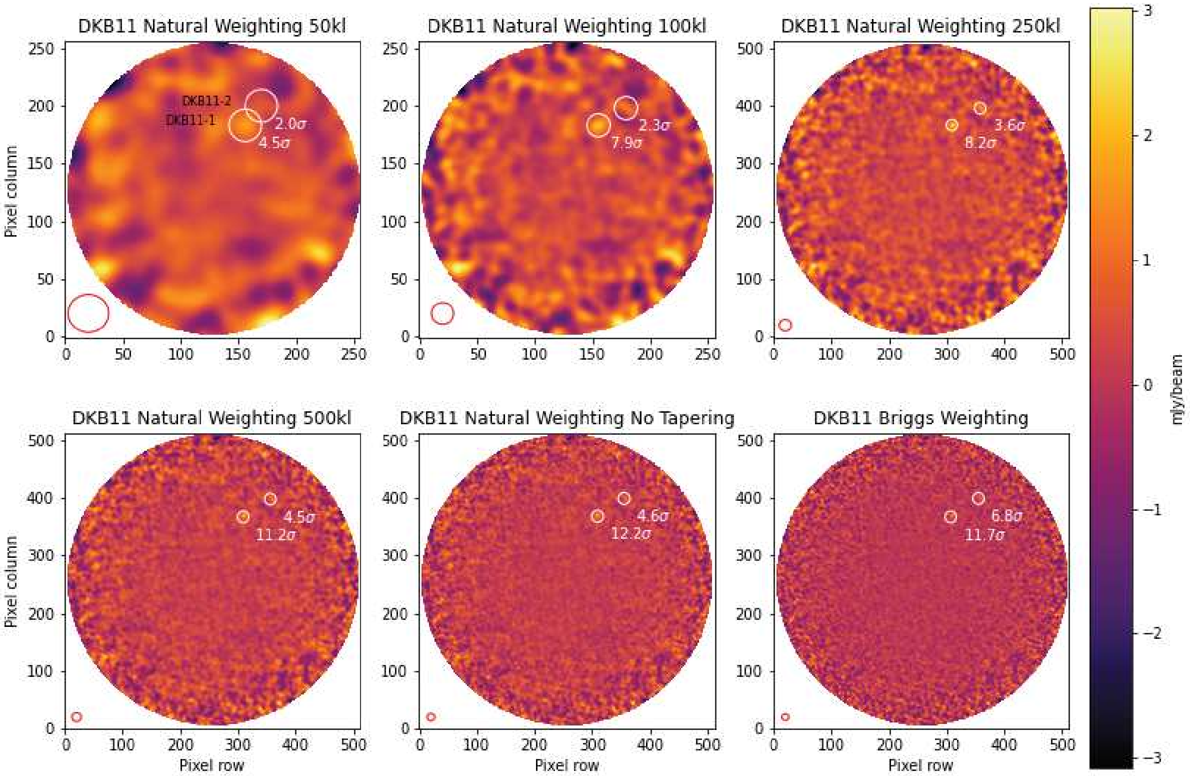
DKB11 Natural Weighting 50kl
DKB11-2
DKB11-1
2.0σ
4.5σ
DKB11 Natural Weighting 100kl
2.3σ
7.9σ
DKB11 Natural Weighting 250kl
3.6σ
8.2σ
DKB11 Natural Weighting 500kl
4.5σ
11.2σ
DKB11 Natural Weighting No Tapering
4.6σ
12.2σ
DKB11 Briggs Weighting
6.8σ
11.7σ
Pixel column
Pixel row
mJy/beam
3
2
1
0
−1
−2
−3

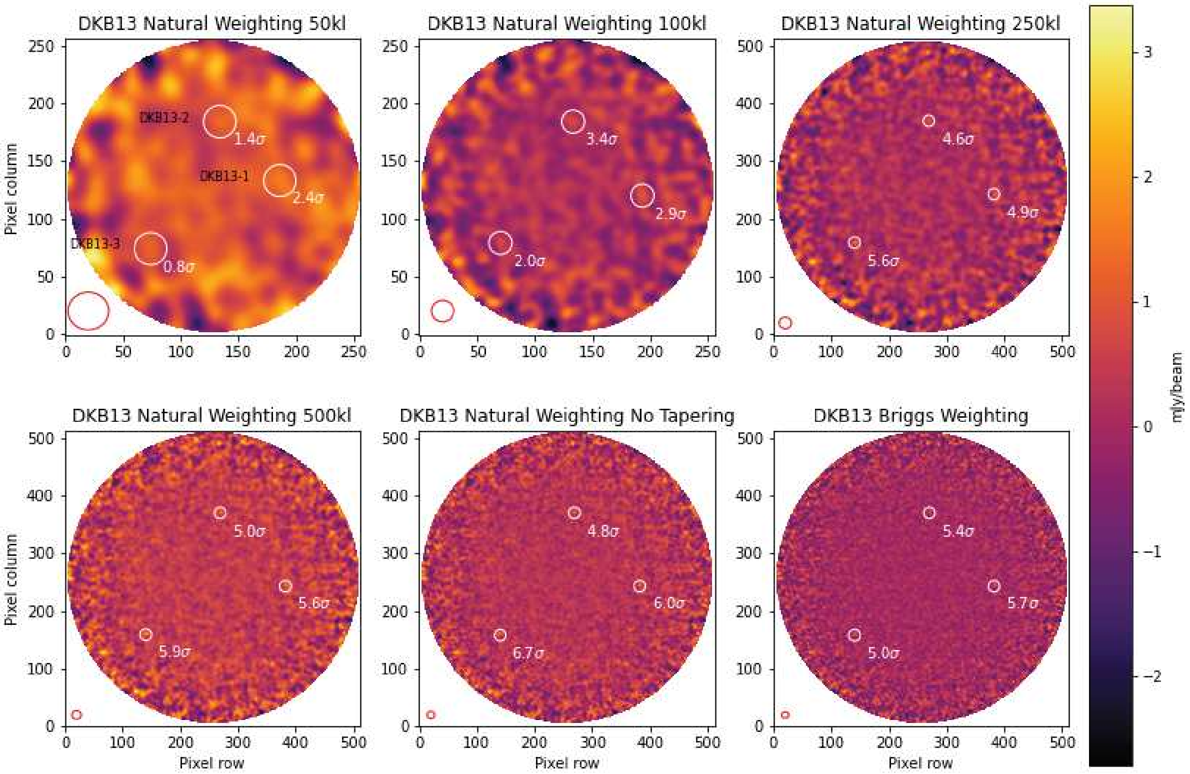
DKB13 Natural Weighting 50kl
DKB13-2
1.4σ
DKB13-1
2.4σ
DKB13-3
0.8σ
DKB13 Natural Weighting 100kl
3.4σ
2.9σ
2.0σ
DKB13 Natural Weighting 250kl
4.6σ
4.9σ
5.6σ
DKB13 Natural Weighting 500kl
5.0σ
5.6σ
5.9σ
DKB13 Natural Weighting No Tapering
4.8σ
6.0σ
6.7σ
DKB13 Briggs Weighting
5.4σ
5.7σ
5.0σ
Pixel column
Pixel row
mJy/beam
3
2
1
0
−1
−2

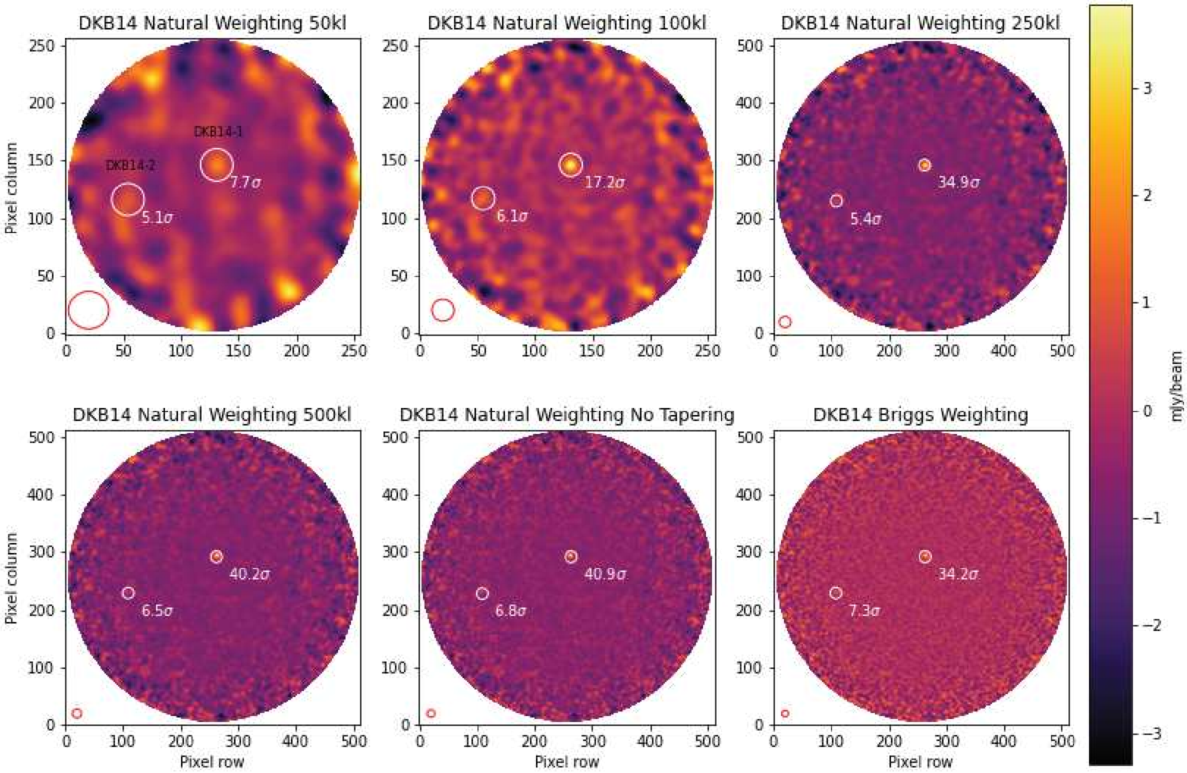
DKB14 Natural Weighting 50kl
DKB14-1
DKB14-2
7.7σ
5.1σ
DKB14 Natural Weighting 100kl
17.2σ
6.1σ
DKB14 Natural Weighting 250kl
34.9σ
5.4σ
DKB14 Natural Weighting 500kl
40.2σ
6.5σ
DKB14 Natural Weighting No Tapering
40.9σ
6.8σ
DKB14 Briggs Weighting
34.2σ
7.3σ
Pixel column
Pixel row
mJy/beam
3
2
1
0
−1
−2
−3

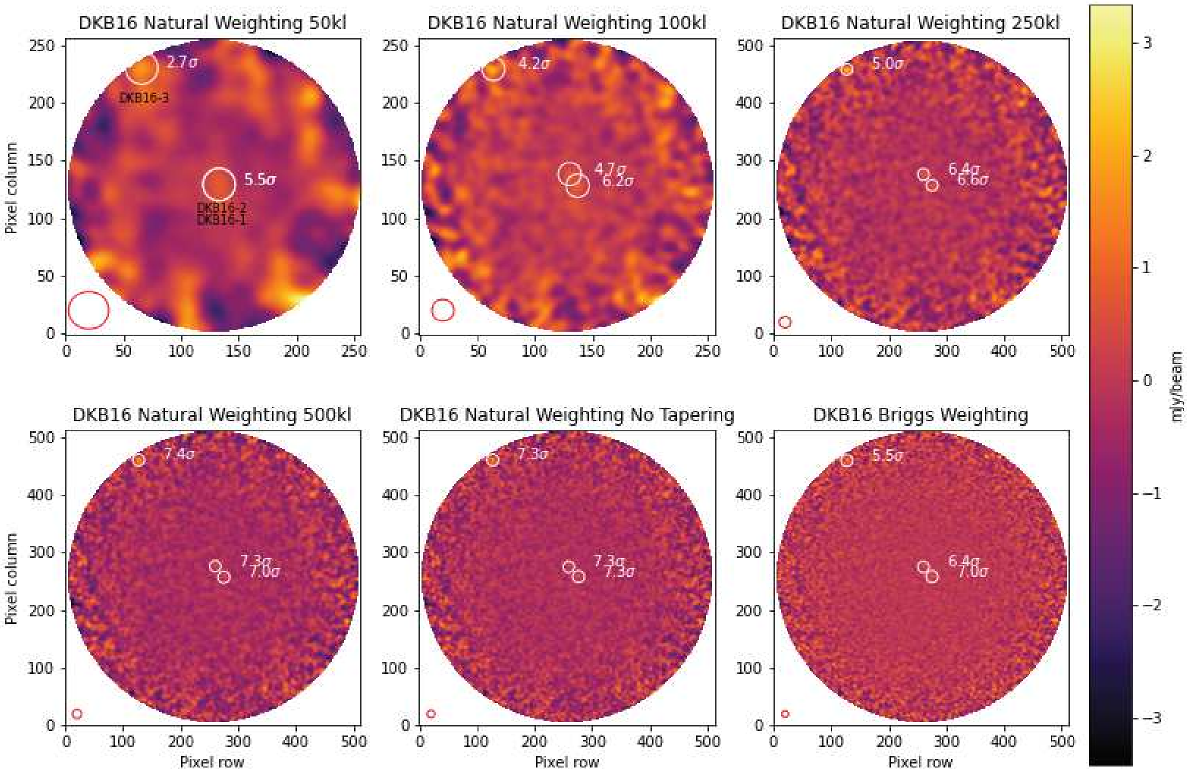
DKB16 Natural Weighting 50kl
2.7σ
DKB16-3
5.5σ
DKB16-2
DKB16-1
DKB16 Natural Weighting 100kl
4.2σ
4.7σ
6.2σ
DKB16 Natural Weighting 250kl
5.0σ
6.4σ
6.6σ
DKB16 Natural Weighting 500kl
7.4σ
7.3σ
7.0σ
DKB16 Natural Weighting No Tapering
7.3σ
7.3σ
7.3σ
DKB16 Briggs Weighting
5.5σ
6.4σ
7.0σ
Pixel column
Pixel row
mJy/beam
3
2
1
0
−1
−2
−3

A.2 Flux measurements

We hereby report all the peak (blue dots) and integrated flux measurements (green dots) for the detected ALMA sources, represented as a function of beamsize. Errorbars are given by the noise estimate.

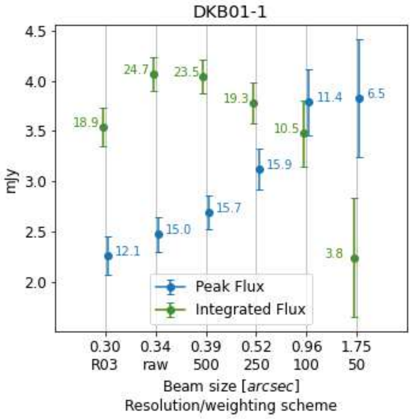

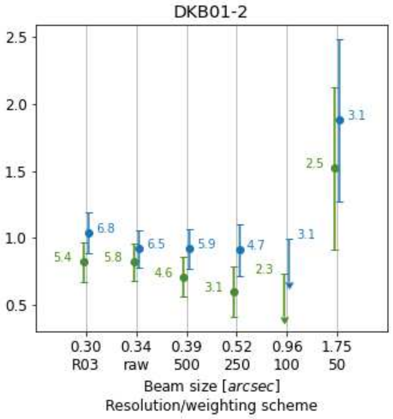

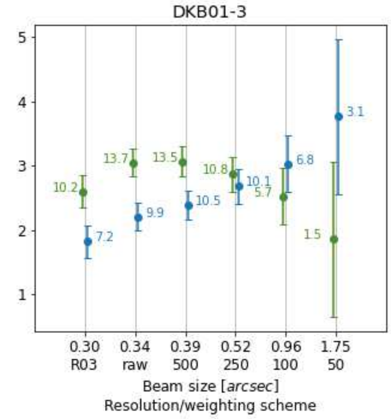

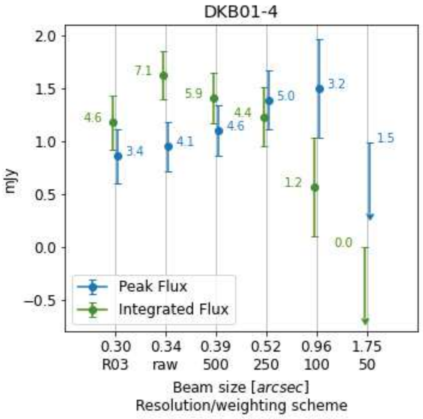

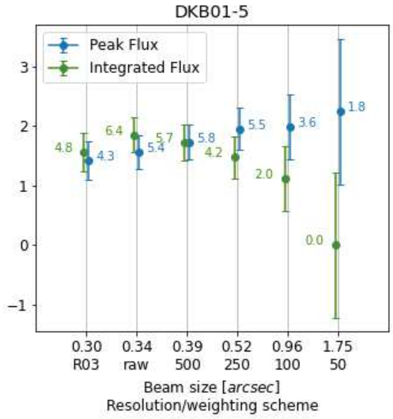

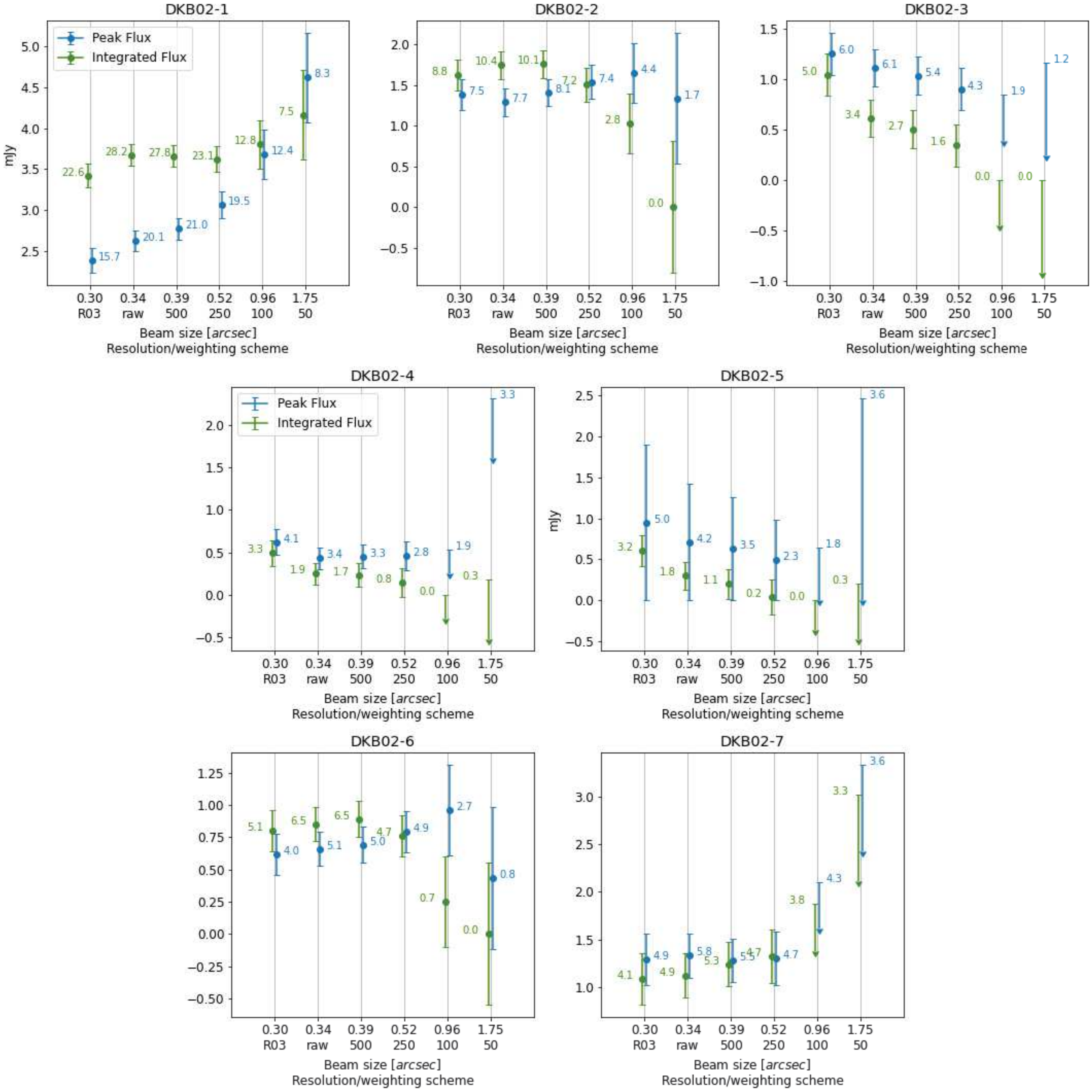
DKB02-1
DKB02-2
DKB02-3
DKB02-4
DKB02-5
DKB02-6
DKB02-7
Peak Flux
Integrated Flux
mJy
Beam size [arcsec]
Resolution/weighting scheme
0.30
R03
0.34
raw
0.39
500
0.52
250
0.96
100
1.75
50
22.6
28.2
27.8
23.1
12.8
7.5
15.7
20.1
21.0
19.5
12.4
8.3
8.8
10.4
10.1
7.2
2.8
0.0
7.5
7.7
8.1
7.4
4.4
1.7
5.0
3.4
2.7
1.6
0.0
0.0
6.0
6.1
5.4
4.3
1.9
1.2
3.3
1.9
1.7
0.8
0.0
0.3
4.1
3.4
3.3
2.8
1.9
3.3
3.2
1.8
1.1
0.2
0.0
0.3
5.0
4.2
3.5
2.3
1.8
3.6
5.1
6.5
6.5
4.7
0.7
0.0
4.0
5.1
5.0
4.9
2.7
0.8
4.1
4.9
5.3
4.7
3.8
3.3
4.9
5.8
5.5
4.7
4.3
3.6

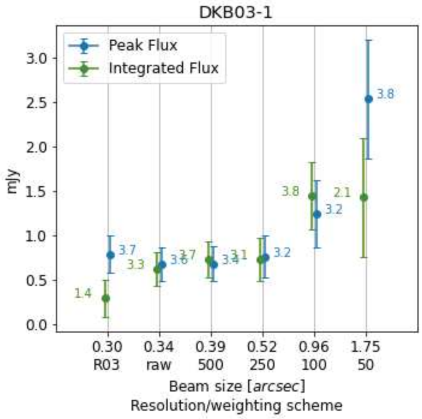
DKB03-1
Peak Flux
Integrated Flux
mJy
0.0
0.5
1.0
1.5
2.0
2.5
3.0
3.7
3.6
3.4
3.2
3.2
3.8
1.4
3.3
3.7
3.1
3.8
2.1
0.30
R03
0.34
raw
0.39
500
0.52
250
0.96
100
1.75
50
Beam size [arcsec]
Resolution/weighting scheme

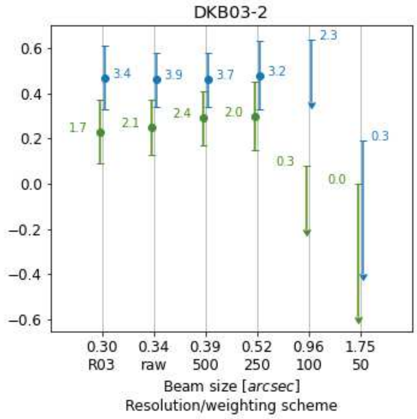
DKB03-2
−0.6
−0.4
−0.2
0.0
0.2
0.4
0.6
3.4
3.9
3.7
3.2
2.3
0.3
1.7
2.1
2.4
2.0
0.3
0.0
0.30
R03
0.34
raw
0.39
500
0.52
250
0.96
100
1.75
50
Beam size [arcsec]
Resolution/weighting scheme

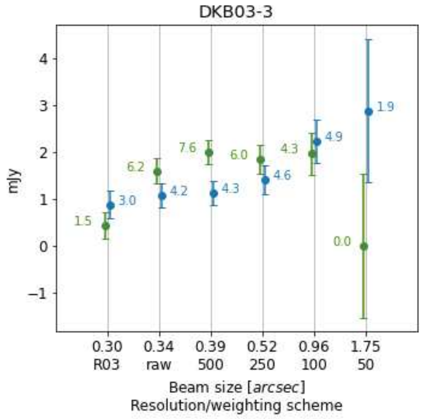
DKB03-3
mJy
−1
0
1
2
3
4
3.0
4.2
4.3
4.6
4.9
1.9
1.5
6.2
7.6
6.0
4.3
0.0
0.30
R03
0.34
raw
0.39
500
0.52
250
0.96
100
1.75
50
Beam size [arcsec]
Resolution/weighting scheme

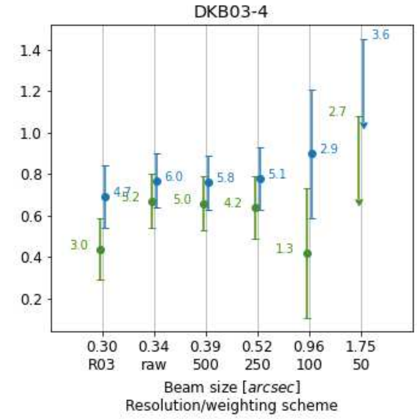
DKB03-4
0.2
0.4
0.6
0.8
1.0
1.2
1.4
4.7
6.0
5.8
5.1
2.9
3.6
3.0
3.2
5.0
4.2
1.3
2.7
0.30
R03
0.34
raw
0.39
500
0.52
250
0.96
100
1.75
50
Beam size [arcsec]
Resolution/weighting scheme

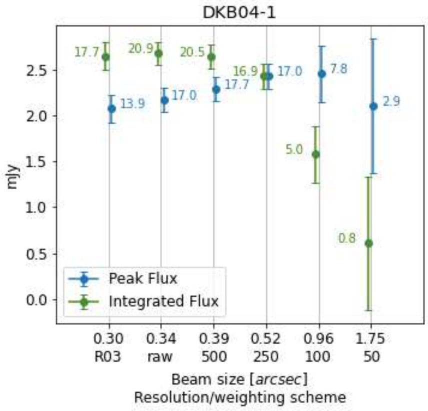
DKB04-1
Peak Flux
Integrated Flux
mJy
0.0
0.5
1.0
1.5
2.0
2.5
13.9
17.0
17.7
17.0
7.8
2.9
17.7
20.9
20.5
16.9
5.0
0.8
0.30
R03
0.34
raw
0.39
500
0.52
250
0.96
100
1.75
50
Beam size [arcsec]
Resolution/weighting scheme

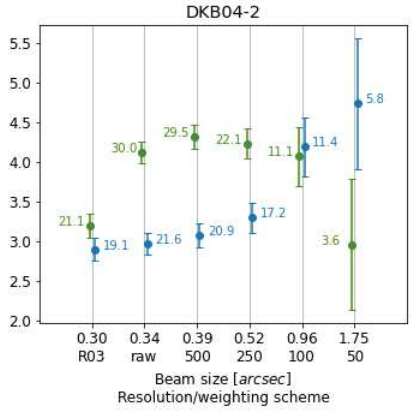
DKB04-2
2.0
2.5
3.0
3.5
4.0
4.5
5.0
5.5
19.1
21.6
20.9
17.2
11.4
5.8
21.1
30.0
29.5
22.1
11.1
3.6
0.30
R03
0.34
raw
0.39
500
0.52
250
0.96
100
1.75
50
Beam size [arcsec]
Resolution/weighting scheme

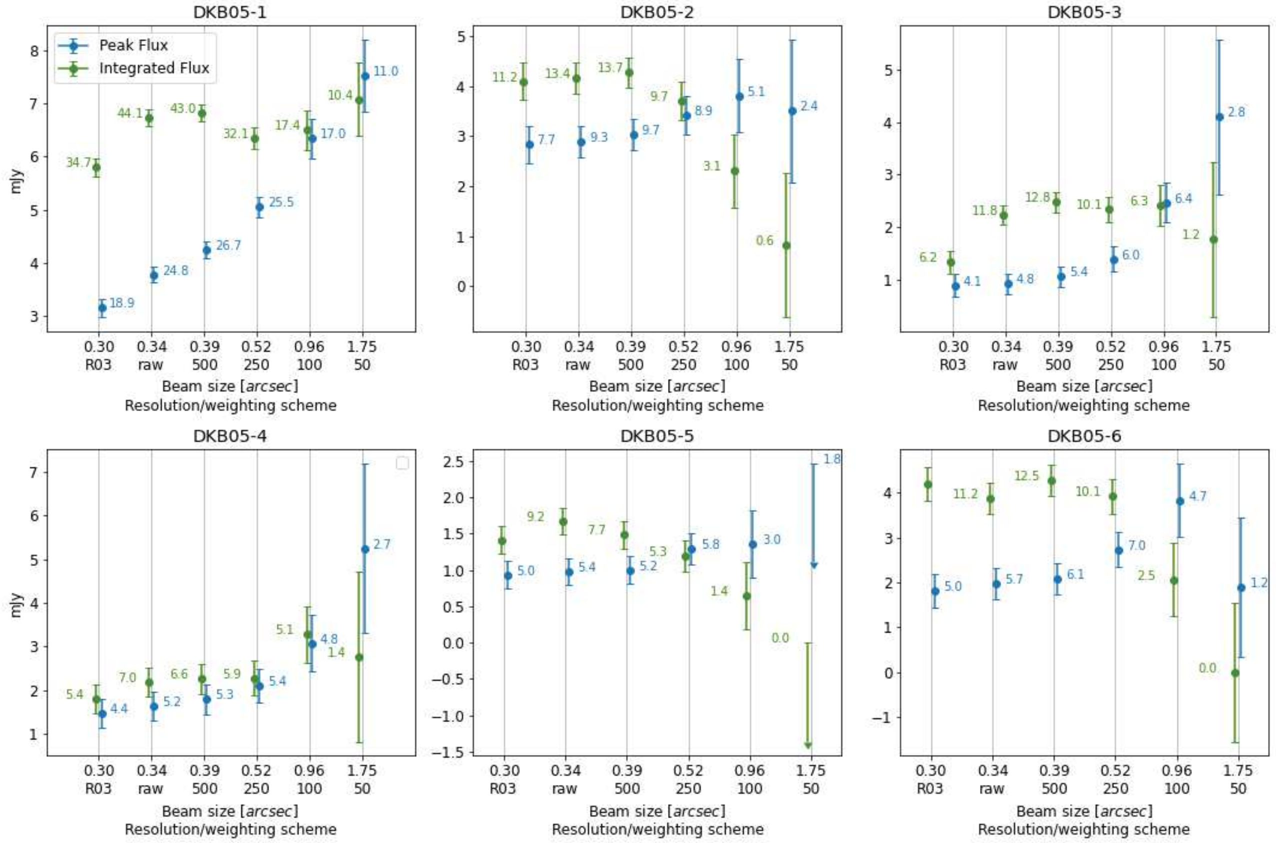
DKB05-1
Peak Flux
Integrated Flux
mJy
8
7
6
5
4
3
34.7
44.1
43.0
32.1
17.4
10.4
18.9
24.8
26.7
25.5
17.0
11.0
DKB05-2
5
4
3
2
1
0
11.2
13.4
13.7
9.7
3.1
0.6
7.7
9.3
9.7
8.9
5.1
2.4
DKB05-3
5
4
3
2
1
6.2
11.8
12.8
10.1
6.3
1.2
4.1
4.8
5.4
6.0
6.4
2.8
DKB05-4
mJy
7
6
5
4
3
2
1
5.4
7.0
6.6
5.9
5.1
1.4
4.4
5.2
5.3
5.4
4.8
2.7
DKB05-5
2.5
2.0
1.5
1.0
0.5
0.0
−0.5
−1.0
−1.5
9.2
7.7
5.3
1.4
0.0
5.0
5.4
5.2
5.8
3.0
1.8
DKB05-6
4
3
2
1
0
−1
11.2
12.5
10.1
2.5
0.0
5.0
5.7
6.1
7.0
4.7
1.2
0.30 R03
0.34 raw
0.39 500
0.52 250
0.96 100
1.75 50
Beam size [arcsec]
Resolution/weighting scheme

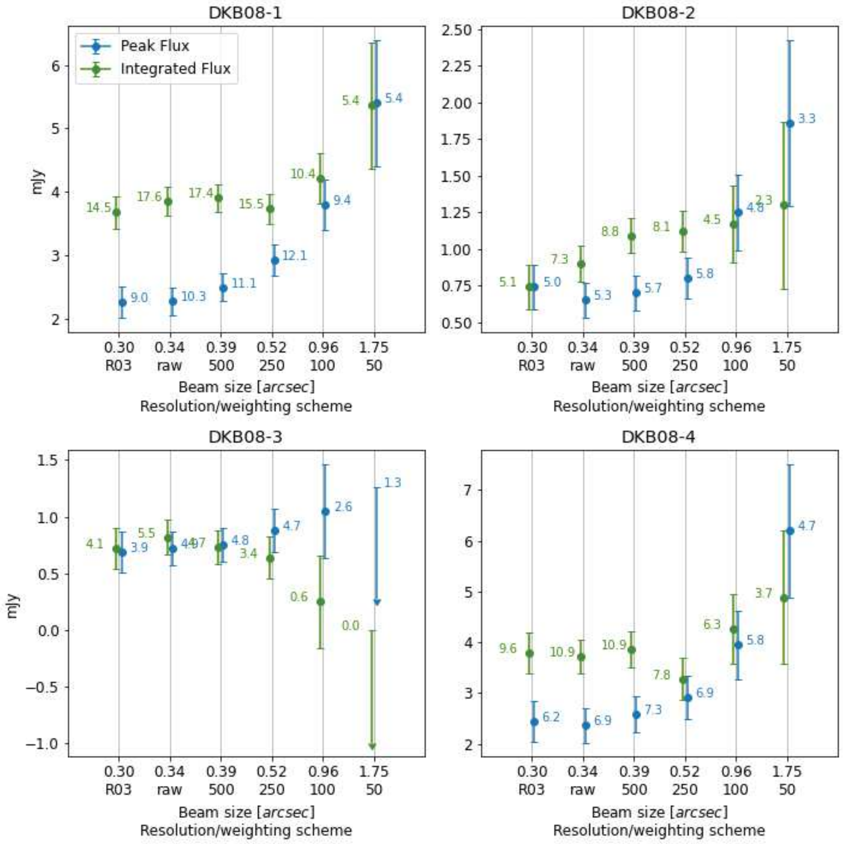
DKB08-1
Peak Flux
Integrated Flux
mJy
6
5
4
3
2
14.5
17.6
17.4
15.5
10.4
5.4
9.0
10.3
11.1
12.1
9.4
5.4
DKB08-2
2.50
2.25
2.00
1.75
1.50
1.25
1.00
0.75
0.50
5.1
7.3
8.8
8.1
4.5
2.3
5.0
5.3
5.7
5.8
4.8
3.3
DKB08-3
mJy
1.5
1.0
0.5
0.0
−0.5
−1.0
4.1
5.5
4.7
3.4
0.6
0.0
3.9
4.4
4.8
4.7
2.6
1.3
DKB08-4
7
6
5
4
3
2
9.6
10.9
10.9
7.8
6.3
3.7
6.2
6.9
7.3
6.9
5.8
4.7
0.30 R03
0.34 raw
0.39 500
0.52 250
0.96 100
1.75 50
Beam size [arcsec]
Resolution/weighting scheme

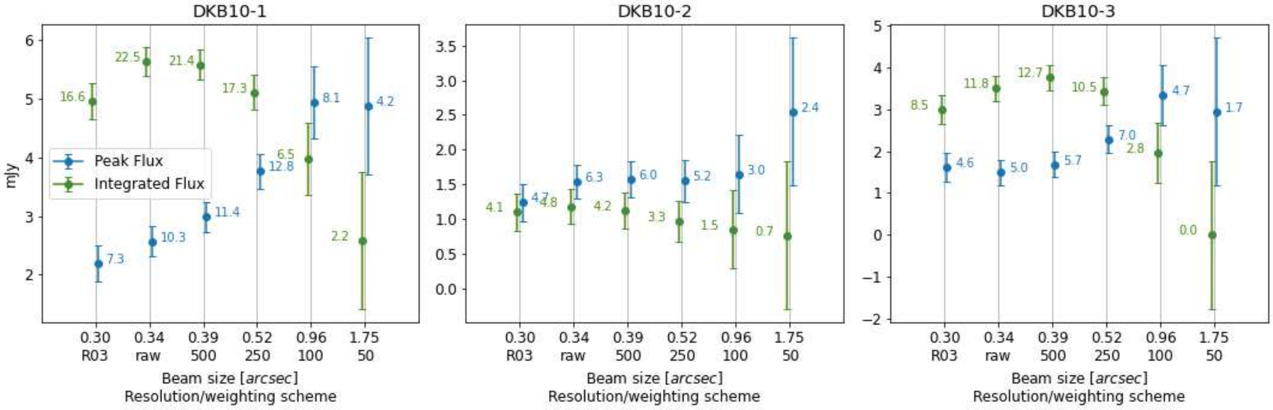
DKB10-1
DKB10-2
DKB10-3
Peak Flux
Integrated Flux
mJy
Beam size [*arcsec*]
Resolution/weighting scheme
0.30 R03
0.34 raw
0.39 500
0.52 250
0.96 100
1.75 50
16.6
22.5
21.4
17.3
6.5
2.2
7.3
10.3
11.4
12.8
8.1
4.2
4.1
4.7
4.8
4.2
3.3
1.5
0.7
6.3
6.0
5.2
3.0
2.4
8.5
11.8
12.7
10.5
2.8
0.0
4.6
5.0
5.7
7.0
4.7
1.7

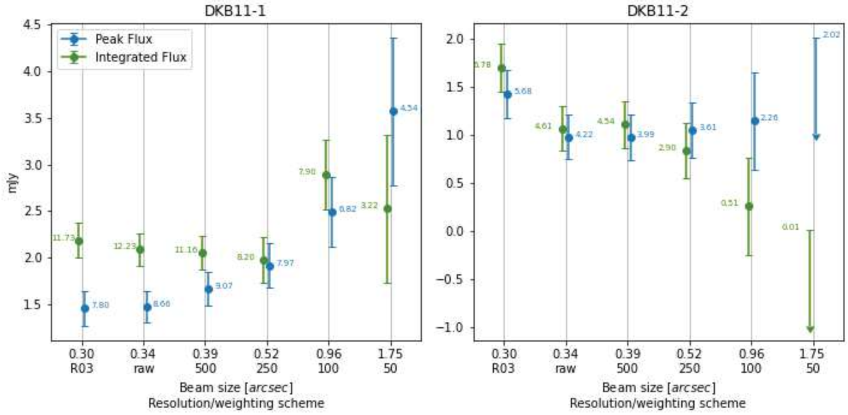
DKB11-1
DKB11-2
Peak Flux
Integrated Flux
mJy
Beam size [*arcsec*]
Resolution/weighting scheme
0.30 R03
0.34 raw
0.39 500
0.52 250
0.96 100
1.75 50
11.73
12.23
11.16
8.20
7.90
3.22
7.80
8.66
9.07
7.97
6.82
4.54
5.78
4.61
4.54
2.90
0.51
0.01
5.68
4.22
3.99
3.61
2.26
2.02

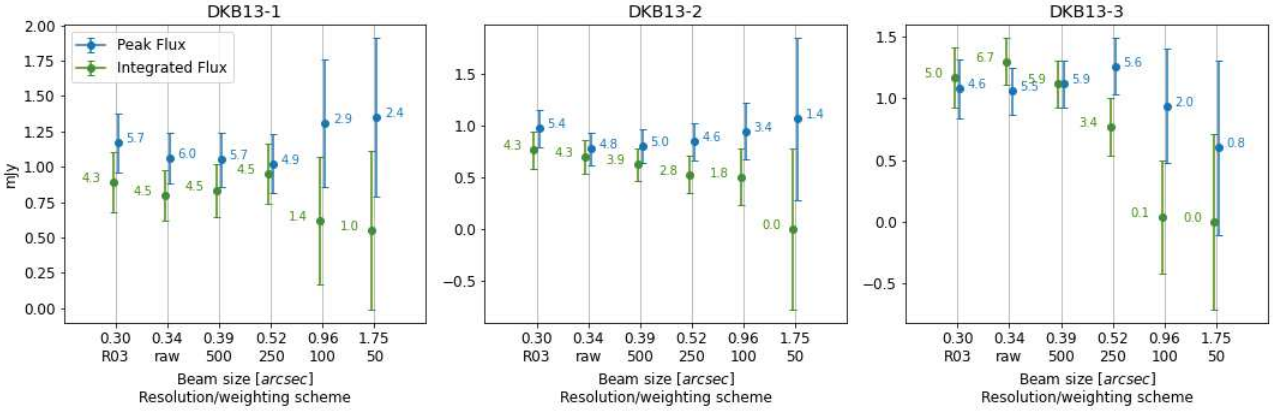
DKB13-1
DKB13-2
DKB13-3
Peak Flux
Integrated Flux
mJy
Beam size [*arcsec*]
Resolution/weighting scheme
0.30 R03
0.34 raw
0.39 500
0.52 250
0.96 100
1.75 50
4.3
4.5
4.5
4.5
1.4
1.0
5.7
6.0
5.7
4.9
2.9
2.4
4.3
4.3
3.9
2.8
1.8
0.0
5.4
4.8
5.0
4.6
3.4
1.4
5.0
6.7
5.9
3.4
0.1
0.0
4.6
5.5
5.9
5.6
2.0
0.8

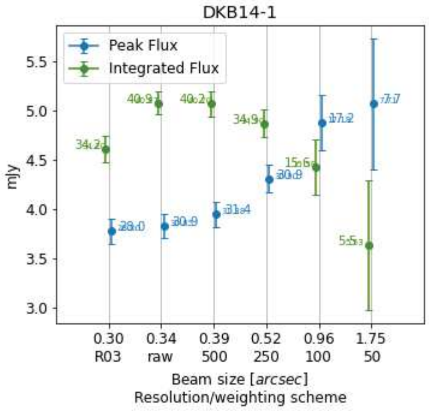
DKB14-1
Peak Flux
Integrated Flux
mJy
5.5
5.0
4.5
4.0
3.5
3.0
34.2
40.9
40.2
34.9
15.6
5.5
28.0
30.9
31.4
30.9
17.2
7.7
0.30
R03
0.34
raw
0.39
500
0.52
250
0.96
100
1.75
50
Beam size [arcsec]
Resolution/weighting scheme

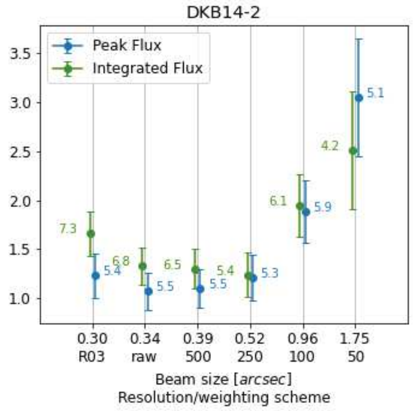
DKB14-2
Peak Flux
Integrated Flux
3.5
3.0
2.5
2.0
1.5
1.0
7.3
5.4
6.8
5.5
6.5
5.5
5.4
5.3
6.1
5.9
4.2
5.1
0.30
R03
0.34
raw
0.39
500
0.52
250
0.96
100
1.75
50
Beam size [arcsec]
Resolution/weighting scheme

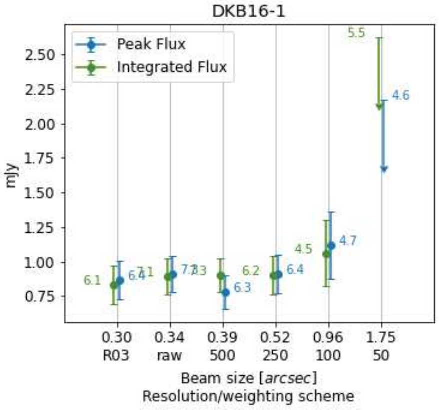
DKB16-1
Peak Flux
Integrated Flux
mJy
2.50
2.25
2.00
1.75
1.50
1.25
1.00
0.75
5.5
4.6
6.1
6.4
7.1
7.7
7.3
6.2
6.3
6.4
4.5
4.7
0.30
R03
0.34
raw
0.39
500
0.52
250
0.96
100
1.75
50
Beam size [arcsec]
Resolution/weighting scheme

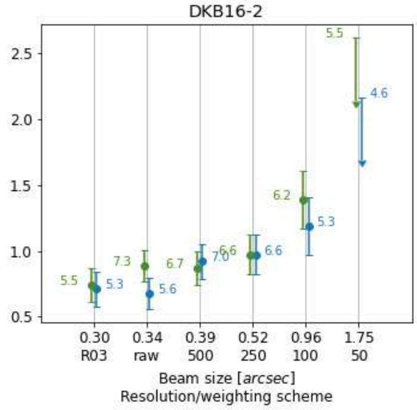
DKB16-2
2.5
2.0
1.5
1.0
0.5
5.5
4.6
6.2
5.3
7.3
6.7
7.0
6.6
6.6
5.5
5.3
5.6
0.30
R03
0.34
raw
0.39
500
0.52
250
0.96
100
1.75
50
Beam size [arcsec]
Resolution/weighting scheme

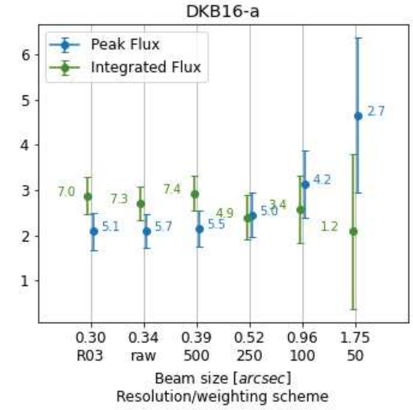
DKB16-a
Peak Flux
Integrated Flux
6
5
4
3
2
1
2.7
4.2
7.0
7.3
7.4
4.9
3.4
5.0
5.1
5.7
5.5
1.2
0.30
R03
0.34
raw
0.39
500
0.52
250
0.96
100
1.75
50
Beam size [arcsec]
Resolution/weighting scheme

Appendix B

Multi-wavelength gallery

Here we report the preliminary counterpart matching that we built in this thesis for our detected ALMA catalogue. We display a comparison between the available maps, from the optical, through NIR and FIR, until the radio regime.

In each band, we operate a comparison between our natural-weighted, 250kλ-tapered ALMA flux maps (left panels) with the filter under exam, (right panels). Circles mark the detected ALMA sources, color-coded basing on the quality factor: red for Q=1, blue for Q=2, cyan for Q=3. If the source is not covered by that wavelength regime, it is not shown.

B.1 HST/ACS/WFC (814 nm)

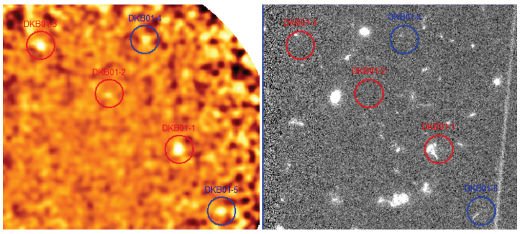

DKB01

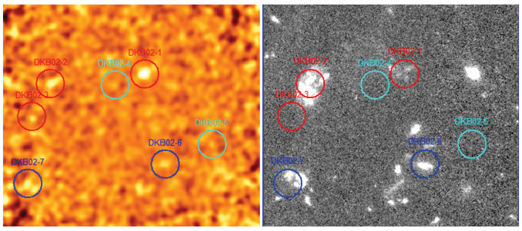

DKB02

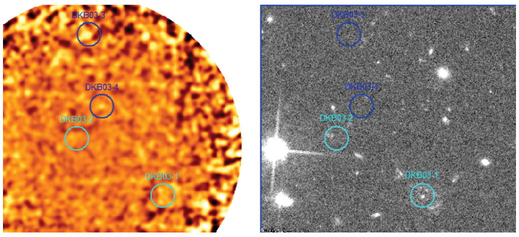

DKB03

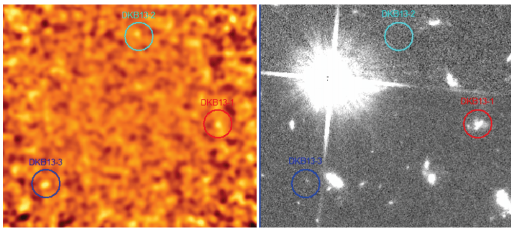

DKB13

B.2 HST/NICMOS/110W (1.1μm)

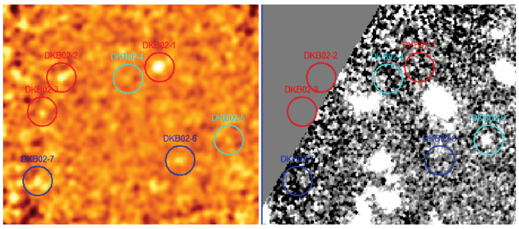
DKB02-1
DKB02-2
DKB02-4
DKB02-3
DKB02-5
DKB02-6
DKB02-7
DKB02-1
DKB02-2
DKB02-4
DKB02-3
DKB02-5
DKB02-6
DKB02-7

DKB02

B.3 HST/NICMOS/160W (1.6μm)

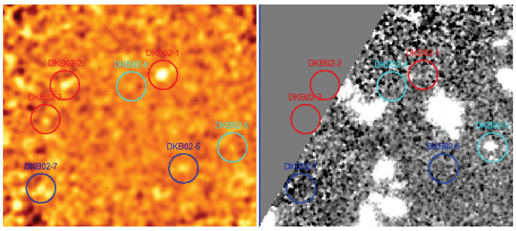
DKB02-1
DKB02-2
DKB02-4
DKB02-3
DKB02-5
DKB02-6
DKB02-7
DKB02-1
DKB02-2
DKB02-4
DKB02-3
DKB02-5
DKB02-6
DKB02-7

DKB02

B.4 VLT/HAWK-I/Y (1.0μm)

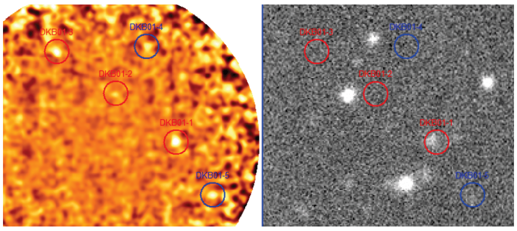
DKB01-3
DKB01-4
DKB01-2
DKB01-1
DKB01-5
DKB01-3
DKB01-4
DKB01-2
DKB01-1
DKB01-5

DKB01

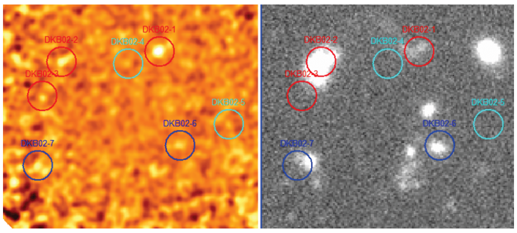
DKB02-2
DKB02-4
DKB02-1
DKB02-3
DKB02-5
DKB02-6
DKB02-7
DKB02-2
DKB02-4
DKB02-1
DKB02-3
DKB02-5
DKB02-6
DKB02-7

DKB02

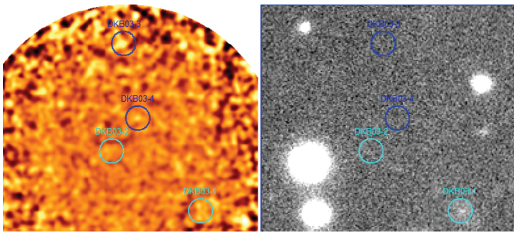
DKB03-3
DKB03-4
DKB03-2
DKB03-1
DKB03-3
DKB03-4
DKB03-2
DKB03-1

DKB03

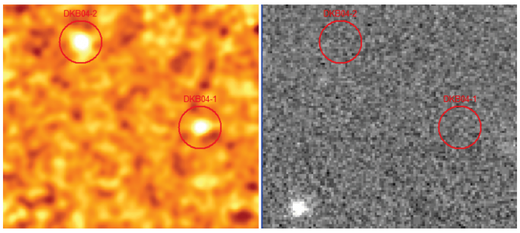
DKB04-2
DKB04-1
DKB04-2
DKB04-1

DKB04

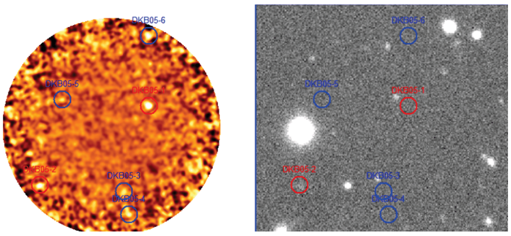
DKB05-6
DKB05-5
DKB05-1
DKB05-2
DKB05-3
DKB05-4
DKB05-6
DKB05-5
DKB05-1
DKB05-2
DKB05-3
DKB05-4

DKB05

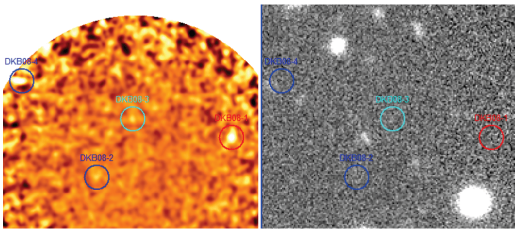
DKB08-4
DKB08-3
DKB08-1
DKB08-2
DKB08-4
DKB08-3
DKB08-1
DKB08-2

DKB08

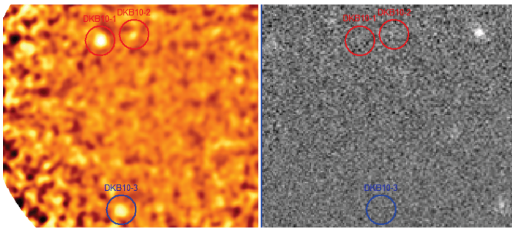
DKB10-1
DKB10-2
DKB10-3
DKB10-1
DKB10-2
DKB10-3

DKB10

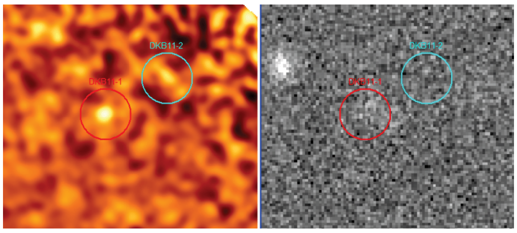
DKB11-2
DKB11-1
DKB11-2
DKB11-1

DKB11

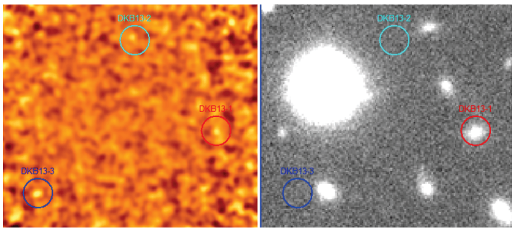
DKB13-2
DKB13-1
DKB13-3
DKB13-2
DKB13-1
DKB13-3

DKB13

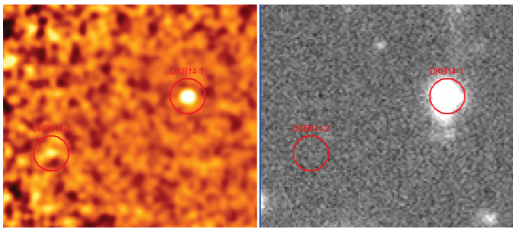
DKB14-1
DKB014-2
DKB14-1
DKB014-2

DKB14

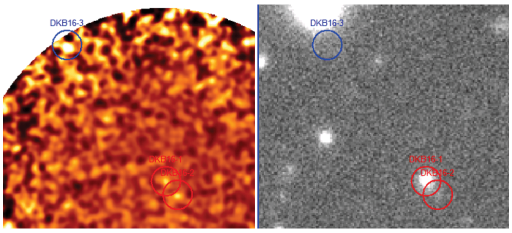
DKB16-3
DKB16-1
DKB16-2

DKB16

B.5 VLT/HAWK-I/H (1.6μm)

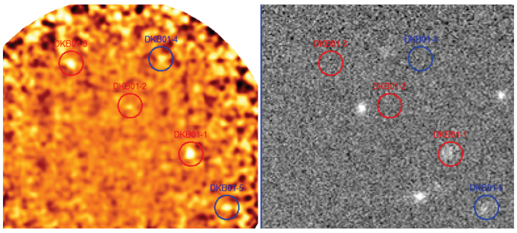
DKB01-4
DKB01-2
DKB01-1
DKB01-5

DKB01

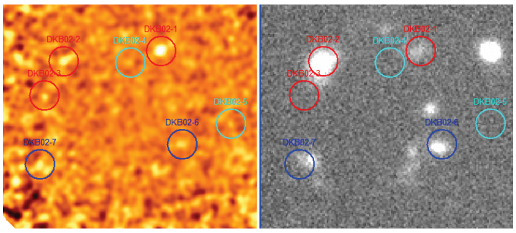
DKB02-2
DKB02-1
DKB02-3
DKB02-5
DKB02-6
DKB02-7

DKB02

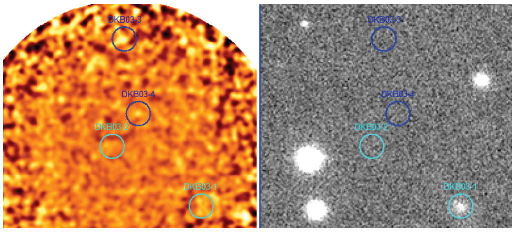
DKB03-3
DKB03-4
DKB03-2
DKB03-1

DKB03

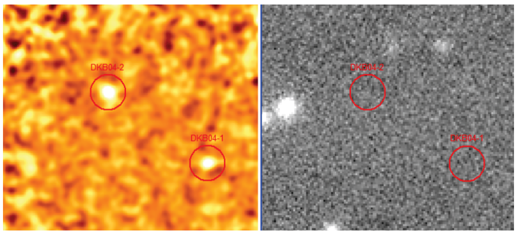
DKB04-2
DKB04-1

DKB04

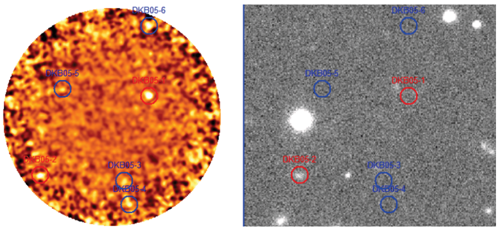
DKB05-6
DKB05-5
DKB05-1
DKB05-2
DKB05-3
DKB05-4

DKB05

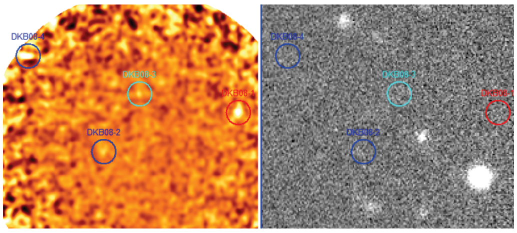
DKB08-4
DKB08-1
DKB08-2

DKB08

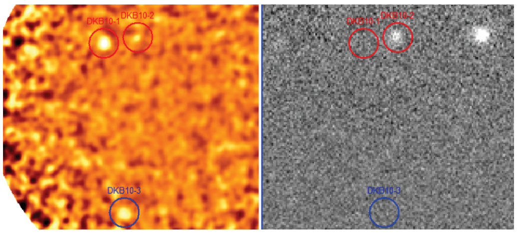
DKB10-1
DKB10-2
DKB10-3

DKB10

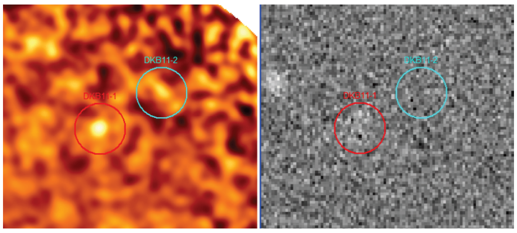
DKB11-2
DKB11-1

DKB11

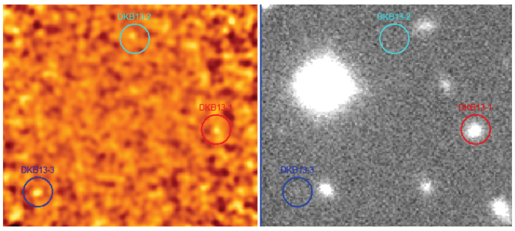
DKB13-2
DKB13-1
DKB13-3
DKB13-2
DKB13-1
DKB13-3

DKB13

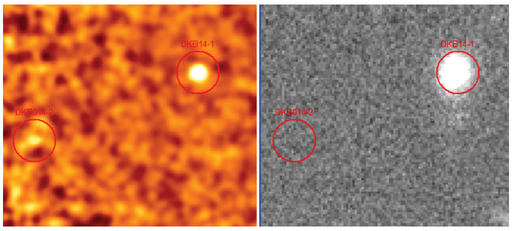
DKB14-1
DKB14-2
DKB14-1
DKB14-2

DKB14

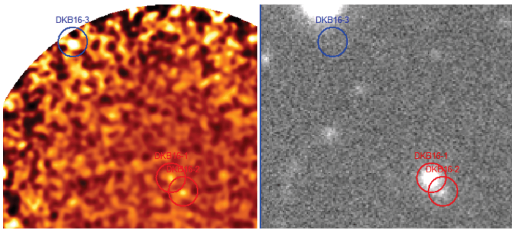
DKB16-3
DKB16-1
DKB16-2
DKB16-3
DKB16-1
DKB16-2

DKB16

B.6 VLT/ISAAC/K_s (2.1μm)

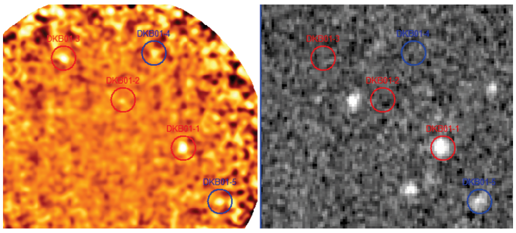
DKB01-3
DKB01-4
DKB01-2
DKB01-1
DKB01-5
DKB01-3
DKB01-4
DKB01-2
DKB01-1
DKB01-5

DKB01

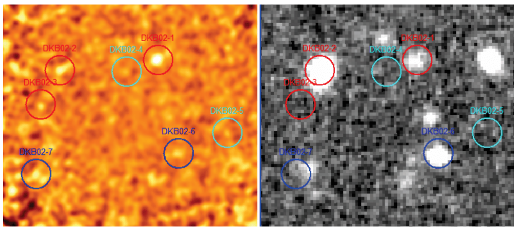
DKB02-2
DKB02-4
DKB02-1
DKB02-3
DKB02-5
DKB02-6
DKB02-7
DKB02-2
DKB02-4
DKB02-1
DKB02-3
DKB02-5
DKB02-6
DKB02-7

DKB02

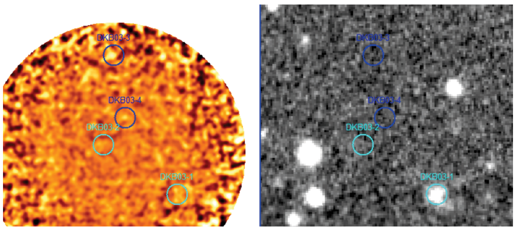
DKB03-3
DKB03-4
DKB03-2
DKB03-1
DKB03-3
DKB03-4
DKB03-2
DKB03-1

DKB03

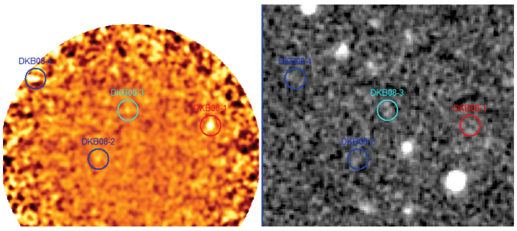
DKB08-4
DKB08-3
DKB08-1
DKB08-2
DKB08-4
DKB08-3
DKB08-1
DKB08-2

DKB08

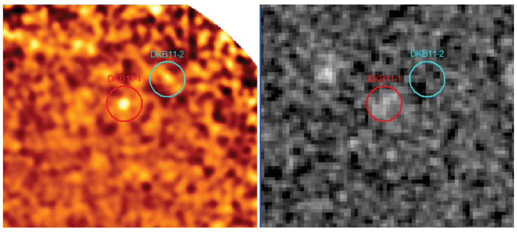
DKB11-2
DKB11-1
DKB11-1
DKB11-2

DKB11

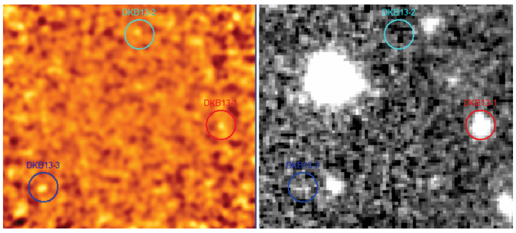
DKB13-2
DKB13-1
DKB13-3
DKB13-2
DKB13-1
DKB13-3

DKB13

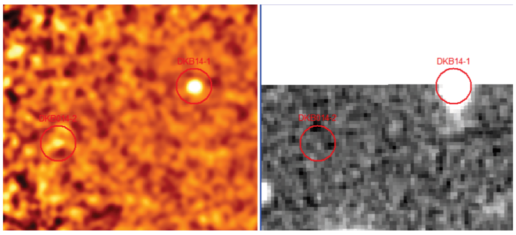
DKB14-1
DKB014-2
DKB14-1
DKB014-2

DKB14

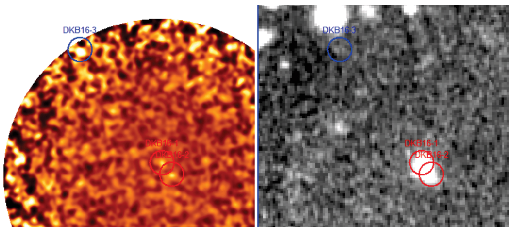
DKB16-3
DKB16-1
DKB16-2
DKB16-3
DKB16-1
DKB16-2

DKB16

B.7 Subaru/MOIRCS/NB2071 (2.1μm, narrow band)

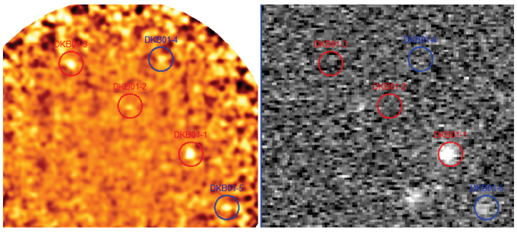
DKB01-3
DKB01-4
DKB01-2
DKB01-1
DKB01-5
DKB01-3
DKB01-4
DKB01-2
DKB01-1
DKB01-5

DKB01

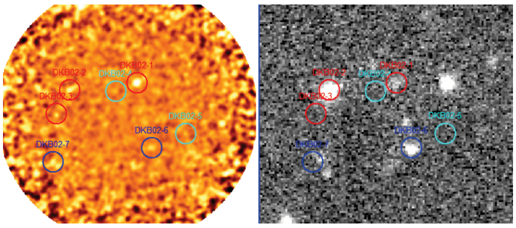
DKB02-1
DKB02-2
DKB02-4
DKB02-3
DKB02-5
DKB02-6
DKB02-7
DKB02-1
DKB02-2
DKB02-4
DKB02-3
DKB02-5
DKB02-6
DKB02-7

DKB02

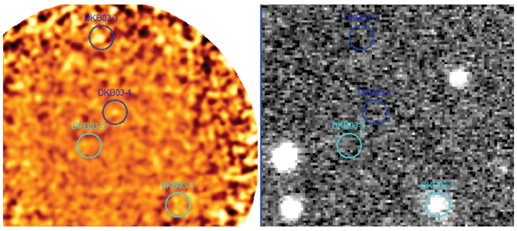
DKB03-3
DKB03-4
DKB03-2
DKB03-1
DKB03-3
DKB03-4
DKB03-2
DKB03-1

DKB03

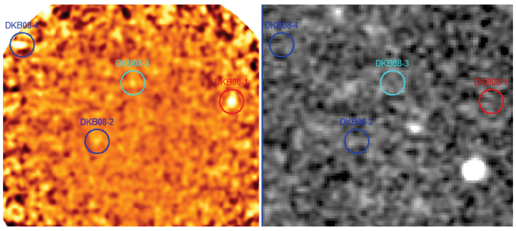
DKB08-4
DKB08-3
DKB08-1
DKB08-2
DKB08-4
DKB08-3
DKB08-1
DKB08-2

DKB08

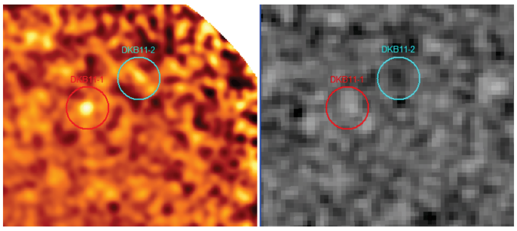
DKB11-2
DKB11-1
DKB11-2
DKB11-1

DKB11

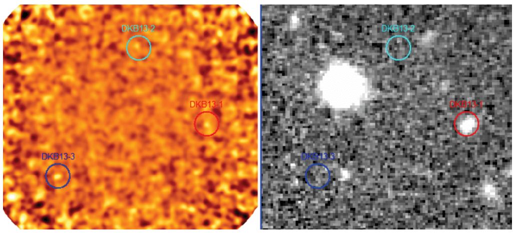
DKB13-2
DKB13-1
DKB13-3
DKB13-2
DKB13-1
DKB13-3

DKB13

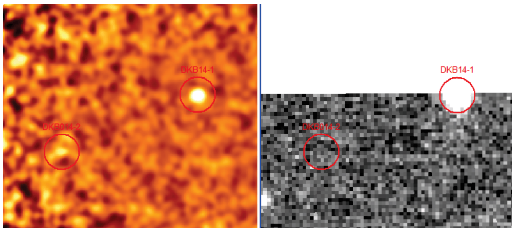
DKB14-1
DKB014-2
DKB14-1
DKB014-2

DKB14

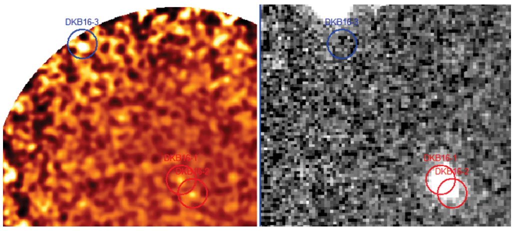
DKB16-3
DKB16-1
DKB16-2
DKB16-3
DKB16-1
DKB16-2

DKB16

B.8 Subaru/MOIRCS/K_s (2.1μm)

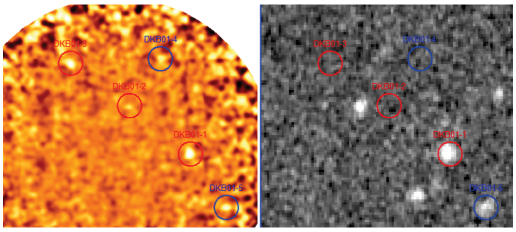
DKB01-3
DKB01-4
DKB01-2
DKB01-1
DKB01-5
DKB01-3
DKB01-4
DKB01-2
DKB01-1
DKB01-5

DKB01

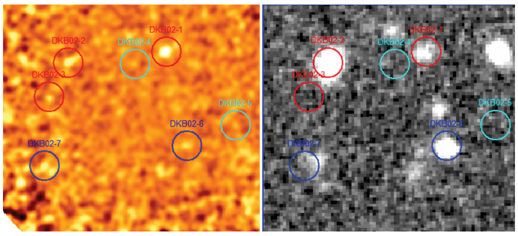
DKB02-1
DKB02-2
DKB02-4
DKB02-3
DKB02-5
DKB02-6
DKB02-7
DKB02-1
DKB02-2
DKB02-4
DKB02-3
DKB02-5
DKB02-6
DKB02-7

DKB02

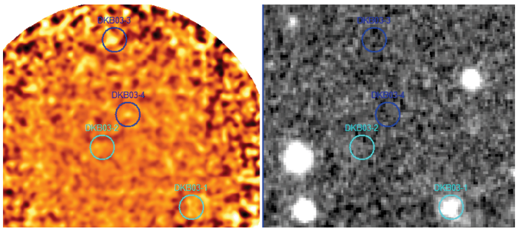
DKB03-3
DKB03-4
DKB03-2
DKB03-1
DKB03-3
DKB03-4
DKB03-2
DKB03-1

DKB03

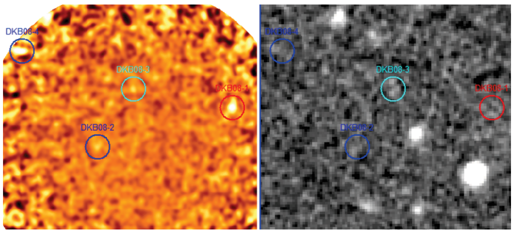
DKB08-4
DKB08-3
DKB08-1
DKB08-2
DKB08-4
DKB08-3
DKB08-1
DKB08-2

DKB08

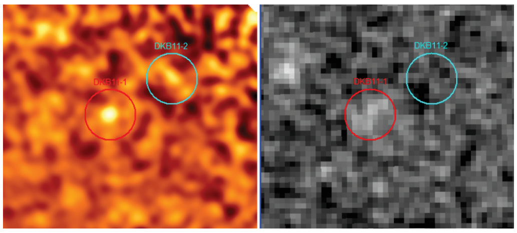
DKB11-2
DKB11-1
DKB11-2
DKB11-1

DKB11

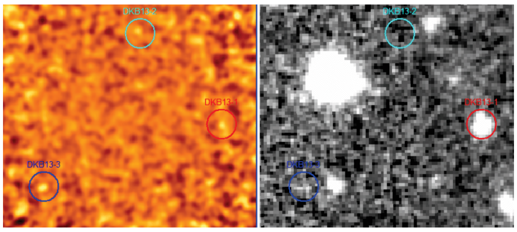
DKB13-2
DKB13-1
DKB13-3
DKB13-2
DKB13-1
DKB13-3

DKB13

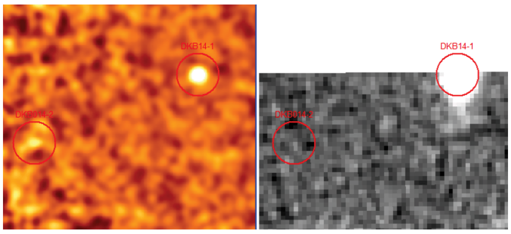
DKB14-1
DKB014-2
DKB14-1
DKB014-2

DKB14

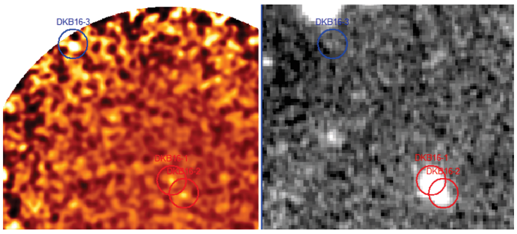
DKB16-3
DKB16-1
DKB16-2
DKB16-3
DKB16-1
DKB16-2

DKB16

B.9 Spitzer/IRAC/ch1 (3.6μm)

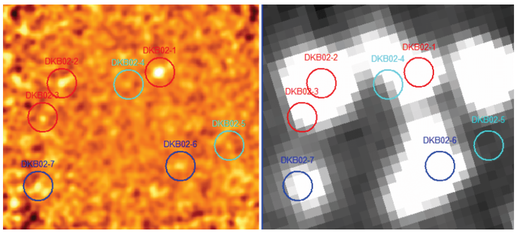
DKB02-1
DKB02-2
DKB02-4
DKB02-3
DKB02-5
DKB02-6
DKB02-7
DKB02-1
DKB02-2
DKB02-4
DKB02-3
DKB02-5
DKB02-6
DKB02-7

DKB01

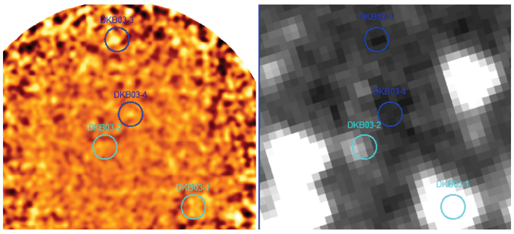
DKB03-3
DKB03-4
DKB03-2
DKB03-1
DKB03-3
DKB03-4
DKB03-2
DKB03-1

DKB02

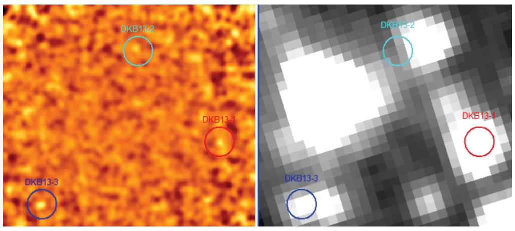
DKB13-2
DKB13-1
DKB13-3
DKB13-2
DKB13-1
DKB13-3

DKB03

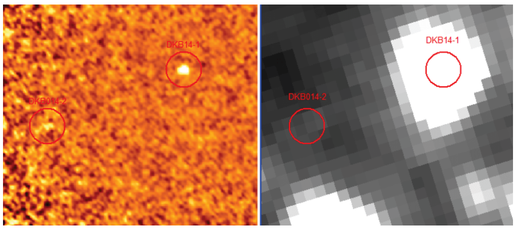
DKB14-1
DKB014-2
DKB14-1
DKB014-2

DKB04

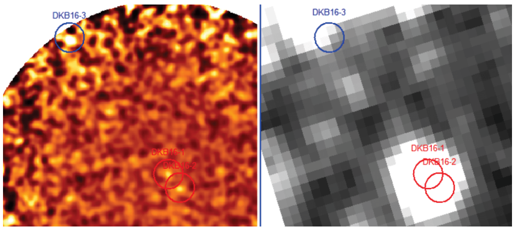
DKB16-3
DKB16-1
DKB16-2
DKB16-3
DKB16-1
DKB16-2

DKB16

B.10 Spitzer/MIPS (24μm)

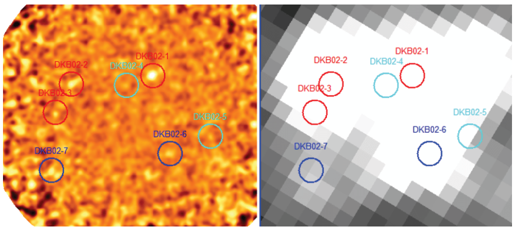
DKB02-2
DKB02-4
DKB02-1
DKB02-3
DKB02-5
DKB02-6
DKB02-7
DKB02-2
DKB02-1
DKB02-4
DKB02-3
DKB02-5
DKB02-6
DKB02-7

DKB01

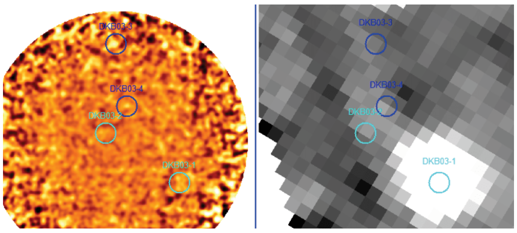
DKB03-3
DKB03-4
DKB03-1
DKB03-3
DKB03-4
DKB03-1

DKB02

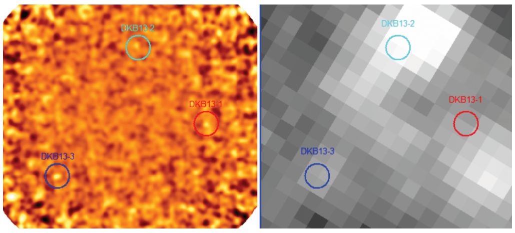
DKB13-2
DKB13-1
DKB13-3
DKB13-2
DKB13-1
DKB13-3

DKB03

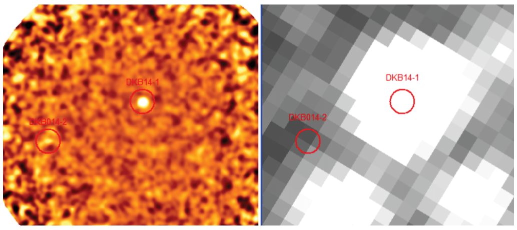
DKB14-1
DKB014-2
DKB14-1
DKB014-2

DKB04

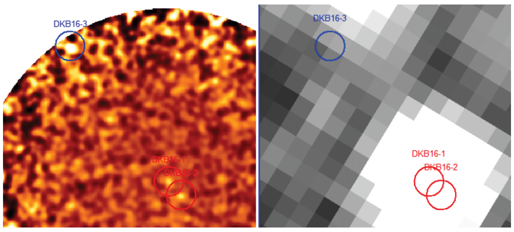
DKB16-3
DKB16-3
DKB16-1
DKB16-2

DKB16

B.11 VLA 1.4GHz

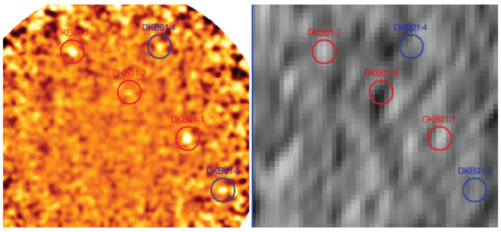
DKB01-3
DKB01-4
DKB01-2
DKB01-1
DKB01-5
DKB01-3
DKB01-4
DKB01-2
DKB01-1
DKB01-5

DKB01

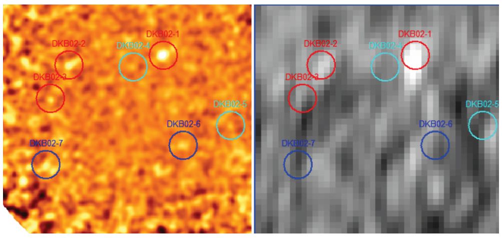
DKB02-2
DKB02-4
DKB02-1
DKB02-3
DKB02-5
DKB02-6
DKB02-7
DKB02-2
DKB02-4
DKB02-1
DKB02-3
DKB02-5
DKB02-6
DKB02-7

DKB02

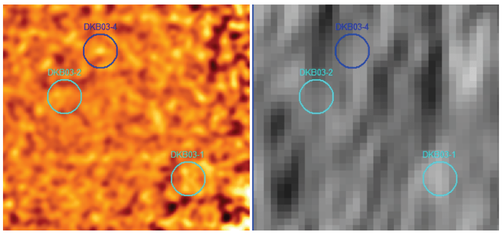
DKB03-4
DKB03-2
DKB03-1
DKB03-4
DKB03-2
DKB03-1

DKB03

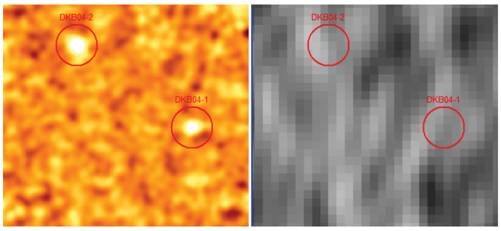
DKB04-2
DKB04-1
DKB04-2
DKB04-1

DKB04

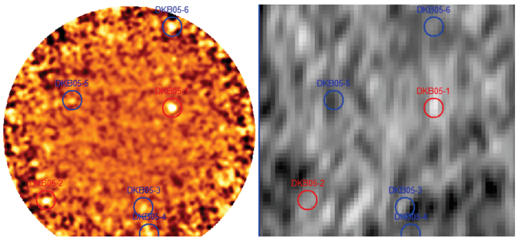
DKB05-6
DKB05-5
DKB05-1
DKB05-2
DKB05-3
DKB05-4
DKB05-6
DKB05-5
DKB05-1
DKB05-2
DKB05-3
DKB05-4

DKB05

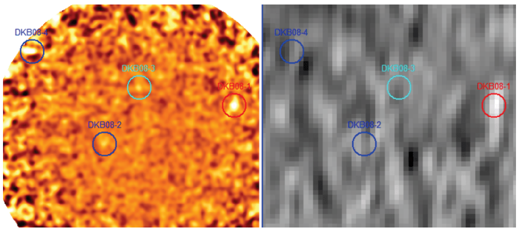
DKB08-4
DKB08-3
DKB08-1
DKB08-2
DKB08-4
DKB08-3
DKB08-1
DKB08-2

DKB08

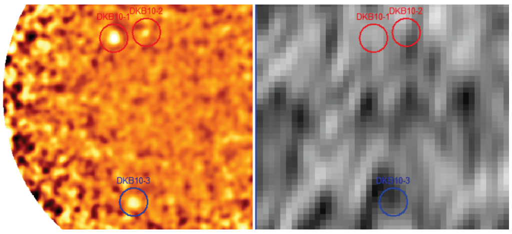
DKB10-1
DKB10-2
DKB10-3
DKB10-1
DKB10-2
DKB10-3

DKB10

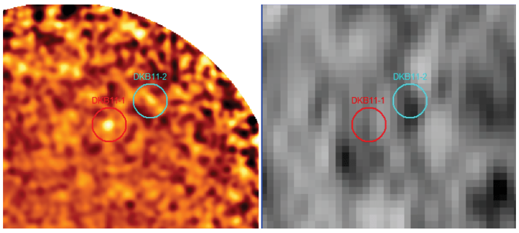
DKB11-2
DKB11-1
DKB11-2
DKB11-1

DKB11

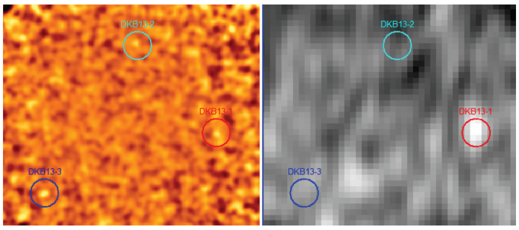

DKB13

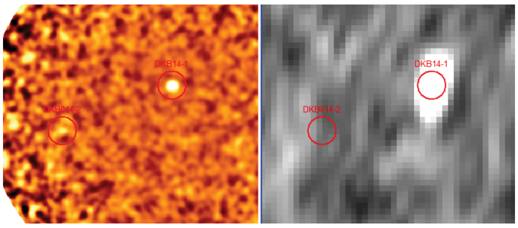

DKB14

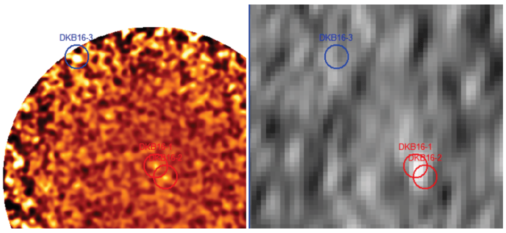

DKB16

ID	H814	H110	H160	NB2071	Sub/K_s	H/Y	H/H	H/K_s	I/K_s	IRAC	MIPS	VLA
DKB01-1	YES	0	0	YES	YES	YES	YES	YES	YES	0	0	106,P
106,P	NO	NO	NO	YES								
DKB01-2	NO	0	0	NO	NO	NO	NO	NO	NO	0	0	NO
DKB01-3	NO	0	0	NO	NO	NO	NO	NO	NO	0	0	YES
DKB01-4	YES	0	0	NO	NO	NO	NO	NO	NO	0	0	NO
DKB01-5	YES	0	0	YES	YES	NO	YES	YES	YES	0	0	NO
DKB02-1	YES	NO	YES	YES	YES	YES	YES	YES	YES	YES	YES	YES
DKB02-2	YES	0	0	YES	YES	YES	YES	YES	YES	YES	YES	YES
DKB02-3	NO	0	0	NO	NO	NO	NO	NO	NO	YES	YES	NO
DKB02-4	NO	NO	NO	NO	NO	NO	NO	NO	NO	NO	YES	NO
DKB02-5	NO	YES	YES	NO	NO	NO	NO	NO	NO	NO	YES	NO
DKB02-6	YES	YES	NO	YES	YES	YES	YES	YES	YES	YES	YES	NO
DKB02-7	YES	NO	NO	YES	YES	YES	YES	YES	YES	YES	YES	NO
DKB03-1	YES	0	0	YES	YES	YES	YES	YES	YES	YES	YES	YES
DKB03-2	YES	0	0	NO	NO	NO	NO	NO	NO	YES	NO	NO
DKB03-3	NO	0	0	NO	NO	NO	NO	NO	NO	NO	NO	NO
DKB03-4	NO	0	0	NO	NO	NO	NO	NO	NO	NO	NO	NO
DKB04-1	0	0	0	NO	NO	NO	NO	NO	0	0	0	NO
DKB04-2	0	0	0	NO	NO	NO	NO	NO	0	0	0	YES
DKB05-1	0	0	0	0	0	NO	NO	YES	0	0	0	YES
DKB05-2	0	0	0	0	0	YES	YES	YES	0	0	0	NO
DKB05-3	0	0	0	0	0	NO	NO	NO	0	0	0	YES
DKB05-4	0	0	0	0	0	NO	NO	NO	0	0	0	NO
DKB05-5	0	0	0	0	0	NO	NO	NO	0	0	0	NO
DKB05-6	0	0	0	0	0	NO	NO	NO	0	0	0	NO
DKB08-1	0	0	0	NO	NO	NO	NO	NO	NO	0	0	YES
DKB08-2	0	0	0	NO	NO	NO	NO	NO	NO	0	0	NO
DKB08-3	0	0	0	NO	YES	NO	NO	NO	NO	0	0	NO
DKB08-4	0	0	0	NO	YES	NO	NO	NO	NO	0	0	NO
DKB10-1	0	0	0	0	0	NO	NO	NO	0	0	0	NO
DKB10-2	0	0	0	0	0	YES	YES	YES	0	0	0	NO
DKB10-3	0	0	0	0	0	NO	NO	NO	0	0	0	NO
DKB11-1	0	0	0	YES	YES	YES	YES	YES	YES	0	0	NO
DKB11-2	0	0	0	NO	NO	NO	NO	NO	NO	0	0	NO
DKB13-1	YES	0	0	YES	YES	YES	YES	YES	YES	YES	NO	YES
DKB13-2	NO	0	0	NO	NO	NO	NO	NO	NO	YES	YES	NO
DKB13-3	YES	0	0	NO	YES	NO	NO	YES	YES	YES	YES	NO
DKB14-1	0	0	0	YES	YES	YES	YES	YES	YES	YES	YES	YES
DKB14-2	0	0	0	YES	NO	NO	NO	NO	NO	NO	NO	YES
DKB16-1	0	0	0	YES	YES	YES	YES	YES	YES	YES	YES	YES
DKB16-2	0	0	0	YES	YES	NO	YES	YES	YES	YES	YES	YES
DKB16-3	0	0	0	NO	NO	NO	NO	NO	NO	YES	YES	YES

Table B.1: Candidate counterparts table for the main datasets. Per each ALMA detection (column 1), we specify whether each other available band has a candidate counterpart ("YES"), or it does not ("NO"), or it is not covered by the dataset ("0"). In the Herschel columns, if there is a counterpart in the catalogue used, we indicate its name. Column (2): HST/ACS/814nm. Column (3): HST/NICMOS/1.1μm. Column (4): HST/NICMOS/1.6μm. Column (5): Subaru/MOIRCS/K_s. Column (6): Subaru/MOIRCS/NB2071. Column (7): VLT/HAWK-I/Y. Column (8): VLT/HAWK-I/H. Column (9): VLT/HAWK-I/K_s. Column (10): VLT/ISAAC/K_s. Column (11): Spitzer/IRAC. Column (12): Spitzer/MIPS. Column (13): VLA 1.4 GHz.

Acknowledgements

Heartfelt thanks to Helmut Dannerbauer for his technical and scientific assistance, also for welcoming me at IAC and for teaching me a lot about research. Heartfelt thanks also to Paolo Cassata for his precious insights, for his support and for giving me the opportunity of doing this traineeship. I also thank Rosa Calvi, Emanuel Ríos-López, Victor Bonjean, Chiara D'Eugenio, Nataliya Ramos Chernenko, Zhengyi Chen, Zohreh Ghaffari, Andrés Laza Ramos, Andrea Negri, Alessio Anitra and Francesco Sinigaglia for scientific consulting and for being great friends during my staying.

Ringrazio mia mamma Carla per avermi aiutato nei momenti difficili di questi ultimi mesi.

Infine, ringrazio Martina, a cui dedico questa tesi, che mi ha sempre ascoltato con pazienza, dato motivazione quando non ne avevo più e senza cui non sarei arrivato alla fine di questo percorso.